9-27-2018

Studies on Nitric Oxide Generation and its Enzymatic Degradation

Kathleen Fontana

University of Windsor

Recommended Citation

Fontana, Kathleen, "Studies on Nitric Oxide Generation and its Enzymatic Degradation" (2018). *Electronic Theses and Dissertations*. 7520.
https://scholar.uwindsor.ca/etd/7520

Studies on Nitric Oxide Generation and its Enzymatic Degradation

By

Kathleen Fontana

A Thesis
Submitted to the Faculty of Graduate Studies
through the Department of Chemistry & Biochemistry
in Partial Fulfillment of the Requirements for
the Degree of Master of Science
at the University of Windsor

Windsor, Ontario, Canada

2018

Studies on Nitric Oxide Generation and its Enzymatic Degradation

By

Kathleen Fontana

APPROVED BY:

P. Karpowicz
Department of Biological Sciences

P. O. Vacratsis
Department of Chemistry & Biochemistry

B. Mutus, Advisor
Department of Chemistry & Biochemistry

September 20th, 2018

DECLARATION OF ORIGINALITY

I hereby certify that I am the sole author of this thesis and that no part of this thesis has been published or submitted for publication.

I certify that, to the best of my knowledge, my thesis does not infringe upon anyone’s copyright nor violate any proprietary rights and that any ideas, techniques, quotations, or any other material from the work of other people included in my thesis, published or otherwise, are fully acknowledged in accordance with the standard referencing practices. Furthermore, to the extent that I have included copyrighted material that surpasses the bounds of fair dealing within the meaning of the Canada Copyright Act, I certify that I have obtained a written permission from the copyright owner(s) to include such material(s) in my thesis and have included copies of such copyright clearances to my appendix.

I declare that this is a true copy of my thesis, including any final revisions, as approved by my thesis committee and the Graduate Studies office, and that this thesis has not been submitted for a higher degree to any other University or Institution.

ABSTRACT

Nitric oxide (NO) is a vital gasotransmitter, involved in a plethora of signaling pathways. With bioavailable NO stored as S-nitrosoglutathione (GSNO), its enzymatic degradation by S-nitrosoglutathione reductase (GSNOR) has a large impact on cellular SNO levels. This thesis consists of two components: chapter one explores the production of NO generating particles, that use chitosan as a matrix for a copper catalyst. Chapter two reports the discovery into a new regulatory domain on the GSNOR enzyme.

In chapter one, we have developed a novel technology capable of generating NO, in the form of NO-releasing copper-chitosan particles (Cu-chito). These particles were successfully tested in their release of authentic NO: the maximum rate of production was 1.40 nmol/min/g. The Cu-chito particle treatments were analysed using scratch assays. In comparison to control groups: Cu-chito particles, which provide bioactive NO, displayed 130% of cells in the wound, while treatments with supplemented glucose displayed 152%. This supports the hypothesis that glucose aids to regenerate active copper in the catalytic cycle of NO production. Matrix metalloproteinases (MMP-2 and -9) were chosen as an intracellular NO target. The activity MMP was investigated: displayed an increase of 60% after Cu-chito treatments. The NO treatments provide a lasting effect on a cellular level.

Presented in chapter two is the discovery of a new regulatory domain on GSNOR: an allosteric binding domain. A sigmoidal deviation in GSNOR kinetics indicated positive cooperativity for GSNO binding. Molecular docking (MD) simulations indicates the location a putative allosteric site at the amino acid residues Gly321, Lys323, Asn185, and Lys188. To further these studies hydrogen / deuterium exchange (HDX) mass spectrometry (MS) experiments were performed. With a two second HDX reaction, the residues Gly321, Lys323, and Lys188 displayed a decrease in deuterium uptake of 1.4%, 1.4%, and 0.4%, after the incorporation of GSNO. These results strongly support the existence of a secondary binding domain of substrate GSNO that contributes to its mechanism of action.

DEDICATION

To my parents and Nathan.

ACKNOWLEDGEMENTS

First and foremost, I would like to offer my heartfelt gratitude to my supervisor, Dr. Bulent Mutus, for the guidance and support he has provided me throughout my graduate, and undergraduate, studies. He has provided me with the opportunity to thrive as a researcher and has provided an environment for me to grow as an individual. My appreciation is further extended to members of my supervisory committee, Dr. Panayiotis O. Vacratsis and Dr. Phillip Karpowicz for their advice, suggestions, and the critical evaluation of my thesis.

This research would not have been made possible without our collaborators, Dr. Derek Wilson and his lab manager, Cristina Lento. I thank them for their knowledge, guidance, and resources. Further collaborative thanks extend to Dr. James Gauld and his student Sahar Nikoo for their computational inputs, under the direction of Drs Bei Sun and Mutus.

To the faculty and staff of the department of Chemistry & Biochemistry, who has allowed the progress of my education with their diligence and hard work. Including administrative staff Catherine Wilson, Elizabeth Kickham, and Marlene Bezaire. As well as lab coordinators Nedhal, Norah, Ronan, and Una.

A special thanks to fellow lab member Dr. Bei Sun, whose past work with GSNOR made my project possible. I would like to thank Dr. Sun, as well as Dr. Artur Jarosz, Hyder Ali Khan, and Terence Yep, for their direct training and support that allowed me to grow as researcher. It was a pleasure to have worked alongside other lab members: Cody Caba, Scott Smith, Leslie Ventimiglia, as well as Mitchell, Bianca, Angela, Dave, Nneamaka, Milosz, Farzana, Alexa, Adnan, and Brett. The friendships and connections formed throughout the department of Chemistry & Biochemistry have been unforgettable throughout my education. Thank you, Ashley, Justin, Mike, Elodie, The Isotopes, ChemClub, past GA’s, other graduate students, and the class of 2016 undergraduate thesis students for providing this community.

Finally, I am forever grateful to my parents, my siblings, and Nathan Bazinski, for their unwavering love, support, encouragement, and understanding.

TABLE OF CONTENTS

TABLE OF FIGURES

TABLE OF TABLES

TABLE OF EQUATIONS

TABLE OF APPENDICES

LIST OF NOMENCLATURE & ABBREVIATIONS

NO	Nitric oxide
NO_2^-	Nitrite
Cu	Copper
Cu-Chito	Copper-chitosan milli-particles
Chito	Chitosan milli-particles
CO	Carbon monoxide
H_2S	Hydrogen sulfide
RNS	Reactive nitrogen species
NOS	Nitic oxide synthases
GSH	Glutathione
GSNO	S-nitrosoglutathione
GSSH	Oxidized glutathione
EDRF	Endothelium-derived relaxing factor
cNOS	Constitutive isoforms (cNOS) of nitric oxide synthase
eNOS	Vascular endothelial isoform of nitric oxide synthase
nNOS	Neuronal isoform of nitric oxide synthase
sGC	Soluble guanylate cyclase
cGMP	Cyclic guanosine monophosphate
iNOS	Inducible isoforms of nitric oxide synthase
IBS	Inflammatory bowel disease
MMP	Matrix metalloproteinase
VEGF	Vascular endothelial growth factor
SNO	S-nitrosothiol
PDMS	Polydimethylsiloxane
Dansyl chloride	5-(dimethylamino)naphthalene-1-sulfonyl chloride; DNSC
$CuCl_2$	Copper chloride

NOA 280i	Sievers NO analyzer, model 280i
DTT	Dithiothreitol
PBS	Phosphate buffered saline
ARPE-19	Human retinal pigmented epithelium cells
FBS	Fetal bovine serum
TIMPs	Tissue inhibitors of metalloproteinases
ELISA	Enzyme-linked immunosorbent assay
RT-PCR	Reverse transcription polymerase chain reaction
FGF-2	Fibroblast growth factor 2
ADH5	GSNOR, GSH-FDH, FALDH, AHDX, FDH, and HEL-S-60p
GSNOR	S-nitrosoglutathione reductase; ADH5
GSNO	S-nitrosoglutathione
TRESI	Time-resolved electrospray
HDX	Hydrogen/deuterium exchange
MS	Mass spectrometry
GSH-FDH	Glutathione-dependent formaldehyde dehydrogenase; ADH5
HMGSH	S-(hydroxymethyl)glutathione
NADH	Nicotinamide adenine dinucleotide + hydrogen
GSNHOH	N-hydroxy-sulphenamide
GSSG	Dimerized glutathione
NH_2OH	Hydroxylamine
$GSONH_2$	Glutathione sulphinamide
GSOOH	Glutathione sulphinic acid
NH_4^+	Ammonia
CFTR	Cystic fibrosis transmembrane conductance regulator
ESI	Electrospray ionization
m/z	Mass charge ratio
Synapt G1 MS	Waters Synapt G1 High Definition Mass Spectrometer
IMS	Ion mobility separation
CID	Collision Induced Dissociation

TOF	Time of flight
PMMA	Poly(methyl methacrylate)
MS-MS	Tandem mass spectrometry; MS2
D_2O	Deuterium oxide
o.d.	Outer diameter
i.d.	Inner diameter
MD	Molecular docking

CHAPTER 1: Nitric Oxide Generating Copper-Chitosan Particles

1.1 Chapter Summary

Nitric oxide (NO) is a signaling molecule that plays many roles during infection, inflammation, and wound healing processes. Due to NO's role in wound repair, we have developed a novel NO generation system based on copper-chitosan complexes that can be used for the topical generation of NO. Chitosan, a biocompatible polymer, chelates copper ions. Copper in the +1 state can reduce nitrite (NO_2^-) and convert it into NO. With glucose, a reducing sugar, present in the system, Cu^{+2} can be returned to Cu^{+1} to complete the catalytic cycle. Copper-chitosan milli- and micro- sized particles were produced using microfluidic techniques. Copper-chitosan milli-particles (Cu-chito) did produce nitric oxide (NO). The maximum rates of NO production were ~ 1.40 nmol/min/g (Cu-chito) and 1.08 nmol/min/g (Cu-chito + glucose). The milli-particles were tested with ARPE-19 cell lines in scratch assays, to mimic an *in vitro* model for wound healing. Cu-chito particle treatments with nitrite showed 130% new cells in the wound in comparison to chitosan milli-particles not containing copper. Furthermore, Cu-chito treatments of nitrite + glucose showed 152% new cells in the wound in comparison to control groups, and 118% in comparison to Cu-chito with nitrite alone. The activity of intracellular NO target, matrix metalloproteinases (MMP-2 and -9), were shown to increase by 60% after 48 hours of Cu-chito ± glucose treatments.

1.2 Introduction

This chapter focuses on the development of a nitric oxide (NO) releasing technology for the desired application relating to wound healing and other similar medical or biological fields. In order to do this, the physiological relevance and implications of NO and other components of the technology must first be described.

1.2.1 Gasotransmitters

Gasotransmitters is a term used to describe a group of small gaseous signaling molecules consisting of nitric oxide (NO), carbon monoxide (CO), and hydrogen sulfide (H_2S). As a group, gasotransmitters have several interesting properties. They are endogenously produced molecules that have significant roles as physiologic mediators in the cardiovascular (NO, CO, H_2S), immune (NO, CO), and nervous systems (NO, H_2S), while also existing as toxic gasses.[1-3] They have high lipid solubilities, can freely pass through cellular membranes and have specific targets; including the metal centers of metalloproteins, such as guanylyl cyclase.[1-2] For example, the main targets of NO, and other reactive nitrogen species (RNS), include metal centers and thiols.[3]

The ability to penetrate the cellular membrane is just one property that distinguishes gasotransmitters from other, more classical signaling molecules, which could require other mechanisms, such as binding to plasma membrane receptors in order to reach their targets.[1-2] Since gaseous molecules are not easily stored (i.e. in vesicles), they are produced as required and diffused out. In turn, the robust reactivity of NO and H_2S relates to the requirement of being subjected to regulatory systems. For example, both molecules will readily react with the cysteine thiol of glutathione, which could yield problematic results if that is not the intended destination.[2] The robust action of NO and H_2S is countered by the body's ability to biochemically detox them; they are readily metabolized by cytochrome oxidases (a group of metalloproteins).[3-4] In the instance of NO, regulation is performed by the control of nitic oxide synthases (NOS), the group of enzymes responsible for its biosynthesis. NO can reach its target by the binding of NOS to the protein target, or with the aid of scaffolding proteins.[2]

As it stands, the reaction of NO and H_2S with glutathione does a sufficient job of visualizing the effects that are typical of gasotransmitters; by chemically modifying intracellular proteins. In contrast to classical messenger molecules mode of action being amplifying signaling cascades. The chemical reactions of glutathione (GSH) reacting with NO and H_2S are shown in **Figure 1.2.1a**.

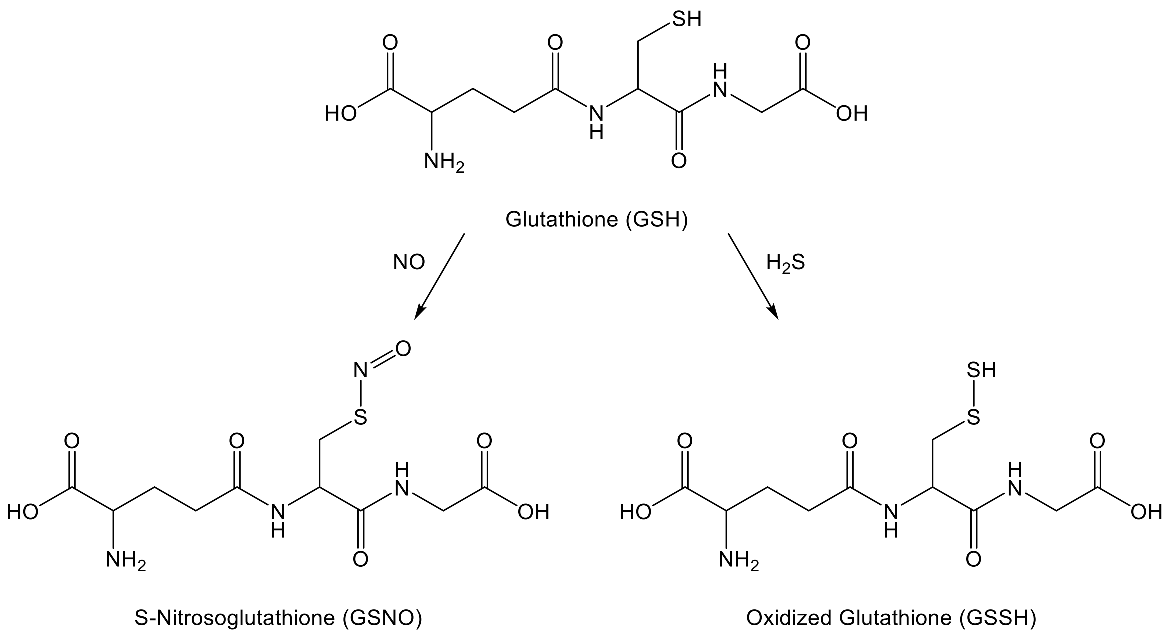

Figure 1.2.1a: Glutathione (GSH) reacting with the gasotransmitters NO and H_2S. Producing S-nitrosoglutathione (GSNO) and oxidized glutathione (GSSH), respectively.

1.2.2 Nitric Oxide, the First Gasotransmitter

Nitric oxide (NO), the gaseous radical shown in **Figure 1.2.2a**, was the first identified gasotransmitter. The molecule itself was discovered in 1772 by Joseph Priestley. In the late 1980's there were breakthroughs in regards to its biological role. The research group led by Dr. Louis J. Ignarro discovered that NO was the endothelium-derived relaxing factor (EDRF). This led to him being awarded the Nobel Prize in Medicine in 1998, in conjunction with Robert F. Furchgott and Ferid Murad for their work with NO. Research interests took off after NO was named "Molecule of the Year" in 1992.

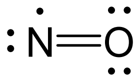

Figure 1.2.2a: Nitric oxide Lewis dot diagram

NO is produced in the body principally through nitric oxide synthases (NOSs).[5-6] In general, NOSs are responsible for the NO produced in eukaryotic cells; they are found in animals, partly conserved in bacteria and in some algae.[7] Other organisms, including land plants, use alternative methods like nitrite reduction.[7]

Basal levels of NO are produced by the constitutive isoforms (cNOS) of nitric oxide synthase, which continuously produces NO in the picomolar to nanomolar levels necessary for signaling. There are two isoforms of cNOS, one originally discovered in vascular endothelial cells (eNOS) and a neuronal isoform found in the brain (nNOS), they have since been discovered in other tissues.[8-9] Its role as the EDRF, responsible for the dilation of blood vessels, is one of its basal functions in vascular endothelial cells. NO activates soluble guanylate cyclase (sGC), an enzyme involved in vasodilation.[10] In the central nervous system, NO mediates the increase of cyclic guanosine monophosphate (cGMP) via the activation of glutamate receptors.[11-13] The activation of cGMP controls vascular tone, participates in the control of blood pressure, and regulates the distribution of flow between vascular beds, including the brain and skeletal muscles.[10]

Beyond cNOS, NO can also be produced in larger quantities (micromolar) by the inducible isoforms of nitric oxide synthase (iNOS), in response to stimuli such as endotoxins and cytokines, which are often released in response to infections, inflammation, and other pathologies.[10, 14-15] iNOS is calcium-independent and was discovered in macrophages, with roles in the immune system; with responses to burn injuries, arthritis, and inflammatory bowel diseases (IBSs).[15] At the micromolar levels produced by iNOS, NO can display toxic effects that work to aid the immune system by killing microorganisms, viruses, and parasites.[10]

1.2.3 Downstream NO Signaling & Matrix Metalloproteinase's (MMP).

NO plays several roles in wound healing. It has a central role in physiological and pathological processes of angiogenesis where it can promote collagen deposition at the wound site, which helps to increase the strength of the healed wound.[16-18] Inhibition of NO at a wound site results in a decrease of collagen produced and decreased formation of granulation tissue.[19] In the vasculature, NO can stimulate cell proliferation, provide protection from apoptosis, prevent against thrombosis, and is the mediator for the vascular endothelial growth factor (VEGF).[17] In addition, NO has been shown to display some antiplatelet, antiatherosclerotic, haemodynamic and neuroprotective properties.[10] Topically applied NO has been shown to increase dermal microcirculation in skin models.[20]

Downstream signaling effects of NO are observed throughout cell physiology. For example, NO activates guanylyl cyclase which can then produce cyclic guanosine monophosphate (cGMP). One of cGMP's signaling roles include the dilation of blood vessels. Other effects of NO include the influence of other proteins, such as matrix metalloproteinase's (MMP). MMP's play a central proteolytic role in extracellular matrix remodeling, during processes such as cell proliferation, angiogenesis and more.[21] A NO regulatory effect on the activity of MMPs has been observed. In a wound model by Ridnour *et al*. media exhibiting peak MMP activity increased corresponded to a vascular cell migration that was MMP-9-dependent, which suggested that MMP-9 is a key physiologic mediator of the effects of NO.[22] Multiple pathways of MMP activation by NO have been discovered: MMP's are influenced by cGMP (a reaction product of NO), VEGF-stimulated cerebral MMP has been found to be mediated through NO produced by iNOS, elevated levels of NO has been found to correspond with MMP activity in diseases like rheumatoid arthritis, where cartilage breakdown is predominant, or cancer, where rapid remodeling and angiogenesis takes place.[22-24]

1.2.4 Medical Effects of NO

Certain disease states and health complications can deteriorate by the body's inefficient production of NO, or its decrease in sensitivity to NO. NO activity can be tracked by the levels of the post translational modification S-nitrosylation (SNO), which is the result of NO signaling. This NO adduct on cysteine thiols (SNOs) can be investigated. Abnormal S-nitrosylation can be found in various human diseases. Such is the case for diabetes, where impaired function of NO synthase is prevalent. Diabetic peripheral neuropathy is a long term complication for diabetic patients and can lead to amputation; this is theorized to be caused by lack of NO.[25-26] It was found that diabetic patients displayed an increase in red blood cell SNO-hemoglobin that displayed a defective release of the NO adduct.[27] Increased SNOs in the joints can be found with arthritis due to local NO production, there is an increase in airway SNOs during pneumonia due to the induction of iNOS, and the S-nitrosylation of MMP-9 can be found during stroke via the activation of nNOS.[27] A decreased amount of SNO-hemoglobin in red blood cells can be found in pulmonary hypertension due to low oxygen saturation and a deacrease in SNO-proteins in the lung can be found with pre-term birth due to decreased NOS expression.[27]

NO is already incorporated into various treatment plans for many cardiopulmonary disorders, including for sickle cell disease, lung and heart transplants, and for newborns with pulmonary hypertension.[28] It has been used for biomedical devices, such as stents. A stent with NO donor-containing liposomes has been shown to enhance endothelial cell proliferation, while inhibiting smooth muscle cell proliferation for the purpose of fighting against thrombosis and restenosis.[29-30] NO can also be used to disperse biofilms from accumulating on surfaces like catheters, implants, and on wounds.[31]

Due to NO's role in wound repair, we have developed a novel NO generation system based on copper-chitosan complexes that can potentially be used for the topical generation of NO. Chitosan (derived from chitin) is a hydrophilic polysaccharide, made from D-glucosamine and N-acetyl-D-glucosamine monomers bound through ß(1→4) linkages.[32] Chitosan is a biocompatible, biodegradable, non-toxic, and antimicrobial polymer.[33] As well, it is already used for various medical purposes such as wound dressings, tissue engineering, plastic surgery, and for drug delivery systems.[33] Here, chitosan was chosen as the base matrix for the NO generation system due to its ability to chelate various metal ions, including copper (**Figure 1.2.4a**). A study by Martinez *et al.* showed that their nitric oxide releasing nanoparticles, a hydrogel/glass composite made using chitosan, had beneficial effects on wound closure using mouse models.[16] The nanoparticles in this study used the glass properties of the composite to reduce nitrite to NO. The NO produced was tested as a therapeutic strategy against superficial skin infections; successful with both MRSA and MRSS bacterial strains.[16]

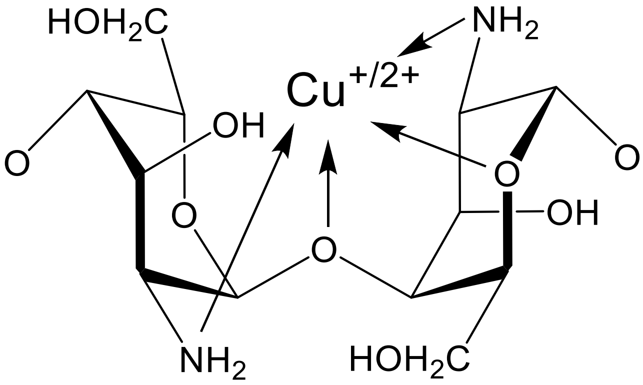

Figure 1.2.4a: Postulated structure for Chitosan-copper complex.

1.2.5 Chitosan & Our Technology

Chitosan has previously been used in wound healing applications, mainly due to its antimicrobial properties and its ability to perform as a stand-alone film, while being supported by a backbone matrix (scaffolds), or as a gel. For instance, some success has been found with a chitosan-based, film-forming gel containing an antibiotic in diabetic mice wounds.[34] Films, both made with chitosan alone and one with chitosan combined with silver oxide nanoparticles were used in rat models. Both of these films outcompeted the control group in a wound healing model, with a significant increase observed with the modified chitosan.[35] These results were especially apparent in the early phases of wound healing. As well, chitosan-based scaffolds have shown an ability to enhance the process of tissue regeneration when combined with immobilized growth factors.[36] Chitosan is a highly versatile biopolymer.

In this study, we present copper chitosan derivatives that produce NO by reducing nitrite. During this process copper is oxidized to the +2 state.[37] Glucose, a reducing sugar, is added to the system to return copper to its +1 state.[38-39] The overall process is schematically shown in **Figure 1.2.5a (i)**, with the postulated mechanism of NO conversion is shown in **Figure 1.2.5a (ii)**. Here, we made copper chitosan milli- and micro- sized particles and demonstrated the NO production using a NO analyzer, a cell culture model of wound healing, and by monitoring the intracellular NO target MMP-2 and -9.

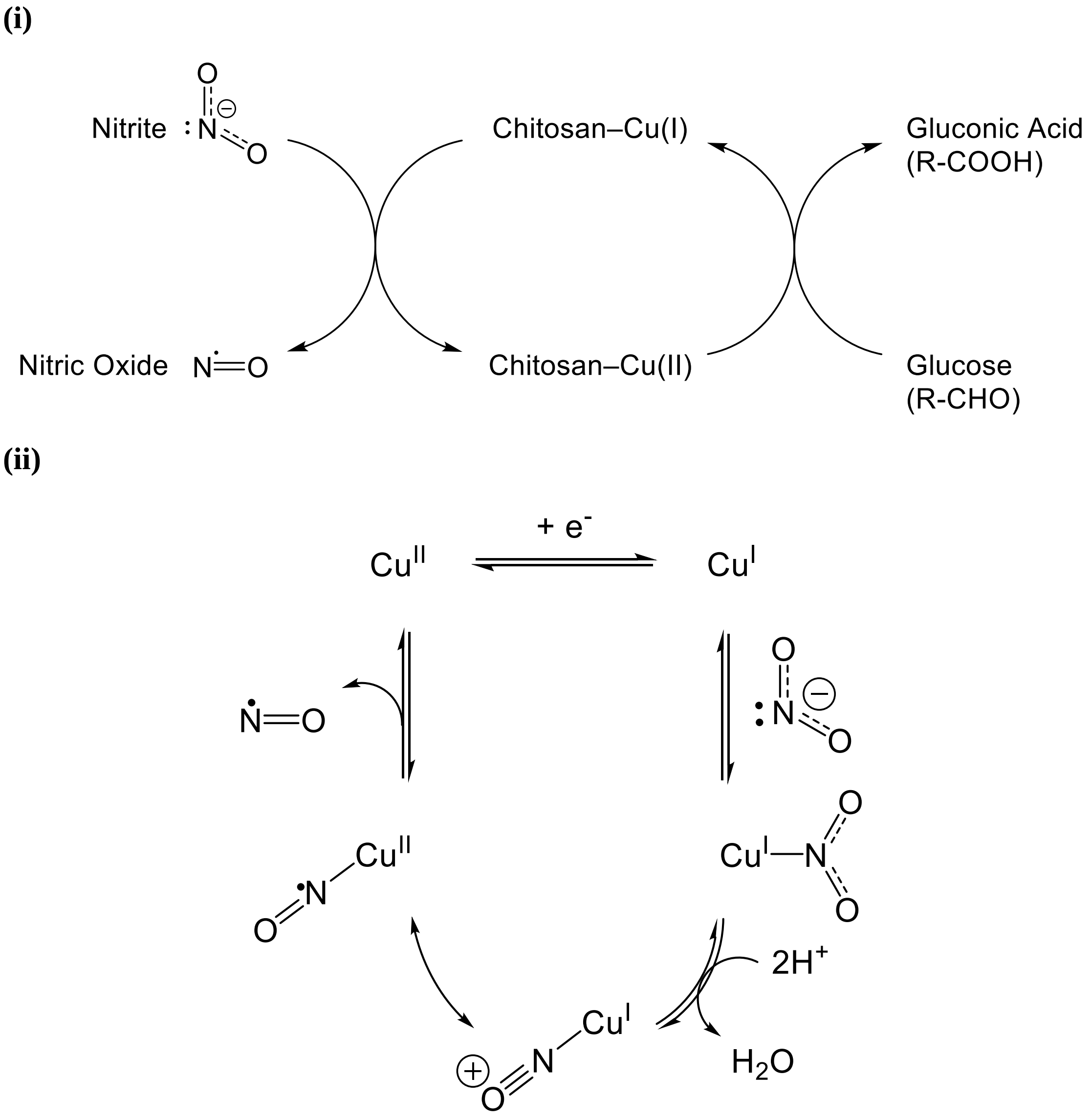

Figure 1.2.5a: Structures of Copper-Chitosan.

(i) Copper-chitosan's pathway to making nitric oxide. Nitric oxide reduced from nitrite via the oxidation copper (I) chitosan particles. The catalytic cycle is completed by cupper being reduced by the oxidation of glucose to gluconic acid.

(ii) Postulated mechanism for NO production from nitrite and Cu^{+1}. Nitrite (NO_2^-) binds to Cu(I), where it becomes protonated. Water is released to produce a copper-nitrosyl (Cu(I)-NO^+). Cu(I)-NO^+ is then reduced by the copper center and nitric oxide is released. Cu(II) is reduced to Cu(I) to complete the catalytic cycle.

1.3 Methods

Chitosan and copper-chitosan particles were successfully produced on the micro- and milli-size scale. Milli-size particles were used for experiments, including experiments utilizing a Nitric Oxide Analyser to test for NO production, scratch assays to test for cellular response in regards to cell growth, as well as a matrix metalloproteinase (MMP) activity assays for a closer look at the NO effect at a cellular level. Chitosan and copper-chitosan particles milli-particles will be respectively referred to as "chito" and "Cu-chito" henceforth.

1.3.1 Copper-Chitosan Micro-Particle Preparation

Soft lithography and molding techniques were used to prepare polydimethylsiloxane (PDMS) microfluidics apparatus, containing micro channels used to control fluid flow. The apparatus is shown in **Figure 1.3.1a (i)**. The design was adapted from Sugaya *et al.*'s apparatus for micrometer-sized chitosan hydrogel beads.[40]

The PDMS mold was designed to have the dimensions of a glass microscope slide, 25.4 x 76.2 mm. To complete assembly, the mold was clamped between two microscope slides using small binder clips. Tubing connected each channel to a syringe, via a 20G needle connection. This full set up is shown in **Figure 1.3.1a (ii)**.

The mold contained four micro channels placed in a cross formation, three for reagents and one to act as an exit channel. Particles are formed by taking advantage of the solubility properties of chitosan. Acid-dissolved chitosan solutions were made by dissolving 0.05% (w/v) chitosan in 0.1 M acetic acid. This dilute chitosan solution was pumped down the vertical micro channel at a speed of 5 µL/min from a 10 mL syringe, using a NE-300 Syringe Pump. This continuous flow was disrupted by 50 mM NaOH being pumped by two other syringe pumps delivering NaOH solutions from 60 mL syringes into their respective horizontal micro channel at a rate of 50 µL/min. Due to chitosan being insoluble in basic pH levels, particles are essentially ‘pinched’ off from the original flow. This forms reproducible particles under 5 microns in size. Copper chitosan micro-particles were produced using the same protocol, but with copper chloride mixed with the chitosan.

A sample of micro-particles were reacted with 5-(dimethylamino)naphthalene-1-sulfonyl chloride (dansyl chloride, DNSC) to produce fluorescent particles. To do this, a 3 mL solution of concentrated micro-particles made and suspended in 50 mM NaOH was mixed with 1.5 mg of dansyl chloride and left at room temperature for 2 hours. The particles were then spun down using a centrifuge on the lowest setting for two minutes, to form a loose pellet. The supernatant containing excess dansyl was removed and the particles were resuspended with 50 mM NaOH. This process was repeated and the particles were mounted on microscope slide and sealed with a coverslip. A Zeiss Axiovert 200 microscope, outfitted with a QImaging Retiga EX digital camera and a filter cube to accommodate dansyl fluorescence (excitation filter, 350 nm, and emission filter, 500 nm-600 nm), was used to obtain a fluorescent image.

The nucleophilic attack of dansyl chloride by the amine group of chitosan can be seen in **Figure 1.3.1b**. The basic conditions can ensure the deprotonation of chitosan’s 1° amine and aid with deprotonation of the dansyl-chitosan 2° amine.

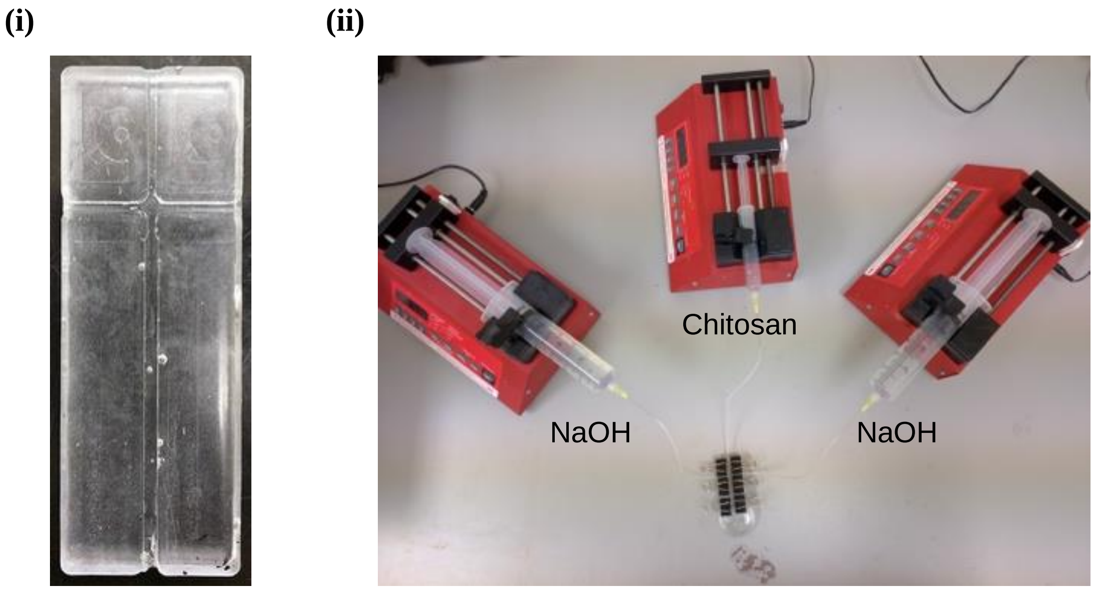

Figure 1.3.1a: Particle-producing apparatus.

(i) PDMS microfluidics apparatus for chitosan micro-particle production. Three reagent channels converge where the particles are formed and the resulting particle suspension exits out of the exit channel.

(ii) Assembled microfluidics apparatus. The PDMS apparatus is clamped between two glass slides. NaOH and a dilute chitosan solution is pumped into the apparatus via syringe pumps and the resulting solution is collected.

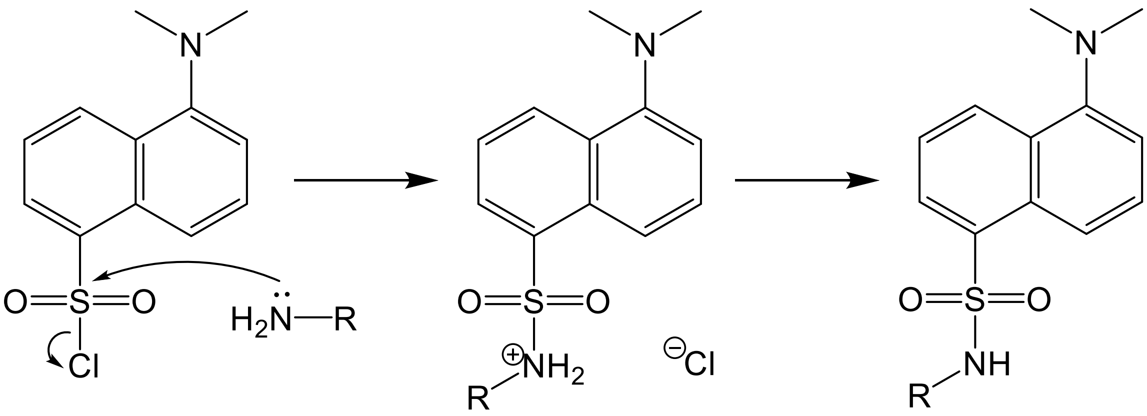

Figure 1.3.1b: Amine group of chitosan reacting with dansyl chloride. 2 hours RT, basic conditions.

1.3.2 Copper-Chitosan Milli-Particle Preparation

To produce copper chitosan milli-particles (Cu-chito), 2% (w/v) chitosan was allowed to mix with an excess of copper chloride ($CuCl_2$). The resulting Cu-chitosan complex was dissolved with the addition glacial acetic acid to obtain a concentration of 1% (v/v) acid. Excess Cu precipitate was allowed to separate from solution overnight and was discarded. This wait period also allowed for any incorporated air bubbles to be removed. Plain chitosan milli-particles (chito) were produced in an identical way but without adding $CuCl_2$, while the solution did not require removing precipitate, excessive air incorporated adds difficulty while producing the particles. Thus, minimal mixing was used or the solution was prepped and left to rest overnight.

The resulting viscous solution was dispensed via a 27G needle and a 10 mL syringe. A NE-300 Syringe Pump dispensed the solution so drops fell in a dropwise manner into a 1 M NaOH solution. The resulting spherical particles, Cu-chito or chito, were thoroughly rinsed with distilled water to remove excess base and left overnight in phosphate buffer (pH 7.4, 0. 1M). This is to reduce particle pH closer to neutral. The particles were rinsed again and dehydrated at room temperature. A count of 10 Cu-chito particles weighed in at 3.0 ± 0.03 mg with individual particles being <1 mm in diameter.

1.3.3 Nitric Oxide Detection

Authentic NO was detected using a Sievers NO analyzer (NOA, model 280i, GE Analytical Instruments, Boulder, CO, USA). The NOA 280i was set up using the standard NO_2^- measurement mode and standardized with NO_2^- according to manufacturer protocol.

Chitosan milli-particles were added to an excess amount of dithiothreitol (DTT) until the colour changed from dark purple to a pale yellow. This was done to reduce Cu(II) to Cu(I), allowing Cu to be in an active state. The particles were washed with 100mL of PBS to remove the excess DTT.

Chitosan (chito) or copper-chitosan (Cu-chito) particles of ~0.50 g, were placed in 22 mL screw cap vials, and were degassed under nitrogen for 5 minutes. 2 mL of 100 µM sodium nitrite ($NaNO_2$) ± 1 mM glucose was added. After allotted 15, 30, 45 or 60 minutes of reaction time had passed, 1.5 mL of headspace gas was removed with a 2.5 mL syringe (Hamilton 1000 Series Gastight Syringe) and injected into the NOA reaction vessel. The NOA reaction vessel was set up as per manufacturer's protocol. Control samples omitted chitosan particles. Results were obtained via NOA peak area and compared to a standard curve created by adding nitrite into I^-_3 (50 mg) in acetic acid (17.4M) described by Piknova *et al*.[41] All experiments were conducted in triplicate.

1.3.4 Cell Studies

Human retinal pigmented epithelium, ARPE-19 (ATCC® CRL- 2302TM) cells were purchased from ATCC (Manassas, VA, USA) and grown in Dulbecco's Modified Eagle Medium, Nutrient Mixture F-12 (DMEM/F12) supplemented with 10% fetal bovine serum (FBS) and 1% penicilium/streptomycin antibiotic solution, incubated at 37 °C with 5% CO_2.

ARPE-19 cells were used for scratch assays. They were plated in 6-well cell culture plates and grown to approximately 90% confluence. Using a rubber ended cell scraper, cells were removed to form a linear artificial wound. Data was organized by wound size. With the field of view taken into consideration, the average wound size was 1.8 mm^2, with the smallest being 0.8 mm^2 and the highest being 4 mm^2.

The milli-particle-bound Cu^{2+} was reduced with DTT, washed, and placed in sterilized polydimethylsiloxane (PDMS) cups with 40 µL of nitrite (100 µM NO_2^-) ± glucose (0.1 or 1.0 mM). The PDMS cups were produced following previous methodology of our group, as described in Faccenda *et al*.[42] The cups adhered to plate cover, and were suspended in the medium with ~2 mm clearance from well bottom. They were placed in the well approximately ~1 cm away from the center of the artificial wound (**Figure 1.3.4a (i, ii)**). NO as well as other gases like O_2, H_2S *etc.* freely diffuse through the PDMS, while salts and hydrophilic compounds like the nitrite and glucose do not.[42] Control samples refer to PDMS cup containing nitrite solution only.

A Zeiss Axiovert 200 microscope, outfitted with a QImaging Retiga EX digital camera, was used to take DIC cell images. The number of cells in the scratch wound area at 0 and 48 hours were compared and the net number of new cells was reported (**Equation 1.3.4a**). Images were obtained at 0 and 48 hours and the cell counts were calculated using Image-J software.

Equation 1.3.4a: $\boldsymbol{Net\ cell\ growth = Cell\ count_{48\ hrs} - Cell\ count_{0\ hrs}}$

(i)

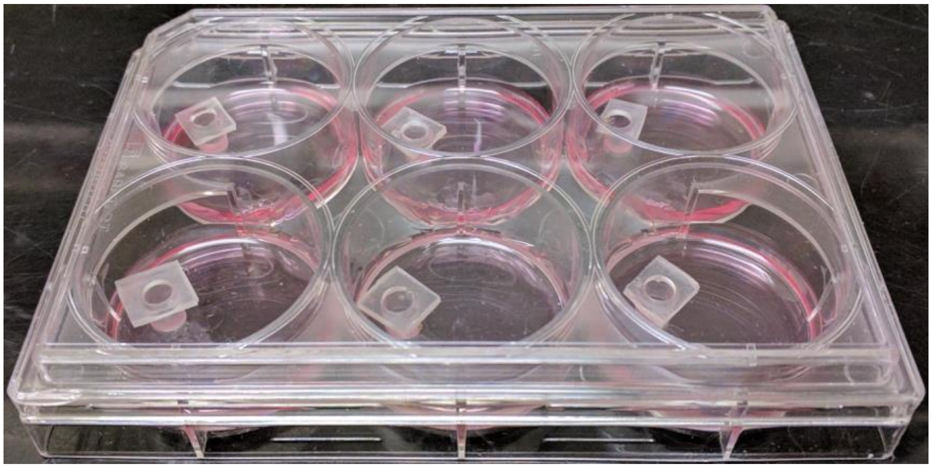

(ii)

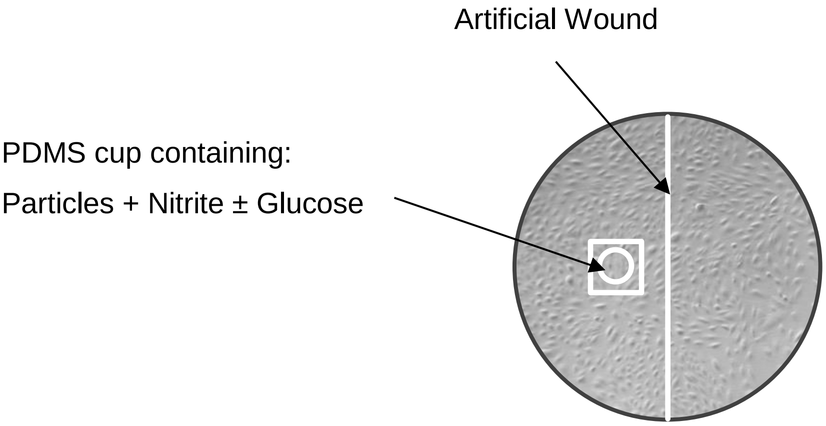

Figure 1.3.4a: Scratch assays with ARPE-19 mammalian cell culture.

(i) Particles with nitrite ± glucose confined by PDMS cups, adhered to plate cover, were suspended in the medium with ~2 mm clearance from well bottom.

(ii) An illustration of the relative position of the PDMS cups with respect to the artificial wound, which spanned the vertical length of each well.

1.3.5 Matrix Metalloproteinase (MMP) Activity

Gelatin zymography was utilized to identify matrix metalloproteinase-2 (MMP-2, gelatinase A) and -9 (MMP-9, gelatinase B). This technique can be used to identify the type of gelatinase, relative amount, and activation status (latent vs active).[43] Zymography works by impregnating the resolving layer of SDS-PAGE gels with the peptide substrate of the enzyme of interest. Protein in non-reducing conditions is electrophoresed. The gel is then incubated with the cofactors necessary for reaction to occur. Gelatinase activity is localized where the protein is present and white bands can be viewed upon distaining, in the areas where the gelatin was hydrolysed.

A standard gelatin zymography protocol (Abcam) was followed.[44] ARPE-19 cells were grown in 10 cm plates to 60% confluence. Using the width of a rubber ended cell scraper (1.7 cm), a vertical wound was made down the length of the plate. Removed cells and media was washed off with sterile PBS then grown with DMEM/F12 media lacking FBS. Cells were treated with 3 PDMS cups filled with their respective treatments, cups with 40 µL of nitrite (100 µM) ± glucose (1.0 mM) ± particles. After 48 hours, cell media was collected and analyzed via protocol. In overview: samples are run using non-reducing sample buffers on an SDS-PAGE gel co-polymerized with gelatin, SDS is washed out of the gel and it is incubated for 24 hours with the cofactors necessary to allow for gelatinase activity. The gel is then stained and destained, areas where the gel becomes clear is where the gelatin was hydrolysed by the enzymes. The bands appear as clear bands on blue background.

The resulting band area of each sample was processed through Image-J software. Values reported were normalized to the control data.

1.3.6 Statistical Analysis

Data was expressed as mean ± standard deviation. Two-tailed t-tests determined statistically significant differences at a 95% confidence interval. Statistical significance is determined by t being greater than the critical value (t > c.v.).

1.4 Results

1.4.1 Copper-Chitosan

The microfluidics apparatus was successfully used to make particles <10 microns in size with an apparent average of around 3 μm. The particles themselves are spherical and can be produced with and without copper. Shown in **Figure 1.4.1a (i)** is an image of copper-chitosan micro-particles made fluorescent by dansyl chloride. The particles are not considered robust, attempts to neutralize the pH result in dissolved particles and when left in their original basic media they aggregate relatively quickly. They are easy to produce when following protocol, however obtaining a large number of concentrated particles can take several days depending on the quantity desired. Immediate, unconcentrated particle solutions is suitable for imaging. Changing variables can change particle shape. For example, increasing the concentrations of chitosan produced varying shapes, such as longer cylindrical fibers (not shown).

The milli-particles, chito and Cu-chito, were used in experiments for NO detection, as well as for cell studies. The particles can maintain their integrity over several rounds of reduction with DTT and handling, thus they are considered relatively robust. In **Figure 1.4.1a (ii)**, there is visible swelling while the particles are hydrated, however upon dehydration they return to their original size. This swelling does not compare to the fully hydrated particles prior to being de-hydrated. These particles can be seen in **Figure 1.4.1a (iii-iv)**. After particles are reduced with DTT and washed, they can be left in a N_2-purged vial for several days before visible oxidation (green to blue colour change) is seen. In comparison, particles exposed to air will re-oxidize overnight. The shelf life of reduced particles could be increased by storing them in an inert atmosphere. Particles used for experiments were utilized immediately after the reduction and subsequent washes.

While milli-sized particles were successfully formed and utilized, copper-chitosan can be manipulated in a variety of ways to increase functionalization and application potential. Copper-chitosan micro-particles were produced using microfluidic techniques and the milli-particles can be ground into a fine powder. This could allow for incorporation into gels, creams, eye drops, wound washes, or other forms of topical application. Copper-chitosan can also be made into a film (not shown), for incorporation onto biomedical devices or wound dressings. As well, it can be fixed onto gauze (shown), for uses as a wound dressing; preliminary gauze NOA 280i experiments showed that copper gauze is capable of NO release (not shown). **Figure 1.4.1a (v)** shows some of these forms of chitosan, including milli-particles, chitosan powder, and copper-chitosan fixed onto gauze.

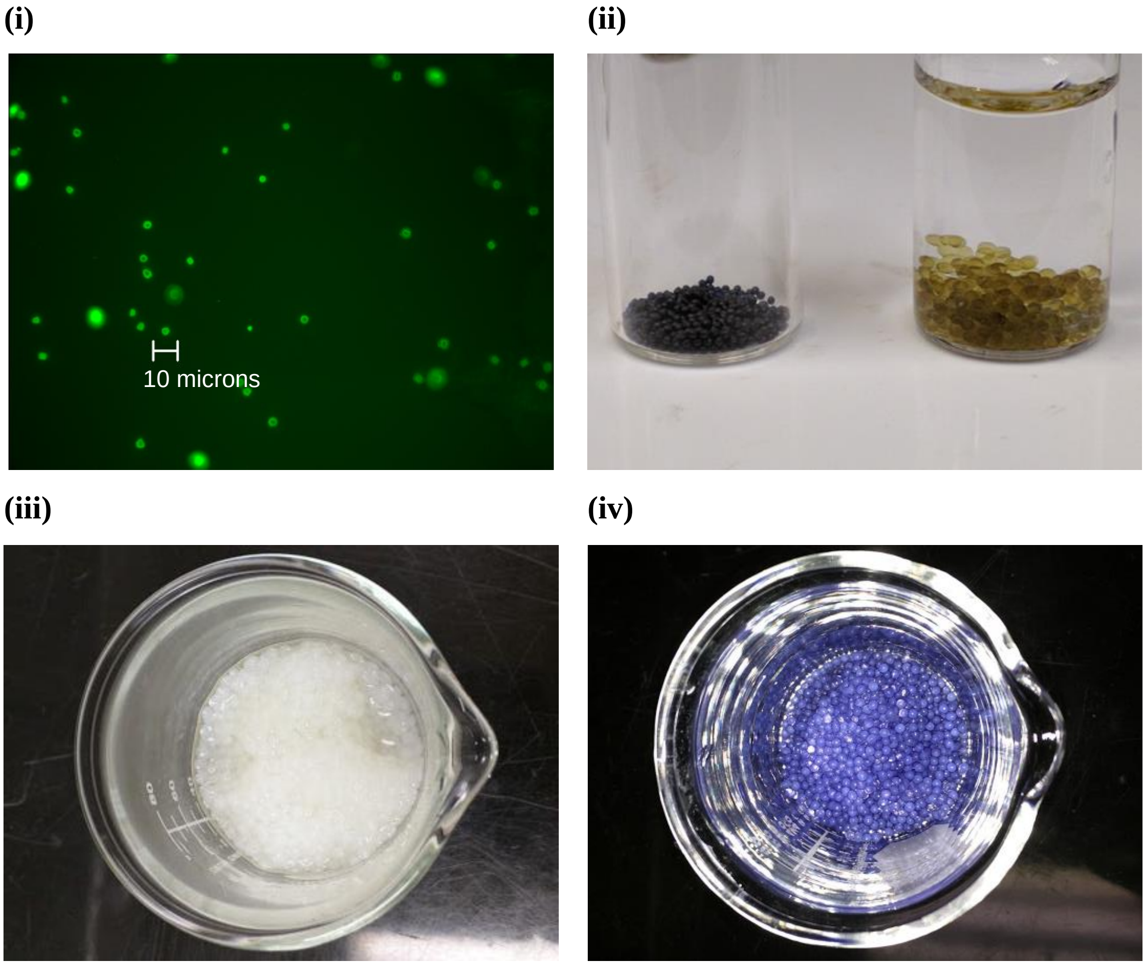

Figure 1.4.1a (i-iv): Various forms of chitosan and copper chitosan.

(i) Fluorescent microscope image of copper-chitosan micro-particles, taken after a reaction with dansyl chloride.

(ii) Left: copper-chitosan milli-particles. Right: copper-chitosan milli-particles after Cu^{2+} was reduced to Cu^{1+} by 0.5 M DTT in H_2O; the particle size increases significantly due to hydration during the reduction process.

(iii) Freshly prepared chitosan (chito) milli-particles, fully hydrated and not yet dried for use. Shown in 100 mL beaker.

(iv) Freshly prepared copper-chitosan (Cu-chito) milli-particles, fully hydrated and not yet dried for use. Shown in 100 mL beaker.

(v)

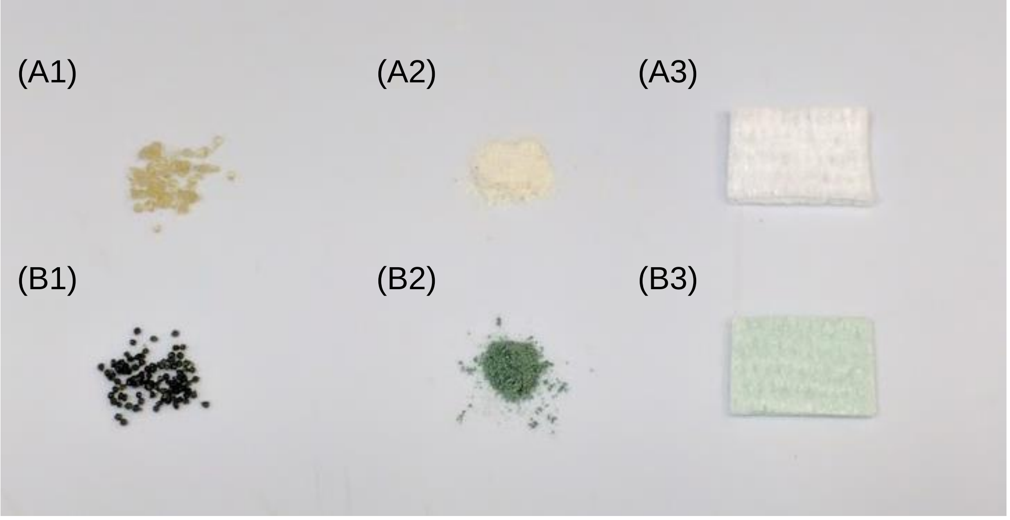

Figure 1.4.1a (v): Various forms of chitosan and copper chitosan.

(v) (A1) Chitosan milli-particles

(A2) Chitosan powder

(A3) Untouched gauze

(B1) Copper-chitosan milli-particles

(B2) Copper-chitosan milli-particles ground into a powder

(B3) Copper-chitosan fixed onto gauze.

1.4.2 Nitric Oxide Detection

The Sievers NOA 280i was used to demonstrate that the Cu-Chito milli-particles ± glucose can produce authentic NO. In these experiments, the milli-particles + nitrite ± glucose were placed in degassed gas-tight vials, three vials at each time point, and each vial was only sampled once at 15 minute intervals up to 60 min. The graphical results at the various time points can be seen in **Figure 1.4.2a (i)**. Peak data was converted to nmol amounts of NO per gram of milli-particles and adjusted for the total headspace of each reaction vial. Each sample, including the control samples, contained 100 µM NO_2^- ± 10 mM glucose. In **Figure 1.4.2a (ii)** the data is represented as the rate of NO produced/min. As indicated in **Figure 1.4.2a**, the milli-particles did produce NO. The level of NO detected by Cu-chito treatments in the presence of glucose did not result in statistically significant differences in comparison to the Cu-chito treatments without glucose present.

The NO production rate plot (**Figure 1.4.2a (ii)**) was more revealing of the reaction dynamics. The maximum rate of NO production was ~ 1.40 nmol/min (Cu-chito) and 1.08 nmol/min (Cu-chito + glucose). Beyond this point the NO production rate steadily decreased to ~0.24 nmol/min (Cu-chito) and ~0.27 nmol/min (Cu-chito + glucose).

(i)

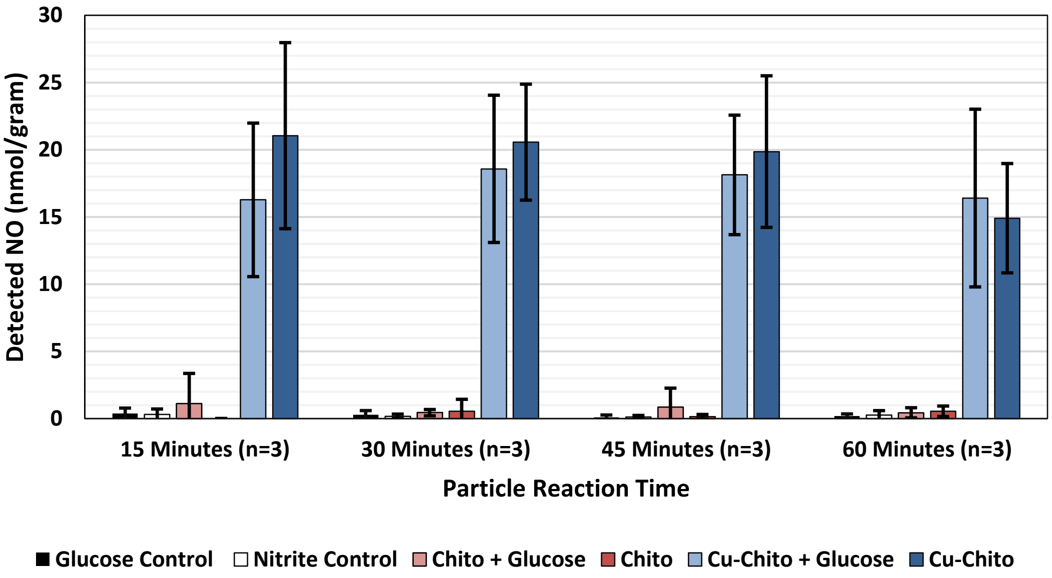

(ii)

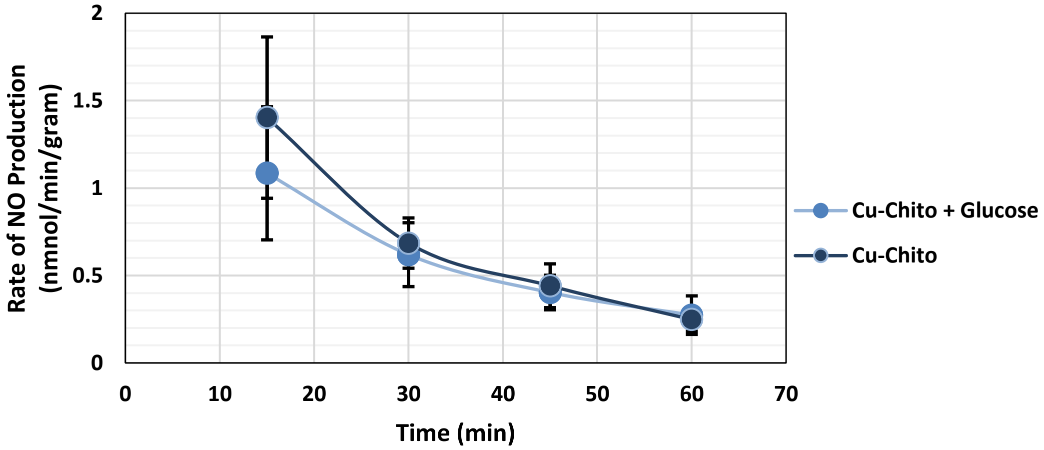

Figure 1.4.2a: NO signal detected by chitosan milli-particles as observed by the Sievers NOA 280i. Active particles were left to react with 100µM nitrite ± 1.0mM glucose, with gas samples were taken every 15 minutes from separate vials *i.e*. each vial at each time point was sampled only once.

(i) Values represent nmoles of NO produced in the total headspace (20 ml) of reach reaction vial, adjusted for particle mass.

(ii) The data expressed as rate of NO produced by Cu-chito and Cu-chito + glucose over sampling time.

1.4.3 Cell Studies

Scratch assays were performed in order to simulate an *in vitro* wound model, in order to test our novel NO releasing particles. They can provide insight into cell–matrix and cell–cell interactions, cell migration, cell proliferation, and can mimic cell migration during wound healing. The data collected here provides the net number of new cells in the wound area, with the data collected at 0 hours and 48 hours. The various cell treatments, of nitrite ± Cu-chito or chito, and ± glucose, were prepared into a PDMS cup and placed with the cell for the duration of the 48 hours.

The scratch assay experiments were conducted using ARPE-19 mammalian cell culture. The reagent controls (nitrite ± glucose) and the NO generation system (chito or Cu-chito with nitrite ± glucose) were isolated from the cells by placing them inside of PDMS cups (**Figure 1.3.4a (i, ii)**) which are impermeable to ionic and hydrophilic molecules but allow gases such as NO to pass through. **Table 1.4.3a** displays the number of new cells grown in the wound for each treatment type.

Overall, the Cu-chito showed an increase in number of cells in the wound, with around ~200-300 new cells more than the controls. Using a 95% confidence interval, this is considered statistically significant. This result is very promising, especially since the chito particles without copper only showed around 0-40 new cells in comparison to the controls, which is statistically insignificant. To visualize the effect of the Cu-chito particles, **Figure 1.4.3a** compares 0 hours to 48 hours on the number of cells, for data with a wound size of 1.8 mm^2.

The data in **Table 1.4.3a** also reveals the difference between having glucose present or absent. With glucose, Cu-chito treatments showed an increase of 152% more cells in the wound in comparison to control groups, while Cu-chito treatments with nitrite alone showed 130% more cells in the wound. In comparison to each other, the Cu-chito with glucose treatments displayed a significant increase of ~118% more cell cells in the wound in comparison to treatment of Cu-chito and nitrite. However, Cu-chitosan with 0.1 mM glucose vs. 1 mM glucose were statistically insignificant in comparison to each other. This is not completely unexpected, since both their concentrations are large; this indicates that 0.1 mM or less of glucose may be sufficient to elicit a similar response.

We also wanted to see if the effect of particle-generated NO would have a different effect depending on the size of the manually-obtained wound. To do this we created a distribution of pseudo-wounds wound areas ranging from 0.8 mm^2 to 4.0 mm^2. To further analyze the effect wound size had on the effectiveness of the Cu-chito treatments, the data was reorganized by the wound size and further analyzed with two-tailed t-tests for statistical significance. The control and Cu-chito data is reorganized by wound size in **Figure 1.4.3b**, with the corresponding statistical information shown in **Table 1.4.3b**.

Table 1.4.3a: Scratch assay results with ARPE-19 mammalian cell culture. Various treatment types of chitosan milli-particles and the net number of new cells after 48 hours. Statistical comparison is to the control data. Two tailed t-test: statistical significance is determined by t being greater than the critical value (t > c.v.). Number 'n' refers to number of data values used.

Treatment Type:	New Cell Count:	95% Confidence Interval:
Control (n=72)	588.6 ± 181.1	
Cu-Chito (n=54)	763.9 ± 231.3	Significant (4.8 > 2.0)
Cu-Chito + 0.1 mM Glucose (n=48)	898.0 ± 219.4	Significant (8.3 > 2.0)
Cu-Chito + 1.0 mM Glucose (n=54)	874.9 ± 173.7	Significant (8.9 > 2.0)
Chito (n=24)	621.7 ± 154.5	Not Significant (0.8 < 2.0)
Chito + 0.1 mM Glucose (n=24)	610.0 ± 257.0	Not Significant (0.4 < 2.0)
Chito + 1.0 mM Glucose (n=24)	583.1 ± 215.4	Not Significant (-0.1 < 2.0)

(i) Nitrite Control

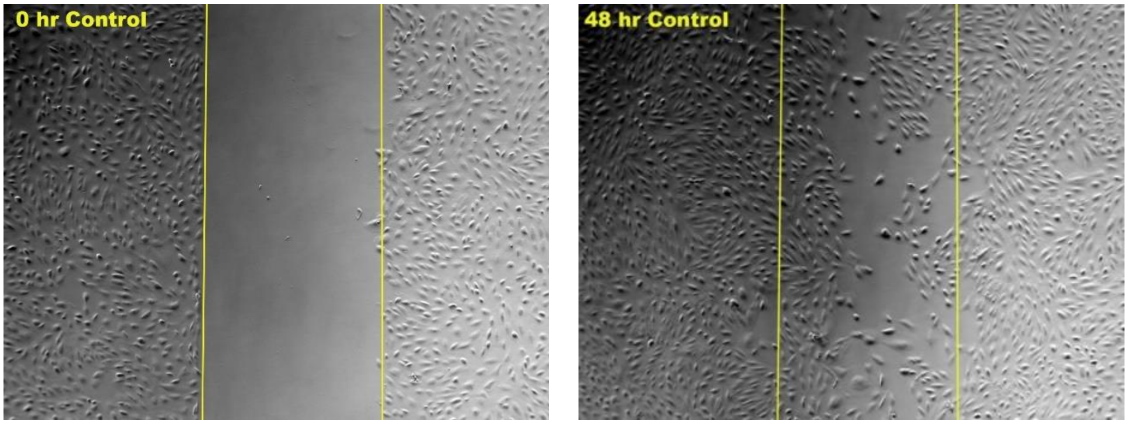

(ii) Cu-Chito + Nitrite

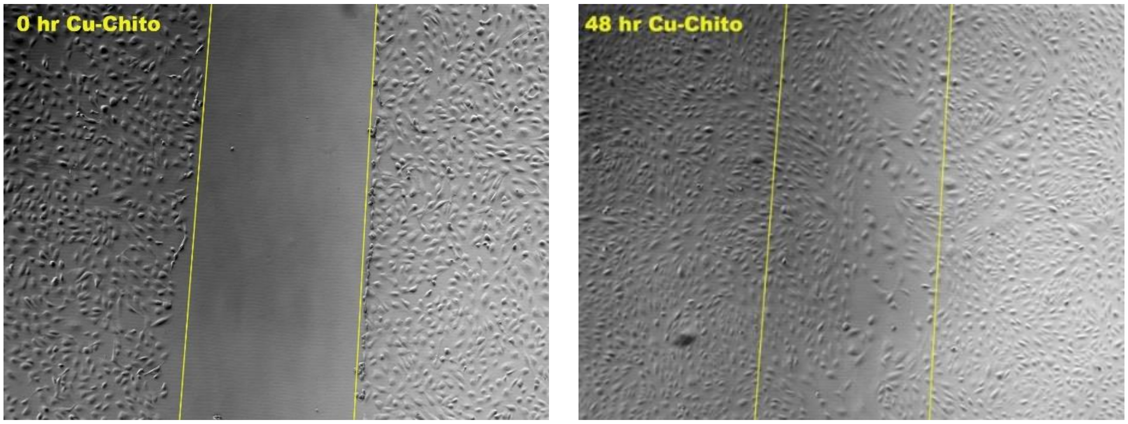

Figure 1.4.3a (i-ii): Representative scratch assay images for pseudo-wounds of 1.8 mm^2 in size. Reported as the difference in number of cells at 0 and 48 hours, as counted by ImageJ:

(i) Nitrite Control sample- net number of new cells: 588.6 ± 181.1 cells

(ii) Cu-Chito + Nitrite treatment- net number of new cells: 763.9 ± 231.3 cells

(iii) Cu-Chito + Nitrite + 0.1 mM Glucose

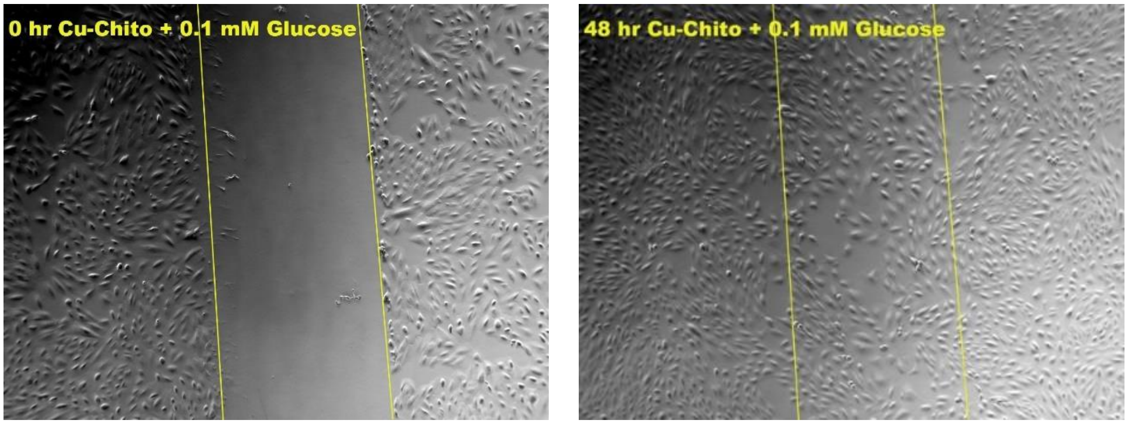

(iv) Cu-Chito + Nitrite + 1.0 mM Glucose

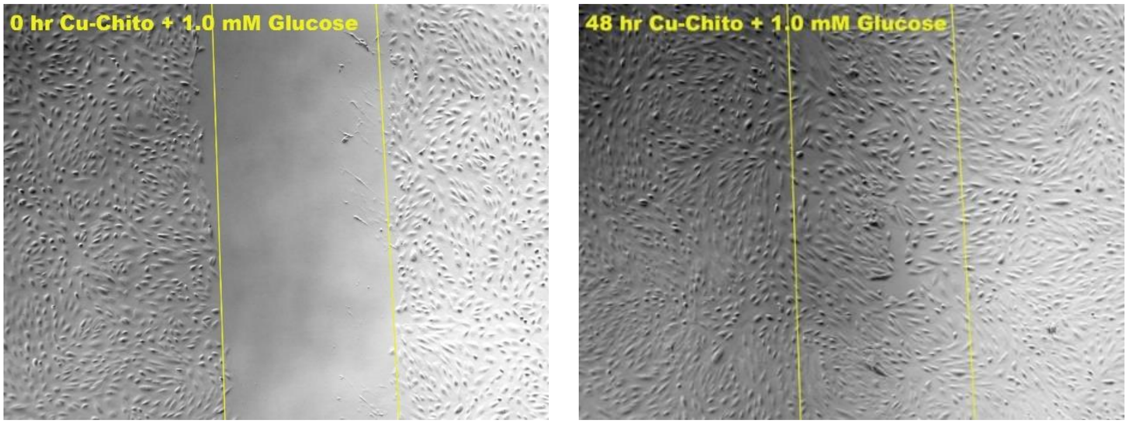

Figure 1.4.3a (iii-iv): Representative scratch assay images for pseudo-wounds of 1.8 mm^2 in size. Reported as the difference in number of cells at 0 and 48 hours, as counted by ImageJ:

(iii) Cu-Chito + Nitrite + 0.1mM glucose treatment- net number of new cells: 898.0 ± 219.4 cells

(iv) Cu-Chito + Nitrite + 1.0mM glucose treatment- net number of new cells: 874.9 ± 173.0 cells

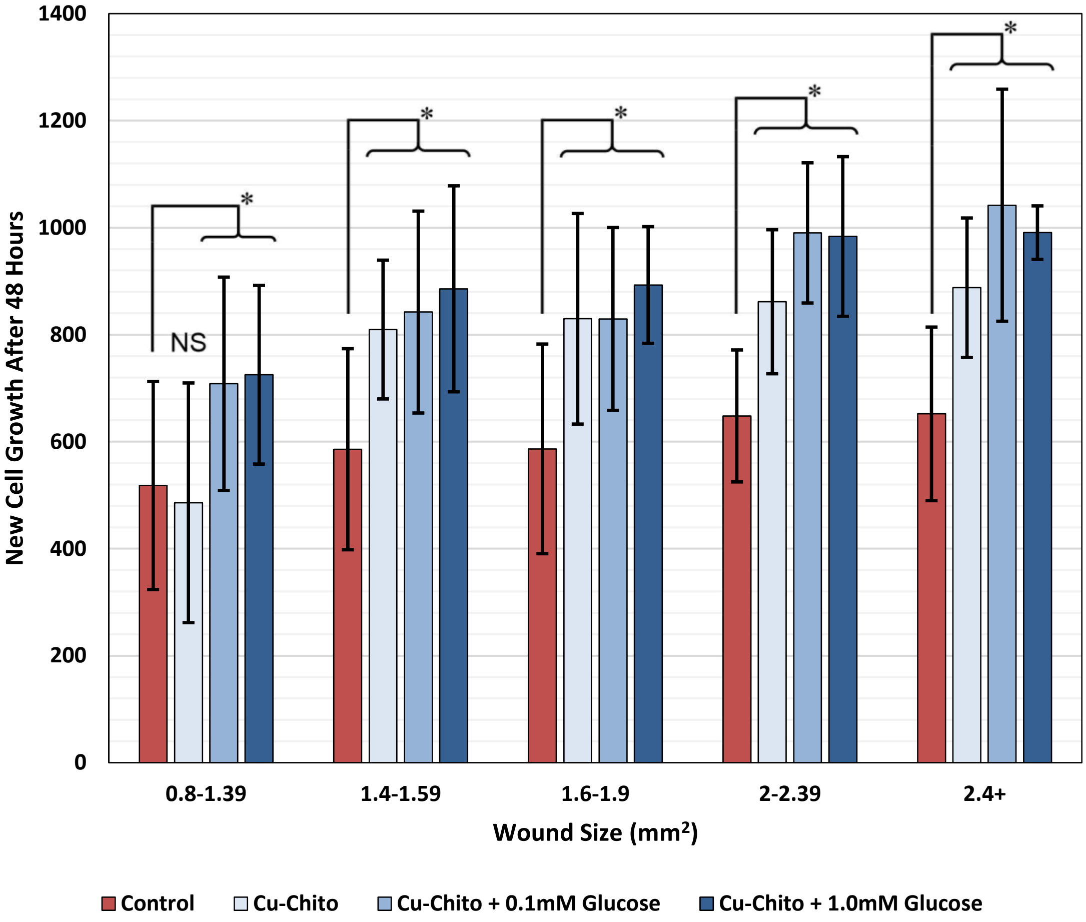

Figure 1.4.3b: Cu-chito scratch assay results, organized by wound size. The Cu-chito (nitrite ± glucose) data sets are compared to the respective control (nitrite) data. The net number of cells in the wound at 48 hours is shown, with the data sets organized by increasing wound size analyzed. (Note: * indicates significance in comparison to the respective control data at a 95% confidence interval; NS = not significant. Statistics displayed in **Table 1.4.3b**)

Table 1.4.3b: Statistics for scratch assay results, with data organized by wound size. Various treatment types of chitosan milli-particles and the net number of new cells after 48 hours. Statistical comparison is to the respective control data. Two tailed t-test: statistical significance is determined by t being greater than the critical value (t > c.v.). Number 'n' refers to number of data values used.

Wound Size:	Treatment Comparisons:	95% Confidence Interval:
0.80-1.39 mm^2	Control (n=21) Cu-Chito (n=13)	Not Significant (0.4 < 2.0)
	Control (n=21) Cu-Chito + 0.1 mM Glucose (n=10)	Significant (2.5 > 2.00)
	Control (n=21) Cu-Chito + 1.0 mM Glucose (n=13)	Significant (3.1 > 2.0)
1.40-1.59 mm^2	Control (n=13) Cu-Chito (n=7)	Significant (2.8 > 2.1)
	Control (n=13) Cu-Chito + 0.1 mM Glucose (n=7)	Significant (3.5 > 2.1)
	Control (n=13) Cu-Chito + 1.0 mM Glucose (n=14)	Significant (4.0 > 2.0)
1.60-1.90 mm^2	Control (n=12) Cu-Chito (n=16)	Significant (3.2 > 2.0)
	Control (n=12) Cu-Chito + 0.1 mM Glucose (n=10)	Significant (3.0 > 2.0)
	Control (n=12) Cu-Chito + 1.0 mM Glucose (n=13)	Significant (4.9 > 2.0)
2.00-2.39 mm^2	Control (n=11) Cu-Chito (n=9)	Significant (3.7 > 2.1)
	Control (n=11) Cu-Chito + 0.1 mM Glucose (n=8)	Significant (5.8 > 2.1)
	Control (n=11) Cu-Chito + 1.0 mM Glucose (n=8)	Significant (5.3 > 2.1)
2.40+ mm^2	Control (n=14) Cu-Chito (n=11)	Significant (3.9 > 2.0)
	Control (n=14) Cu-Chito + 0.1 mM Glucose (n=13)	Significant (5.3 > 2.0)
	Control (n=14) Cu-Chito + 1.0 mM Glucose (n=6)	Significant (5.0 > 2.1)

1.4.4 Gelatin Zymography for MMP Activity

Samples processed by gelatin zymography immediately after the 48 hour treatments can be seen in **Figure 1.4.4a (i-ii)**. With the area of each band normalized to the nitrite control, the results show a 60% increase in MMP activity after Cu-chito and Cu-chito + glucose treatments. The 73 kDa band was used for this measurement due to the clear affect that the particle treatments displayed. With the nitrite control being set to 100 ± 13%, the water control compared at 99 ± 26%. Cu-chito displayed 164 ± 26% and Cu-chito with glucose added displayed 160 ± 5% of the nitrite control. The quantification of the band density is summarized in **Figure 1.4.4a (iii)**.

Further differences between the control samples and the copper particle samples is the presence of more bands displaying gelatinase activity. The copper particle treatments appear to induce other gelatinase enzymes, with a somewhat defined band appearing at 86 kDa. This band was not seen in comparison to control samples. The molecular weight (MW) of this band, along with the prominent 73 kDa band, was calculated using the molecular weight (MW) ladder, which appears on the left of each gel image. This was done using a log(MW) Vs R_f graph (not shown).

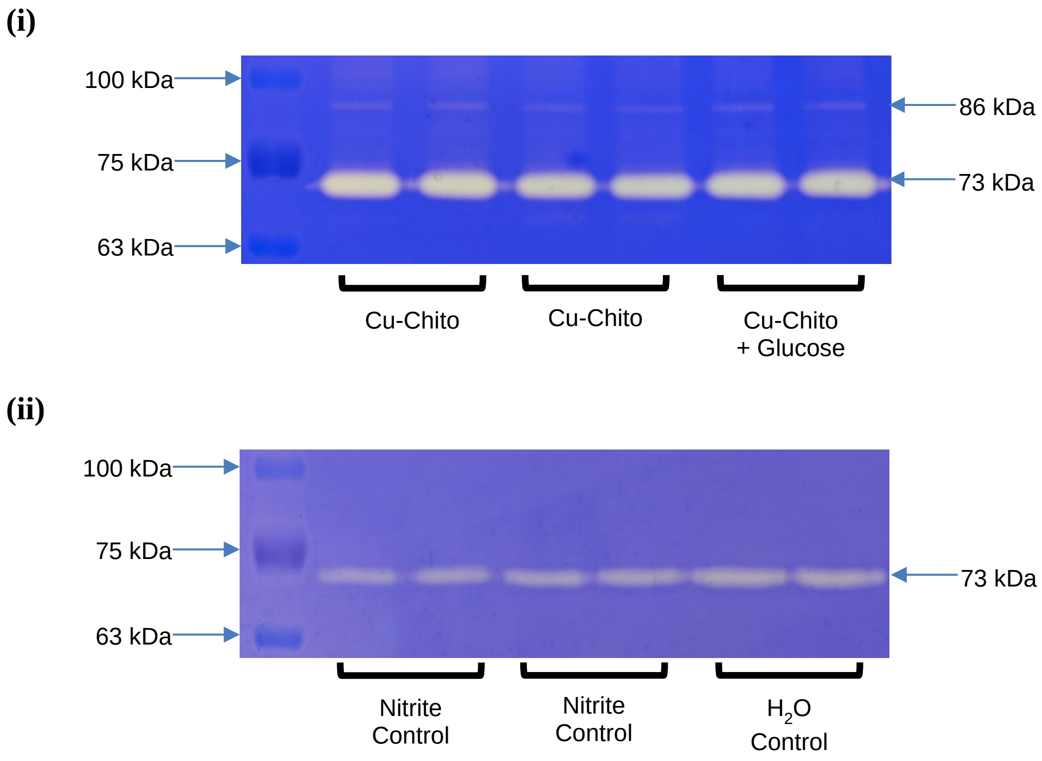

Figure 1.4.4a (i-ii): MMP activity via gelatin zymography.

(i) Zymography gels of copper-chitosan milli-particle treatments. Left to right, the gel lanes contain prestained protein ladder, followed by two Cu-chito with nitrite samples and one Cu-chito with nitrite and glucose sample, run in duplicate.

(ii) Zymography gels of control treatments. Left to right, the gel lanes contain prestained protein ladder, followed by two nitrite control samples and one water control sample, run in duplicate.

(iii)

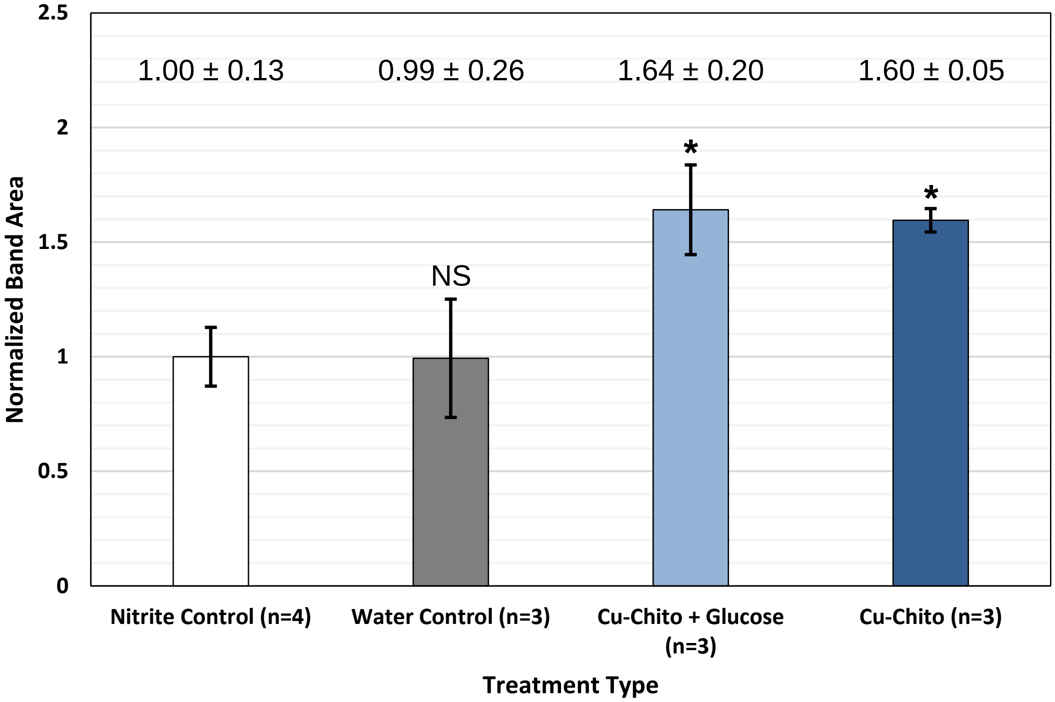

Figure 1.4.4a (iii): MMP activity via gelatin zymography.

(iii) Band densities of bands located at 73 kDa, calculated using ImageJ. Data is normalized to the nitrite control data. Samples were processed immediately after their respective 48 hour treatments. (Note: * indicates significance in comparison to nitrite control data at a 95% confidence interval; NS = not significant)

1.5 Discussion

This is a study into the production of a novel NO releasing particles at the milli and micro scale, using chitosan as a matrix for a copper catalyst. The milli-sized particles were tested for the authentic production of NO using the NOA 280i and underwent testing in an *in vitro* wound healing model. In addition to scratch assays, matrix metalloprotease enzymes were chosen as an extracellular target to observe the effect of the NO treatments.

1.5.1 Nitric Oxide Detection

NO production was detected by taking readings of the headspace gas of sample-containing vials. Copper containing particles successfully produced detectable NO gas over the course of an hour, while controls and particles lacking in a copper aspect produced comparatively minimal signals.

Beyond this, there are a couple of interesting takeaways that the data provides. First, the presence of glucose had a statistically insignificant effect. Glucose neither helps nor hinders the NO production potential exhibited by the particles. This may be attributed to the short time scale that the reaction was monitored and overall does not disprove the theory that glucose could aid in catalytic turnover over time.

As well, while the copper samples give consistent readings in the range of 15-20 nmol/g, the rate of NO production over time decreases over the course of the hour. One reason for this could be the closed system that the readings were taken. In this closed system, NO could be reacting with Cu^{2+} and being converted back to nitrite; this has been demonstrated by Sarma & Mondal.[45] Since $NO_{(g)}$ (the detected species) is in equilibrium with $NO_{(aq)}$ this leads to a suppressed value of the NO produced by the particles, in comparison to its maximum potential. This equilibrium is shown in **Equation 1.5.1a**. This situation is not expected to occur in the wound healing cell model used, as the $NO_{(g)}$ generated would diffuse away to induce cellular signaling. With $NO_{(g)}$ being removed from the equation, the reaction would be pushed towards the product side.

Equation 1.5.1a:

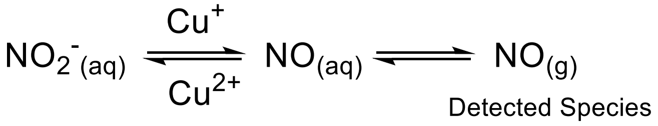

$$NO_2^-{}_{(aq)} \underset{Cu^{2+}}{\overset{Cu^+}{\rightleftharpoons}} NO_{(aq)} \rightleftharpoons \underset{\text{Detected Species}}{NO_{(g)}}$$

1.5.2 Cell Studies

Interesting patterns arose when comparing wound size. The graph (**Figure 1.4.3b**) shows how the two glucose treatments remain similar at every size point. The Cu-chito remains competitive with glucose treatments for sizes 1.4-1.9 mm^2. If wound sizes remained in this range, the effect of glucose would remain inconclusive. At sizes 2 mm^2 and higher, with more room for cells to grow, glucose treatments show increased number of new cells in the wound suggesting that, as we postulated, sustained NO production can be maintained as long as there is sufficient glucose present to recycle the oxidized copper. Unfortunately, we could not demonstrate the sustained NO released from the particles with the closed discontinuous system for NOA detection of NO. It is possible to use the NOA 280i for live NO readings and this has been done[46], however would require building a gas tight chamber for the cells to incubate, with 5% CO_2 incoming and all air being fed into the machine for NO detection.

The effect of glucose is seen in this data. Cu-chito treatments that combined nitrite and glucose had a significant increase in new cells in the wound in comparison to treatments with nitrite alone. Cu-chito without the addition of glucose grew an average of 170 more cells per experiment than the control experiments. Whereas Cu-chito with the presence of glucose grew an average of 300 more cells per experiment, compared to the nitrite control (data can be observed in **Table 1.4.3a**). This is determined as statistically significant, with a two tailed t-test comparing these values (data not shown). Thus, it supports our hypothesis that the addition of glucose aids in the production of NO.

1.5.3 MMP as a NO Sensor

The technique of gelatin zymography is used to identify the activity of MMP-2 and MMP-9, both of which have gelatinase activity. Due to the correlations between NO and MMP activity, this was chosen to observe the changes that the Cu-chito treatments can enact on an enzymatic level. Zymography gels can theoretically be used to identify the type of gelatinase, relative amount, and activation status (latent vs active).[43] In order to accurately identify activation status, an internal standard is required. Options for this include conditioned medium from HT1080 human fibrosarcoma cells, which contains MMP-2 (72kDa) and MMP-9 (92kDa).[43] If these cells undergo treatment, the media can also contain active MMP-2 (62 kDa), another option is using purified protein, if available. Active MMP-9 is 82 kDa.

There are also intermediate inactive forms of MMP-2 (64 kDa) and MMP-9 (85 kDa), and the possibility of low-weight active forms of MMP-2 (45 kDa) and MMP-9 (67 kDa). Viewing all these forms is possible do the SDS in the gel and in the sample buffer that works to unfold the protein in a way that exposes the active site and allows for activity.[43] The intermediate inactive form is found when samples contain endogenous tissue inhibitors of metalloproteinases (TIMPs); this band would be difficult to isolate due to the small difference in size to the respective active species. Low-weight active forms become an issue when protein samples are purposefully treated to obtain the active forms and are overexposed to the treatment.[43] Since our samples are not obtained from a tissue, nor are they purposely treated, bands in these locations are not expected to occur.

The copper containing samples displayed a marked increase in the protein observed. The band that best observes this change was the one seen at 73 kDa, since this band also appeared in the control samples (**Figure 1.4.4a (i)**). This is likely inactive MMP-2, based on size. Copper samples also displayed a distinctive peak at 86 kDa which could correspond to a form of MMP-9 (**Figure 1.4.4a (i)**). To truly confirm the identity of the present enzyme, the use of an internal standard may be necessary. Otherwise techniques such as immunoblotting could be used. In terms of true quantification, ELISA assays would be the gold standard. To determine if expression levels is the cause of increase in MMP activities, reverse transcription polymerase chain reaction (RT-PCR) would have to be utilized.[47-48]

The mechanism of change that NO effects in MMP’s can vary by MMP type or on the cell or tissue type in question. Studies suggest that NO effects activation of MMP’s through S-nitrosylation.[49] Some research on human cells include rheumatoid synovial cells, where NO has be found to increase the expression levels of MMP-2.[50] It was found that MMP-2 is regulated by NO in fibrosarcoma epithelial cancer cells.[51] MMP-9 in human placental tissue is activated by NO; with patients with gestational and pre-existing diabetes mellitus having reduced activity of the enzyme, due to the reduction of NO.[52] NO effects MMP-9 in airway epithelial cells through an expression and activation; the use of NO donors in this study was found to promote wound repair through these methods.[53]

While its is entirely possible that the ARPE-19 cells are reacting to the NO stimulation through an increase in MMP expression, the experimental work done cannot confirm this mechanism of action. With the evident increase in activity, S-nitrosylation activation is the simplest explanation.

In regards to this project itself, the fact that these changes are observed at the 48-hour mark indicate that the nitric oxide supplement via copper chitosan particles is providing long-lasting effects.

1.6 Conclusion

By complexing copper with chitosan polymer, nitric oxide releasing derivatives have been developed. Copper-chitosan micro- and milli- particles were produced using microfluidic techniques. Authentic nitric oxide production from copper-chitosan milli-particles was observed using the Seivers Nitric Oxide Analyzer 280i. *In vitro* scratch assays with the ARPE-19 cell line resulted in an increase of cell new cells in the wound after treatment with the copper-chitosan milli-particles, as well as an even higher increase in cell new cells by supplementing glucose in the particle treatment. Using the activity of MMP proteins as a NO sensor resulted in Cu-chito treatments showing a 60% increase in cellular enzymatic activity in comparison to controls; the influence of NO can be observed at least up to the end of the 48-hour treatment.

There are many applications for the technology presented here. The size of the nitric oxide releasing micro-particles would allow for use in gels, creams, eye drops, wound washes, or other topical applications for a wound. Copper chitosan could be incorporated directly onto biomedical devices, or a wound dressing, gauze or otherwise. Our technology utilizes a minimal number of easily accessible, low-cost, components, as well as a minimally complex system for forming particles that can easily be adapted to an industrial setting. This puts our technology at a clear advantage in comparison to other NO releasing systems, for example, those that use NO donor compounds or other drugs that have to be independently synthesized.

1.7 Future Directions

Future work that could benefit this project includes battling the logistics of taking live readings of NO output over a greater period of time. Being able to assess the quantity of NO that the mammalian cells are utilizing versus how much is being outputted total would benefit in assessing the concentration of NO that would benefit the cells without releasing a concentration that becomes needlessly toxic. In addition, monitoring other extracellular effects would add useful insights to the effects of the treatments. The complications with this include the ability to measure endogenous proteins. Past work in this regard includes Western blot assays utilizing antibodies (Santa Cruz Biotechnology) that target fibroblast growth factor 2 (FGF-2) and vascular endothelial growth factor (VEGF), to no success in identifying the proteins at endogenous levels. Optimizing these experiments or pursuing different routes, including routes that take a closer look at MMP levels, is a possible future direction. Performing a Western blot while probing for S-nitrosocysteine residues may be of interest.

CHAPTER 2: Study into an Allosteric Site of S-nitrosoglutathione Reductase (GSNOR)

2.1 Chapter Summary

S-nitrosoglutathione (GSNO), an endogenous S-nitrosothiol (SNO), plays a prominent role in nitric oxide (NO) signaling and bioavailability. S-nitrosoglutathione reductase (GSNOR) is the enzyme responsible for its metabolism. Due to this, GSNOR's activity has a strong influence on SNO-protein levels. As such, furthering the understanding of GSNOR's regulatory mechanisms is of great interest. Our group has noted a sigmoidal deviation in GSNOR's steady state kinetics, in regards to GSNO concentrations. Our kinetic analysis yields a sigmoidal curve with a Hill coefficient (n) of 1.49 ± 0.037; indicating positive allostery. Molecular docking (MD) simulations were performed and implicated the amino acid residues Gly321, Lys323, Asn185, and Lys188 in the binding of an allosteric GSNO; in a location adjacent to GSNOR's structural zinc atom. To further these studies, time-resolved electrospray (TRESI) microfluidics set up was utilized to perform hydrogen / deuterium exchange (HDX) mass spectrometry (MS) experiments. With a two second HDX reaction time, the peptides containing the residues Gly321, Lys323, and Lys188 displayed a decrease in deuterium uptake of 1.4%, 1.4%, and 0.4%, respectively. These changes were calculated as the difference in deuterium uptake after the inclusion of GSNO in the GSNOR protein solution. This offers insight into the interactions of GSNO at these amino acid residues and ultimately supports the location of the allosteric site proposed by the MD studies.

2.2 Introduction

2.2.1 GSNOR as ADH5

S-nitrosoglutathione reductase (GSNOR) is an alcohol dehydrogenase class-3 (AHD-3) enzyme encoded by the ADH5 gene, located on the reverse strand of chromosome 4 (4q23 – chr4:99993567 – 10000985).[54] Sometimes referred to as ADH5, GSNOR has several other aliases and functions beyond its role in metabolizing the substrate S-nitrosoglutathione (GSNO).[55]

Another main role of GSNOR is to act as a glutathione-dependent formaldehyde dehydrogenase (GSH-FDH, FALDH).[56] ADH5 is critical in the metabolic elimination of formaldehyde. Formaldehyde can react with glutathione to form S-(hydroxymethyl)glutathione (HMGSH) and from there ADH5 can oxidise it to S-formylglutathione, this process is shown in **Figure 2.2.1a**. S-formylglutathione can then go on to undergo hydrolysis via S-formylglutathione hydrolase to produce formic acid and to regenerate GSH.[57] ADH5 requires the cofactor NAD^+ for this function and results in the formation of NADH, the cofactor required for GSNO reduction.

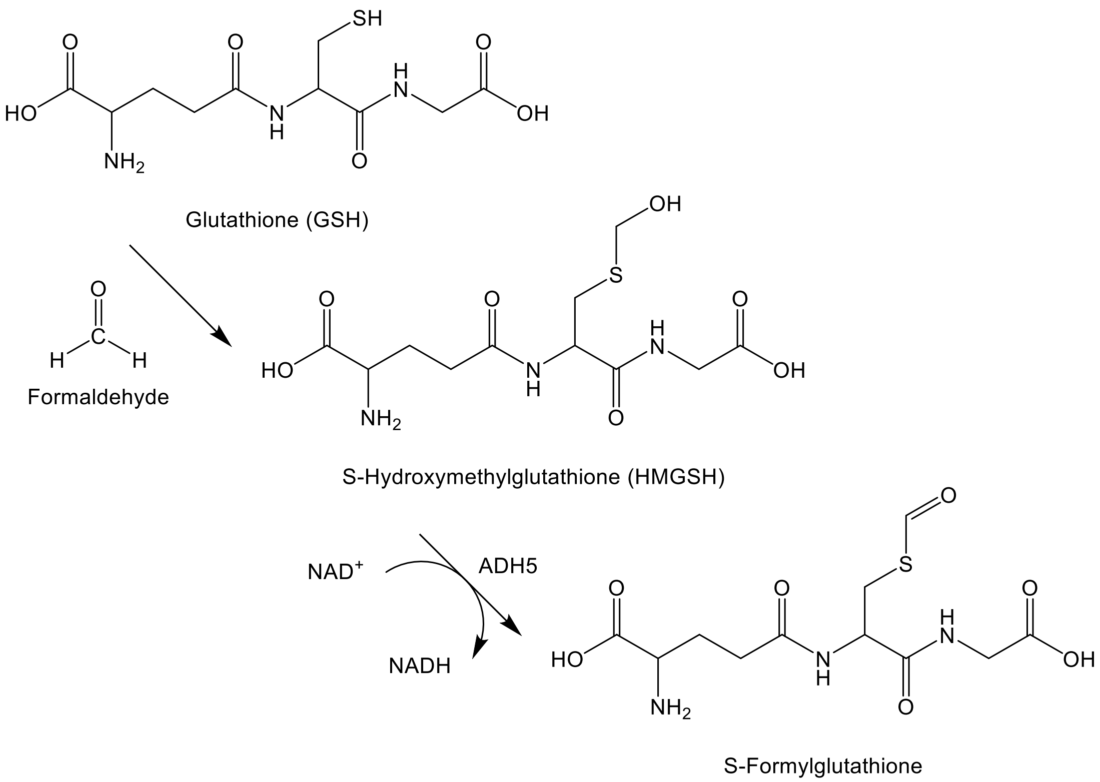

Figure 2.2.1a: ADH5 and its role in formaldehyde detoxification. GSH reacts with formaldehyde to produce HMG. ADH5 can then oxidise HMGSH to form S-formylglutathione. S-formylglutathione is then hydrolyzed via S-formylglutathione hydrolase to reobtain GSH (not shown).

Other synonyms for GSNOR include chi polypeptide, and AHDX, FDH, and HEL-S-60p. Despite being an alcohol dehydrogenase, ADH5 has a low affinity for ethanol, preferring instead to perform the oxidation of long-chain primary alcohols (with a preference with a double bond located in the β position), complex alcohols of high molecular weight, and omega-hydroxy fatty acids.[58]

GSNOR is found in both prokaryotic and eukaryotic organisms, and highly conserved across most vertebrate species.[59] GSNOR plays an important role in plants, the enzyme is necessary for normal growth and development.[60] *Arabidopsis thaliana* plants occupies much of the plant GSNOR research available, however there has also been work involving peas (*Pisum sativum* L.), pepper (*Capsicum annuum* L.), sunflower (*Helianthus annuus* L.), the fungus *Plasmopara halstedii*, as well as maize and rice.[60] GSNO's role in S-nitrosothiol formation, the formation of reactive nitrogen species (RNS), and its ability to influence NO homeostasis, plants are at a severe disadvantage if they display atypical GSNOR activity or expression.

In human tissue, ADH5 displays ubiquitous expression. Notably, GSNOR is found in the endometrium (RPKM 69.1), kidney (RPKM 68.7), fat (RPKM 61.5), liver (RPKM 57.4), prostate (RPKM 62.0), ovary (RPKM 49.2), and esophagus (RPKM 53.3).[61] GSNOR is a cysteine rich homodimer, found in the nucleus and cytoplasm.[62] It is a metalloprotein, containing two zinc atoms per monomer, while both are in the catalytic domain, only one is involved in catalysis while the other is considered a structural zinc. The molecular weight of a monomer is 39,724 kDa consisting of 374 amino acids (UniProtKB identifier: P11766) translated from 9 exons.[58] The amino acids involved with binding are highly conserved, especially Glu68 and Arg379 since they are important to the catalytic mechanism.[58, 63] Cys45, His67, Glu68, and Cys174 are involved in the binding of the catalytic zinc atom while Cys97, Cys100, Cys103, and Cys111 bind the structural zinc.[64] Amino acids Ala302-Gln307 are involved in the diner interface interactions.[65] It is the amino acids of the interacting interface, and in the coenzyme binding domain, that protect the integrity of the homodimer; variations here prevent the formation of heterodimers with other alcohol dehydrogenase enzymes.[65-66] The dimeric structure and the dimeric interface of human GSNOR is shown in **Figure 2.2.1b**, while the amino acids involved in the binding of the zinc atoms are displayed in **Figure 2.2.1c**.

These amino acid labels are consistent with the Met1-Ile374 sequence for human GSNOR used for the recombinant wild type GSNOR sequenced for this project. The full sequence can be found in **Appendix Figure A.1**.

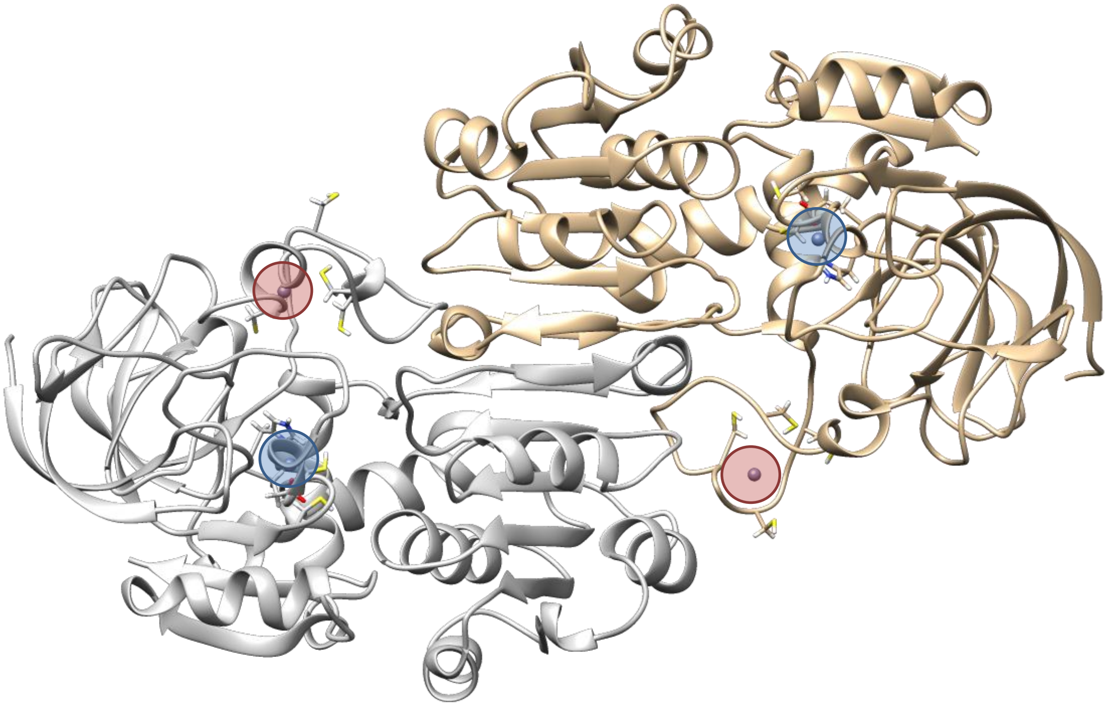

Figure 2.2.1b: GSNOR dimeric crystal structures. GSNOR crystal structure images (PDB ID: 3QJ5) modified using UCSF Chimera software. Dimerized wild type GSNOR crystal structure. Red circles highlight structural zinc atoms, blue circles highlight catalytic zinc atoms. The left-sided monomer is shaded grey to call attention to the dimer interface

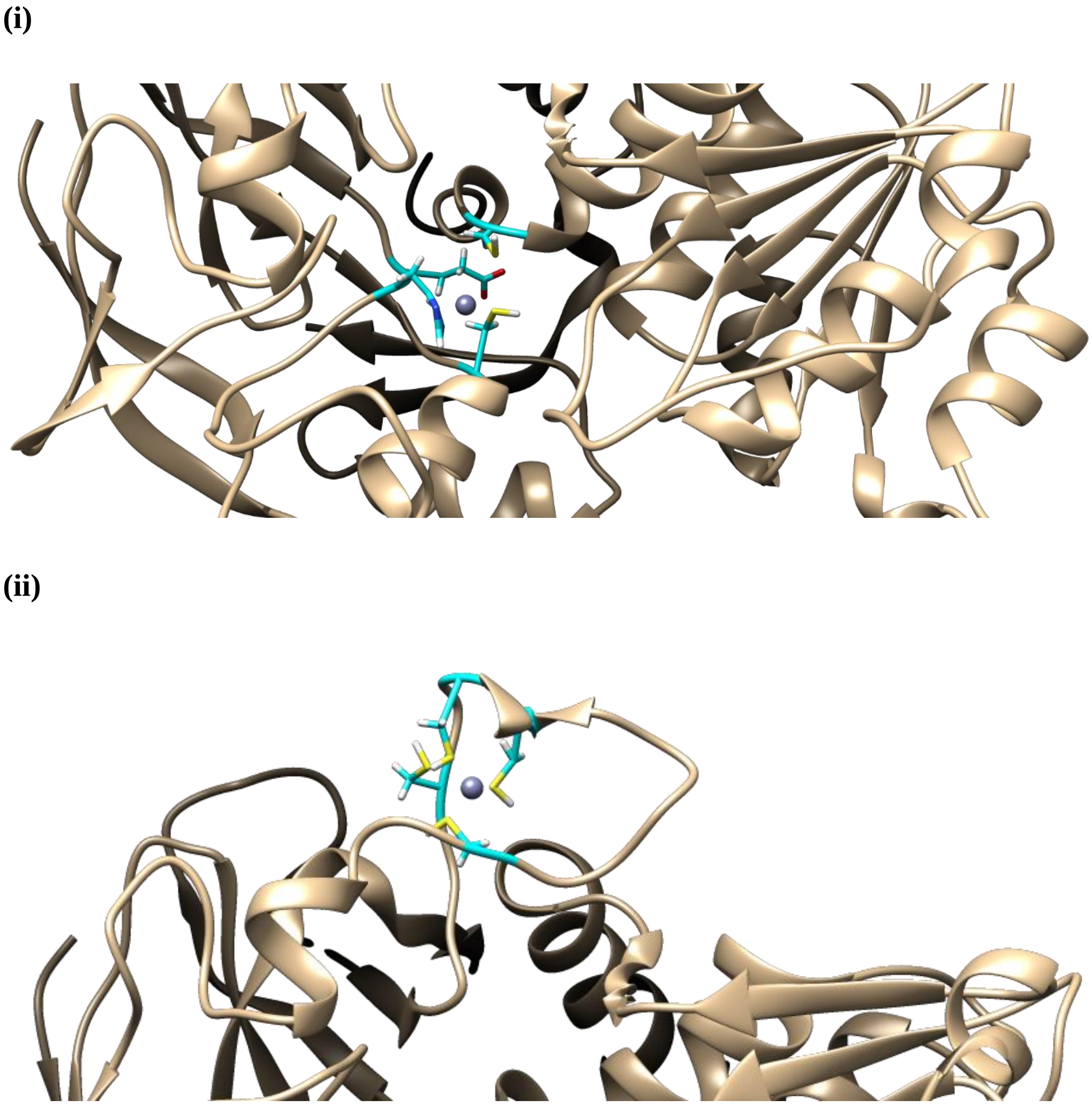

Figure 2.2.1c: Zinc binding of GSNOR.

(i) Active site pocket with catalytic zinc. Cys45, His67, Glu68, and Cys174 are highlighted. Image acquired from the left-sided monomer, relative to the structures displayed in **Figure 2.2.1b**.

(ii) Structural zinc with Cys97, Cys100, Cys103, and Cys111 highlighted. Image acquired from the left-sided monomer, relative to the structures displayed in **Figure 2.2.1b.**

2.2.2 GSNO & GSNOR in the Human Body

The two best substrates for ADH5 are HMGSH and GSNO. With the catalytic efficiency of the metabolism of GSNO almost twice of that for HMGSH, GSNO is considered the best substrate for the enzyme.[67]

The metabolism of GSNO begins with the reductase activity of GSNOR. The first step involves GSNOR reducing GSNO to the unstable intermediate N-hydroxy-sulphenamide (GSNHOH) (**Equation 2.2.2a**). When GSH is present, GSNHOH will react to form the glutathione dimer GSSG, with hydroxylamine (NH_2OH) as a side product (**Equation 2.2.2b**). Without GSH present, the unstable GSNHOH will spontaneously rearrange to form glutathione sulphinamide ($GSONH_2$) which can then be hydrolysed under acidic conditions to obtain glutathione sulphinic acid (GSOOH) and ammonia (NH_4^+) (**Equation 2.2.2c**).[68] The overall reaction is irreversible[67], and the structural changes described are shown in **Figure 2.2.2a**.

Equation 2.2.2a: $\boldsymbol{GSNO + NADH + H^+ \xrightarrow{GSNOR} GS - NHOH + NAD^+}$

Equation 2.2.2b: $\boldsymbol{GS - NHOH + GSH \longrightarrow GSSG + NH_2OH}$

Equation 2.2.2c: $\boldsymbol{GSONH_2 + H_2O \longrightarrow GSOOH + NH_4^+}$

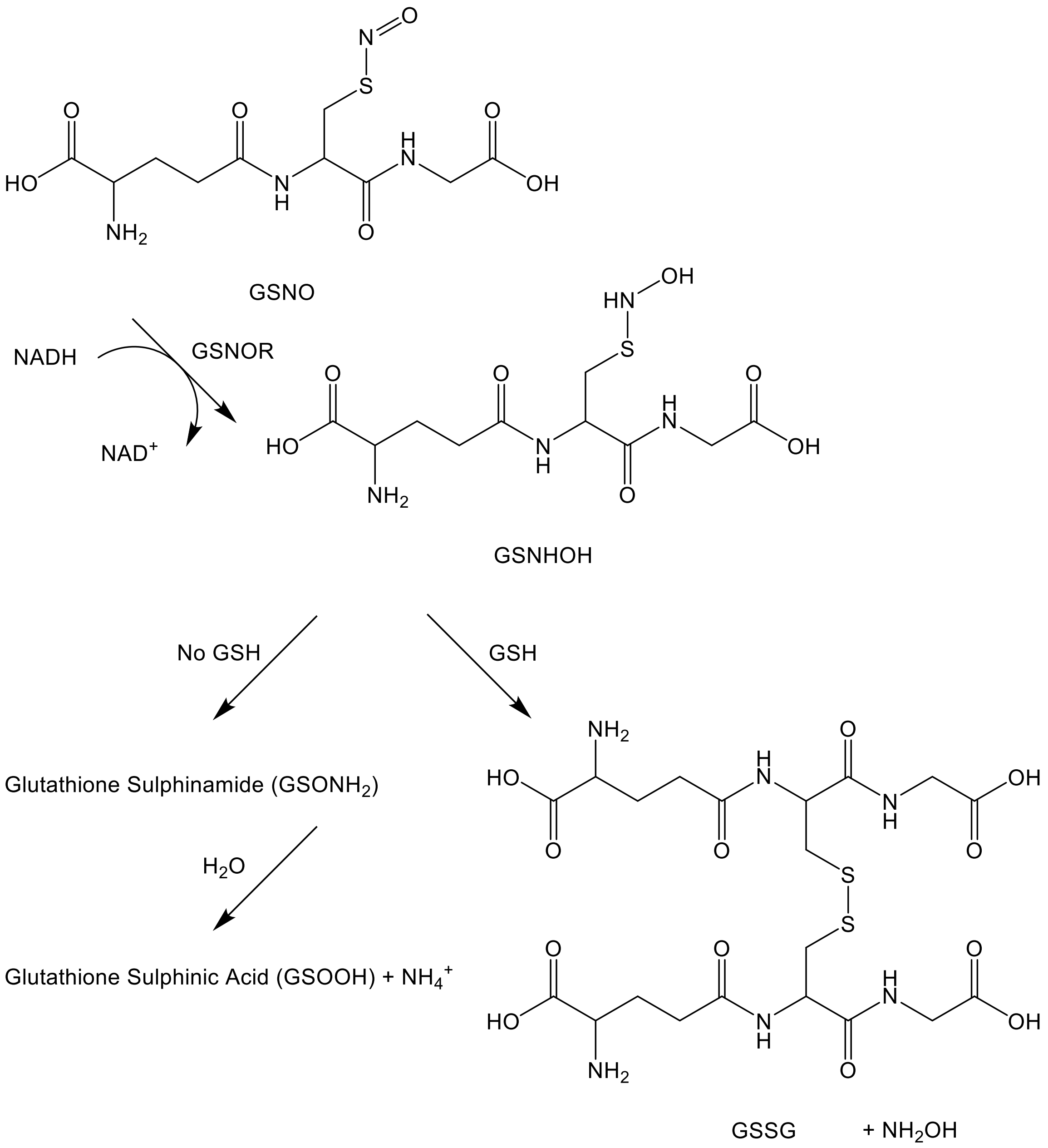

Figure 2.2.2a: Reaction products of GSNO metabolism. GSNO is reduced to GSNHOH by enzyme GSNOR and cofactor NADH. Unstable GSNHOH has two routes of action, with GSH present, GSSG will be formed. Without GSH, GSNHOH will rearrange to $GSONH_2$ which can hydrolyse under acidic conditions to GSOOH.

The GNSO products are determined on the cell redox potential related to the GSH levels. GSH levels can vary wildly due to its antioxidant activity, under oxidative stress GSH levels are decreased.[68] This results in $GSONH_2$ and subsequently GSOOH. Under physiological conditions, GSH occurring in the millimolar range can result in the formation of GSSG and NH_2OH.[39]

As previously stated, the regulation of GSNO correlates to cellular NO homeostasis, S-nitrosothiol formation, and the formation of reactive nitrogen species (RNS). This is due to GSNO acting as endogenous 'sink' or 'reservoir' of bioavailable NO. While NO production by NOS enzymes are co-localized with target proteins, the transfer of NO groups to on cysteine residues allows NO to propagate signal transduction pathways throughout the cell.[69] As GSNO is the most abundant small molecular weight SNO, its metabolism by GNSOR is of high consequence.

In particular, the inflammatory lung diseases of cystic fibrosis and asthma are both worsened by the upregulation in GSNOR activity. This, in turn, reduces the bioavailable NO in the form of reduced GSNO. Indeed, in GSNOR knockout mice display enhanced levels of SNO-proteins while attenuating experimental allergen-induced airway hyperreactivity (asthma) and myocardial infarction (heart attacks), at the cost of endotoxic shock being more severe.[69] GSNOR plays a role in regulating airway smooth muscle tone, as well as receptors in lungs and heart.[70] As well, they display increased angiogenesis, altered homeostasis of G protein–coupled receptors and decreased vascular resistance; due to the increase in SNO proteins.[69] Single-nucleotide polymorphism in GSNOR have been discovered to be are linked with the increase or decrease of childhood asthma, while adult asthma is due to an increase GSNOR of levels and activity in the fluid of the airway lining.[69] Beyond heart failure and asthma, GSNO has been linked to other diseases as well, including Crohn’s disease, IBS, autoimmune encephalomyelitis, autoimmune uveoretinitis, and more.[69]

2.2.3 Inhibitor’s of GSNOR

The regulatory processes GSNOR are currently under investigation, with inhibitors in particular being highly sought after. Due to dysregulation of GSNOR and GSNO depletion is associated with various disease conditions, being able to control activity of GSNOR *in vivo* is of interest.[71]

Perhaps the most prolific advancement in GSNOR medicine, is the development of Cavosonstat (N91115), a GSNOR inhibitor to aid cystic fibrosis patients with the ΔF508-CFTR mutation. This is a mutation within the gene for the cystic fibrosis transmembrane conductance regulator (CFTR), and is responsible for two thirds of cystic fibrosis cases world wide.[72] N91115 works to inhibit GSNOR so GSNO is available to promote CFTR maturation and plasma membrane stability.[73] With an increase in GSNOR activity and expression, there is less GSNO available to propagate protein-SNO signaling. Increasing the *in vivo* levels of S-nitrosothiol’s aids to modulate dilation of the airways, and the proteins that work to degrade CFTR.[73]

The increase in NO bioavailability by inhibiting GSNOR benefits other disease states as well. Vascular disorders in particular. N6022 is another inhibitor that made it to clinical studies. As a tight-binding, specific, and reversible N6022 is a potent inhibitor that has applications with asthma, chronic obstructive pulmonary disease, and IBS.[74] Another inhibitor, N6338, has been found to reduce blood pressure and vascular resistance in hypertensive rats.[75] There are other novel inhibitors[70, 74] that have been developed, however, N91115 and N6022 have had the most success.

Recent research has also found GSNOR to be influenced by S-nitrosylation. One 2016 study found that the nitrosation of conserved cysteines downregulated the enzyme.[65] A reactive oxygen species (ROS)-mediated inhibition of GSNOR has also be discovered.[76] Peroxide treatments led to oxidative modifications on the structural zinc, decreasing the rate of GSNO metabolism and contributing to the activation of anti-oxidative mechanisms.

2.2.4 Deviations & Classical Enzymatic Kinetics

The rates of reactions for enzymatic processes can be monitored and explained through various kinetic parameters over the course of a reaction. A general reaction scheme, **Equation 2.2.4a** describes a reversable joining of the enzyme (E) and the substrate (S), to form an enzyme-substrate complex (ES), along with the forward (k_1) and reverse rates (k_{-1}) of reaction. For the progress of the reaction to come to completion, the ES complex performs its function in order to release the reaction product (P); this corresponds to its own rate (k_2).[77]

Equation 2.2.4a:

$$\mathrm{E} + \mathrm{S} \underset{k_{-1}}{\overset{k_1}{\rightleftharpoons}} \mathrm{ES} \xrightarrow{k_2} \mathrm{E} + \mathrm{P}$$

The classical model to describe enzyme kinetics was described by and named after Leonor Michaelis and Maud Menten. The Michaelis-Menten model describes the rate equation for the process shown in **Equation 2.2.4a** as a function of substrate concentration. The rate equation, **Equation 2.2.4b**, demands several assumptions for the fit to be a perfect match for experimental data. This includes an assumption for instantaneous chemical equilibrium during the formation of ES ($k_{-1} >> k_2$), as well as the use of steady state conditions ([S] >> [E]).[77]

Equation 2.2.4b: $\boldsymbol{v_o = \frac{V_{max}[S]}{K_M + [S]} = \frac{k_{cat}[E]_T[S]}{K_M + [S]}}$

Upon first glance of the Michaelis-Menten equation (**Equation 2.2.4b**), three parameters present themselves, while others can be derived. The Michaelis constant (K_M) is derived from the combination of rates displayed in **Equation 2.2.4a**. This is shown in **Equation 2.2.4c**, operationally K_M corresponds to the concentration of substrate at half the maximal velocity (V_{max}). At the maximal velocity, [S] >> K_M and the reaction velocity equation can be represented by using k_2[E] instead of V_{max}, under these conditions, k_2 represents k_{cat}, the catalytic constant. This constant is then used to measure the catalytic efficiency, or turnover number, of the system (**Equation 2.2.4d**).[77-78] The catalytic constant is defined in **Equation 2.2.4e**.

Equation 2.2.4c: $\boldsymbol{K_M = \frac{k_{-1} + k_2}{k_1}}$

Equation 2.2.4d: $\boldsymbol{Catalytic\ Efficiency = \frac{k_{cat}}{K_M}}$

Equation 2.2.4e: $\boldsymbol{k_{cat} = \frac{V_{max}}{[E]}}$

Deviations from the Michaelis-Menten model require further consideration in order to accurately represent the enzymatic system. Such is the case for allosteric enzymes. The term allosteric describes enzymes that have integrations at a site other than the catalytic site that influences activity.[78] Allosteric modulators can include external ligands or the substrate itself and can offer a variety of effects. Binding of a modulator can affect the binding affinity of the substrate, affect the rates of the catalysis, or offer conformational changes.[78] When the binding at an allosteric site affects the binding to the active site, this is called a cooperative process, which can proceed in a positive or negative manner. These changes affect the steady-state kinetic trend, offering deviations from the Michaelis-Menten curve. While non-allosteric enzymes form a rectangular hyperbolic curve, cooperative binding results in sigmoidal curves depending on the degree of cooperativity.

A sigmoidal deviation in the O_2 binding curve of haemoglobin was first described by Archibald Hill.[77] The resulting Hill Equation (**Equation 2.2.4f**) can be used to provide a more accurate fit for cooperative steady state kinetic data. A couple of marked differences differentiates the Hill Equation from the Michaelis-Menten curve, including the inclusion of the Hill constant, *n*, and the renaming of K_M to $K_{0.5}$. The Hill constant, *n*, provides the degree of cooperativity, when n=1 there is noncooperative behaviour and the curve is identical to a Michaelis-Menten plot. With n<1 there is noncooperative allostery and n>1 corresponds to positive cooperativity with allosteric binding.

Equation 2.2.4f: $\boldsymbol{v_o = \frac{V_{max}[S]^n}{K_{0.5}^n + [S]^n}}$

Deviations from Michaelis-Menten resulting in positive cooperativity is shown in **Figure 2.2.4a**, while deviations resulting in various degrees of positive and negative cooperativity is shown in **Figure 2.2.4b**. With a positive modulator (n>1), binding of the modulator enhances further binding of the substrate, resulting in a large increase in reaction velocity after $K_{0.5}$, allowing the enzyme to reach V_{max} faster. At low substrate concentrations, below $K_{0.5}$, the enzyme is in a less active confirmation, resulting in lower reaction rates in comparison to a noncooperative enzyme adhering to similar parameters.

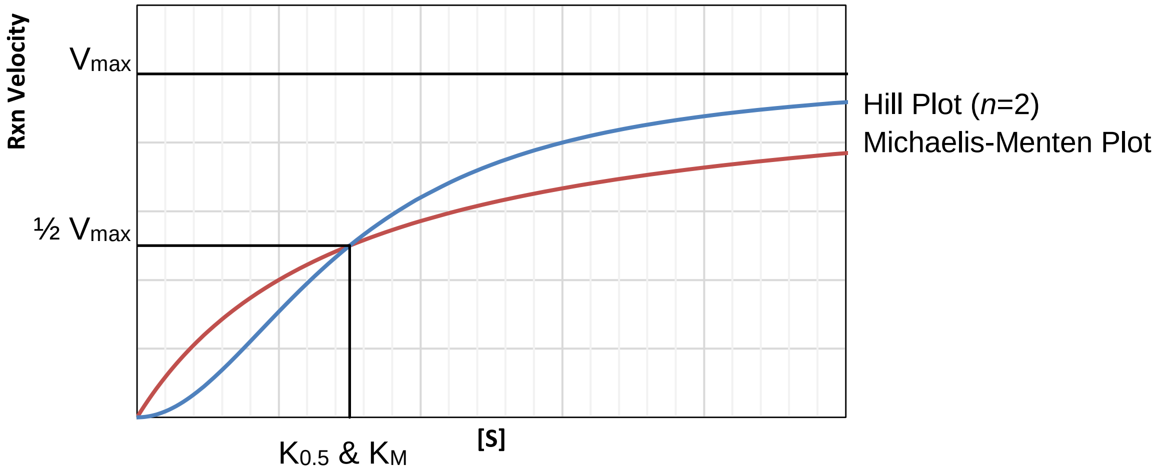

Figure 2.2.4a: Classical Michaelis-Menten curve in comparison to a Hill plot displaying positive cooperativity. Constructed with identical V_{max} and K_M=$K_{0.5}$. *n*=2 for the Hill plot, *n*=1 for the Michaelis-Menten curve.

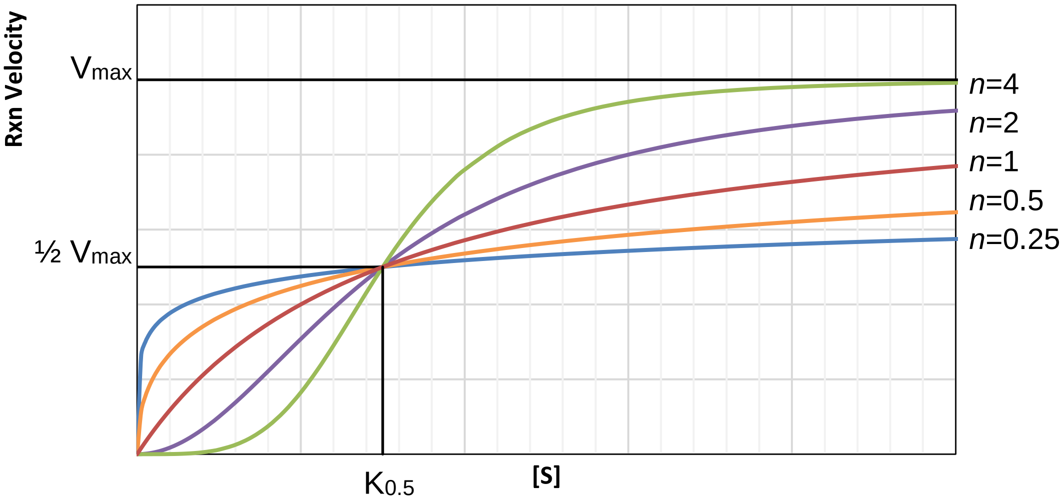

Figure 2.2.4b: Various sigmoidal Hill plots. Constructed using various hill coefficients (*n*), and identical V_{max} and $K_{0.5}$ values. Positive cooperativity is shown in the green (*n*=4) and purple (*n*=2) curves, noncooperatively in the red (*n*=1) curve and negative cooperativity in the yellow (*n*=0.5), and blue (*n*=0.25) curves.

2.2.5 Electrospray Ionisation Mass Spectrometry (ESI-MS)

Mass spectrometry (MS) allows for the analytical analysis of molecular ions. It is an invaluable tool to identify, characterize, and quantify biomolecules.[79] Electrospray ionization (ESI) was adapted for tandem use with mass spectrometry in the 1960s, but it was not until the mid 1980s when the technique was adapted for use with proteins and peptides.[80-82] Advancements in this field aided greatly in the advancements in proteomic studies.[79] The 2002 Nobel Prize in Chemistry was split by John Fenn, for his work on ESI-MS.

There are several steps involved in obtaining ionized analyte. The liquid sample, prepared in a volatile solvent, is fed through a metal capillary held at a high electric potential (2-6 kV). This current can be positive (+, protonation) or negative (-, deprotonation) depending on the ion mode of the mass spectrometer. In positive ion mode, the analyte will acquire net positive charges. With application of the current, these positively charged ions gather at the tip of the capillary, forming a sharp 'Taylor' cone.[83] When electrostatic repulsion becomes stronger than the surface tension, charged droplets leave the cone the direction of the counter-electrode.[84] During the flight, solvent evaporates the particles get smaller in size, leading to larger charge densities.[82] A flow of nebulizing gas ($N_{2(g)}$, as shown in **Figure 2.2.5a**) adds shear forces to the droplets, aiding in disintegration.[84-85] With this deformation and reduction in size, and the increase in electrostatic repulsion, the particle reaches its upper Rayleigh stability limit, resulting in a 'Rayleigh explosion' where the larger 'parent' particle surface turns into a protrusion wherein the particle gives off a jet of 'daughter' microdroplets.[84] This process continues until only bare ions remain. It is bare ions of interest that are completely sorted by their mass charge (*m/z*) ratios and detected by the spectrometer.

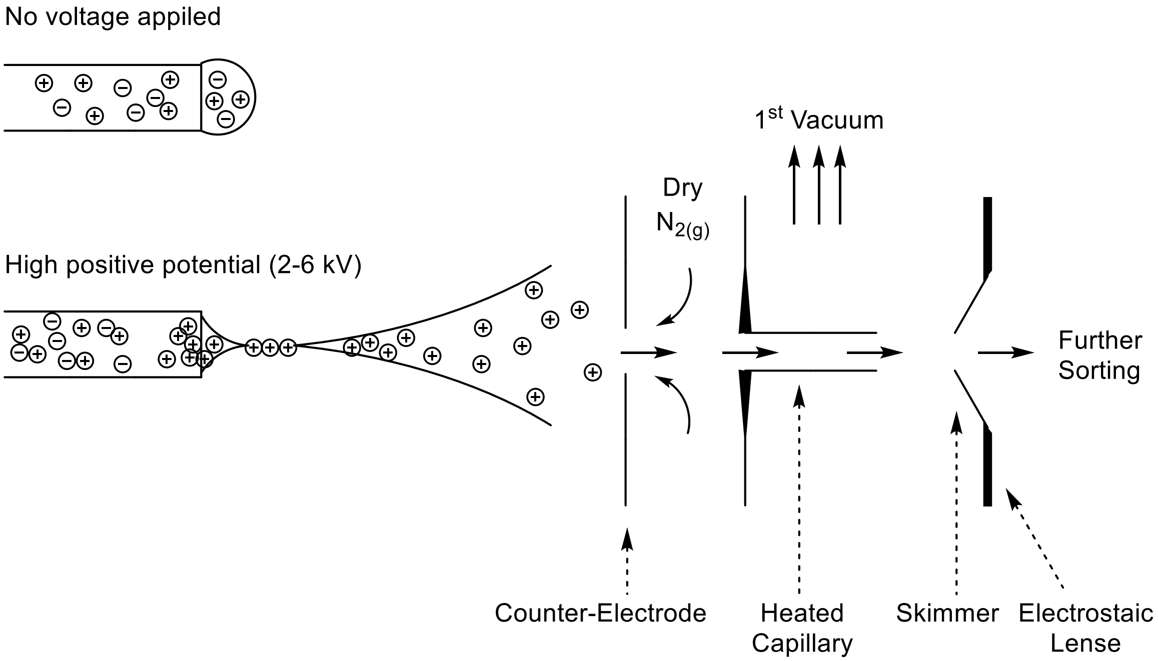

Figure 2.2.5a: Electrospray ionization of liquid analyte. With a high electric potential applied to the analyte capillary, the otherwise round meniscus forms a cone where charges collect (in this case, positive charges, for the application of a positive potential). Analyte is released as fine mist to enter the mass spectrometer. As charged droplets enter the counter-electrode, flowing through pressure and potential gradients aids in stripping ions of solvent and of each other, allowing only bare ions be detected.

2.2.6 Hydrogen Deuterium Exchange Mass Spectrometry (HDX-MS)

Hydrogen/deuterium exchange (HDX) mass spectrometry (MS) is a technique that has become key in investigating the structural dynamics of a protein structures. This is significant knowledge, to supplement the information that static structures obtained from crystal structures.[86] As well this technique can offer insights to protein-protein complexes, protein-ligand interaction, protein mutations, post-translational modifications, and monitor conformational changes due to functional changes.[87] The pharmaceutical industry, in particular, benefits from HDX-MS, in regards to protein-drug interactions.[87]

The exchange reaction occurs when a deuterium source is introduced to a protein solution. Labile protons will exchange with the solvent, including -OH, -NH, and -SH hydrogens.[86] However, since the hydrogens of amino acid side chains can exchange on a sub-millisecond time scale, most studies are concerned with the slower exchange that can be monitored on peptide backbone amides.[86, 88] Of the backbone amides, exchange is faster on fully solvent exposed amides that are not involved in hydrogen bonding.

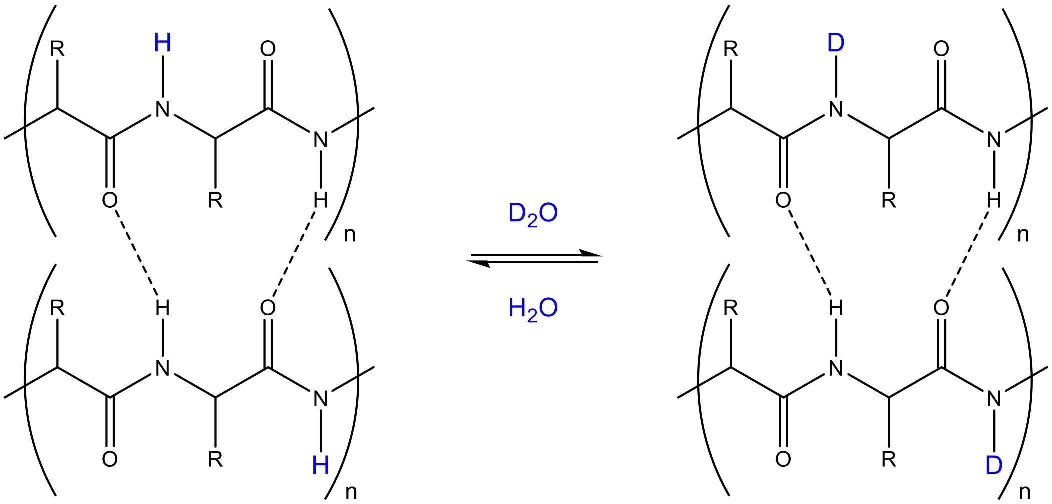

Figure 2.2.6a: Hydrogen/deuterium exchange (HDX) with parallel β-sheets. Solvent exposed, non-hydrogen bonding amide hydrogens will readily exchange with introduced deuterium. Atoms involved in the change are showed in blue.

The exchange rate of any given amide is dependent on the rate constant of the chemical exchange (k_{ch}), combined with the rates of open (k_{op}) and closed (k_{cl}) confirmation transitions of the amide.[86] k_{ch} is influenced by the flanking side changes, reaction temperature, and deuterium ion concentration (pD). The mechanism detailing the opening of a closed amide, the deuterium exchange, and the return to a closed confirmation is shown in **Equation 2.2.6a**.[86] The rate of overall exchange (k_{HDX}) can then be described as a combination of these rates, with three possibilities: (1) If the rate of H to D change (k_{ch}) is much greater than the rate of the amide closing (k_{cl}), ($k_{ch} >> k_{cl}$), then **Equation 2.2.6b** is the simplified rate equation. This implies that exchange occurs during the first opening event.[86] (2) If the rate of closure (k_{cl}) is much greater than the rate of the exchange (k_{ch}), ($k_{ch} << k_{cl}$), then **Equation 2.2.6c** is the simplified rate equation. This situation is more common under physiological conditions. (3) If the amide is permanently unprotected, **Equation 2.2.6d** is the simplified rate equation.[86]

Equation 2.2.6a:

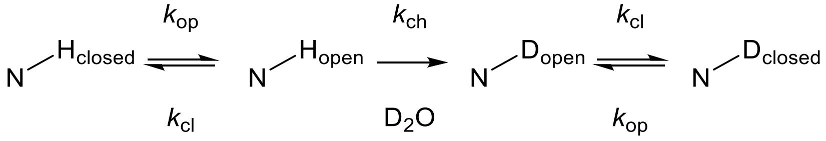

Equation 2.2.6b: $\boldsymbol{k_{HDX} = k_{op}}$

Equation 2.2.6c: $\boldsymbol{k_{HDX} = \frac{k_{op}}{k_{cl}} k_{ch}}$

Equation 2.2.6d: $\boldsymbol{k_{HDX} \approx k_{ch}}$

The exchange reaction can be acid, base, or water catalyzed, with the acid catalyzed mechanism predomination at pH's below 2. At pH levels between 2.0-3.0, water catalysis is dominant, with acid and base mechanisms contributing equally.[89] It is here where the exchange rate (k_{ch}) is at its lowest, with values 10,000-fold lower at pH 2.5, compared to pH 7.0.[89-90]

HDX-MS experiments are capable of investigating protein-substrate interactions. One method of doing so includes utilizing microfluidic set ups in order to perform consistent and reproducible experiments. An example of this is the time-resolved electrospray (TRESI) microfluidics set up developed by Wilson and Konermann.[91] In a quench-flow experiment, the exchange reaction is initiated by the rapid mixing of reagent, and concluded by mixing with a quenching reagent. The TRESI device contains a series of capillaries with an adjustable reaction volume that allows for static time-points and kinetic measurements. The basis of the set up includes a larger metal capillary with a smaller glass capillary inside. When the ends of the two are flush, the reaction volume is zero. When the glass capillary is pulled deeper into the metal capillary, the reagents being pumped through the two capillaries are allowed to mix. Protein solution flowing through the glass capillary is mixed with deuterium oxide flowing around the glass, contained by the metal capillary. The mixing volume, adjustable by the movement of the glass capillary, ends at a T-junction, in which the solution is mixed with an opposite flow of quenching solution (acid). The quenched reaction exits out the perpendicular channel, towards the ionization source (ESI).

In this study, the enzyme S-nitrosoglutathione reductase (GSNOR) is characterized computational studies, kinetic studies, and hydrogen deuterium exchange mass spectrometry. These studies may support the existence of a possible allosteric site on the enzyme. Further information on the HDX experiments performed here, as well as the use and set up of the TRESI device is elaborated on in the Methods section of this chapter, in **Section 2.3.8**, and **Figure 2.3.8a** in particular.

2.3 Methods

2.3.1 GSNOR WT Cloning, Mutagenesis, and Protein Isolation

The original cloning and mutagenesis of the human ADH5 gene was performed by Dr. Bei Sun. The final result was recombinant GSNOR containing two 6X-histidine tags, one at each terminus, to aid in purification. The pET28b_ADH5 plasmid was then transformed into BL21(DE3) *E. coli* for further work. Further detail on Dr. Sun's work in this regard can be found in **Appendix A**.

To begin protein isolation, a single pET28b_ADH5 in BL21 cellular colony was picked from LB-kanamycin agar plates and grown in a sterile round bottom polypropylene culture tube containing 4 mL of 2X YT media and 50 μg/mL kanamycin (YT kan); this was left to incubate overnight at 37ºC with shaking. This colony of cells was added to a starter culture flask at a rate of 1 mL of colony per 100 mL of YT kan media; this was grown for 8 hours at 37ºC with shaking. This starter culture was used to inoculate 1 L of YT kan media in a 4 L flask, at the same rate of 1 mL per 100 mL of media. This was then left to grow overnight, shaking at room temperature. The next morning, GSNOR expression was induced by the addition of IPTG to a final concentration of 0.4 mM. This induced culture was left to incubate for 24 hours, shaking, at room temperature. The cells were then harvested by centrifugation, the cells and their media were placed in 500 mL Nalgene centrifuge bottles and centrifuged at 6,000 rpm for 30 minutes at 4ºC. The supernatant was subsequently discarded and the bacterial cell pellet was resuspended in pH 8 lysis buffer (50 mM Tris-HCl, 150 mM NaCl, 1 mM PMSF, 1% Triton X-100, 75 μg/mL

DNase I and 100 µg/mL lysozyme). The crude lysate was incubated on ice for 30 minutes and further lysed by pulse sonication. This was done on ice, with 30 seconds on, 30 seconds off, for a total of 8 pulses. The lysate was then centrifuged in 50 mL Nalgene centrifuge bottles at 12,000 rpm for 30 minutes at 4ºC. Further purification of the supernatant was done using HIS-Select Nickle Affinity Gel (Sigma-Aldrich P6611).

The Ni affinity column, stored in 20% (v/v) ethanol, was equilibrated with wash buffer (50 mM Tris-HCl, 150 mM NaCl, pH 8) and placed in a 50 mL conical tube. The lysate supernatant was added to the column matrix and allowed to mix for 1 hour at 4ºC. The lysate and matrix were returned to the glass chromatography column (Rio-Rad Econo-Column). The column matrix was washed with wash buffer, followed by 10 mM imidazole wash buffer, and then 25 mM imidazole wash buffer before elution. Bound GSNOR was then eluted with elution buffer (300 mM imidazole, 50 mM Tris-HCl, 150 mM NaCl, pH 8). The eluted protein was then buffer exchanged into storage solution (58 mM Na_2HPO_4, 17 mM NaH_2PO_4, 68 mM NaCl, 15% glycerol, pH 7.4) using 15 mL capacity Amicon centrifugal filter tubes (Millipore Sigma UFC903008) and stored at -80°C.

2.3.2 GSNO Synthesis

The majority of the GSNO used for this project was synthesized by Leslie Ventimiglia and Mark Potter.

GSNO was synthesized in-house as per previously determined protocols.[92] Glutathione (GSH) was mixed in a 1:1 stoichiometric ratio of sodium nitrite ($NaNO_2$) at 4ºC in 0.5M HCl. After 40 minutes, acetone was added in 1:1 (v/v) and mixed for 10 minutes until the red GSNO precipitated out of solution. The precipitate was subsequently filtered and washed 3x with cold water, 3x acetone, and 3x ether. The GSNO was then lyophilized and stored at -20ºC. The concentration of any GSNO solution prepared out of the lyophilized powder was confirmed by UV-Vis spectroscopy; as outlined in **Section 2.3.3**.

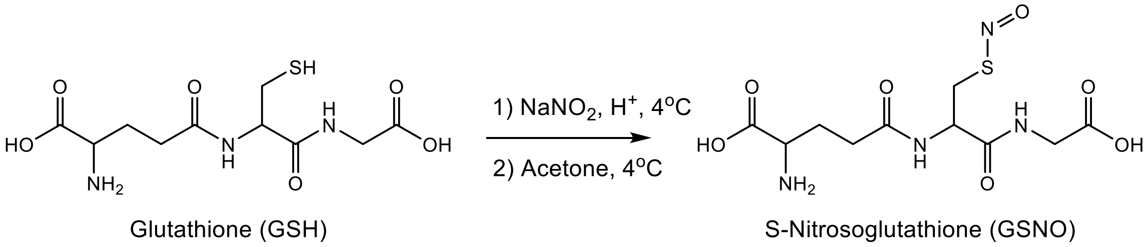

Figure 2.3.2a: Synthesis of GSNO.

2.3.3 GSNOR WT Kinetics & Kinetic Parameters

Steady state kinetic assays were performed using GSNO as a variable substrate, and keeping cofactor NADH constant. 20 mM NADH stock solution was prepared with Milli-Q (Advantage A10 Water Purification System, Millipore Sigma). GSNO stock solutions were prepared fresh from lyophilized powder and pH 7.4 PBS into 10 mM and 1 mM stock solutions. The true concentration of GSNO was obtained by measuring the absorbance of the 1 mM solution at 335 nm, utilizing the molar extinction coefficient of 922 M^{-1} cm^{-1}, and Beer's Law.[93]

GSNO, of increasing concentrations was added to a 500 μL cuvette containing 80 μM NADH and pH 7.4 PBS to a final volume of 500 μL. The kinetic reaction was initiated by the addition of 2 μg of GSNOR. The concentration of stock GSNO was confirmed by

Bradford Assay immediately prior to the experiment. The uptake of NADH during the reaction was monitored by its decrease in absorbance at 340 nm, 60 seconds of reaction was monitored by the Agilent 8453 UV/Vis spectrophotometer. The rate of the initial linear decrease corresponding to NADH uptake was plotted in correlation to the concentration of GSNO. From this, $K_{0.5}$ and V_{max} were calculated. Catalytic efficiency and k_{cat} were determined utilizing **Equations 2.2.4d-e**, respectively.

The experimental kinetic data was manipulated and plotted as per **Equation 2.3.3a-b** to determine the Hill constant. The constant, *n*, was found as the slope of the resulting line of best fit. This is due to the fact that the manipulation performed results in a graph displaying **Equation 2.3.3c**, where K represents binding constants of the ligand.

Equation 2.3.3a: $\boldsymbol{x - values = \log(X) = \log([GSNO])}$

Equation 2.3.3b: $\boldsymbol{y - values = \log\left(\frac{Y}{1-Y}\right) = \log\left(\frac{\frac{y}{V_{max}}}{1-\frac{y}{V_{max}}}\right)}$

Equation 2.3.3c: $\boldsymbol{log\left(\frac{Y}{1-Y}\right) = n\log(X) + \log(K)}$

2.3.4 Mass Spectrometry (MS)

All mass spectrometry was performed at York University in Toronto, Ontario in collaboration with Dr. Derek J. Wilson and his Lab Manager Cristina Lento. All experiments were performed by the author on a Waters Synapt G1 High Definition Mass Spectrometer (Synapt G1) with an electrospray ionization (ESI-MS), schematic shown in Figure **2.3.4a**. The Synapt G1 utilizes Waters' Triwave™ technology to allow for ion mobility separation (IMS); adding the separation based on mass and size to a given data set. With the IMS function turned on, unresolved, overlapping, peaks can be separated and analyzed. Analyte enters the mass spectrometer through electrospray ionization (ESI). Ion obtain a net positive charge through the application of a positive potential electric field. The formation of charged droplets results in solvent evaporation and gas-phase ions of interest. Electrostatic attraction and a vacuum allow the ions to enter into the spectrometer.

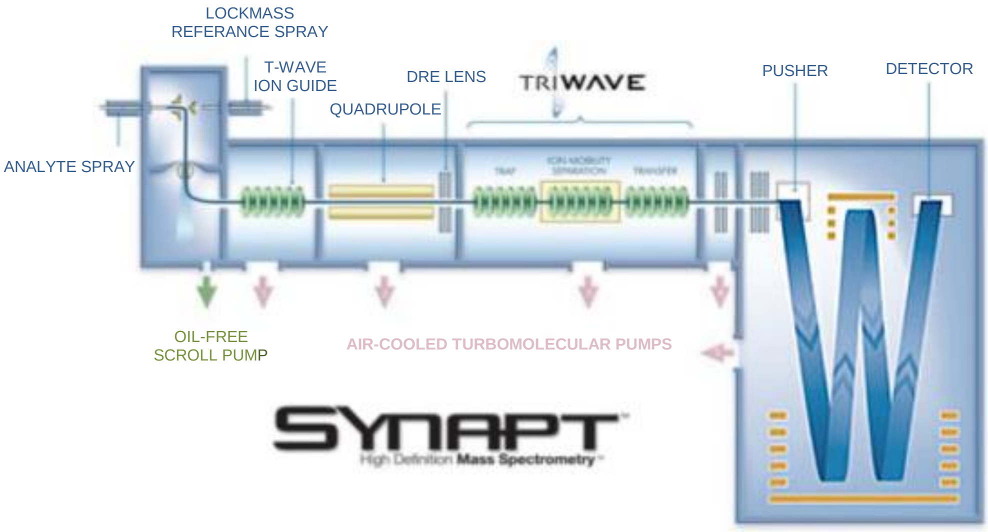

Figure 2.3.4a: Waters Synapt G1 Definition Mass Spectrometer schematic. Analyte is ionized from an electrospray source and incoming ions are focused by the T-wave ion guide mass ion selection by the quadrupole. The Triwave™ technology works with three 'waves' that perform three distinct functions: the first wave traps and releases ions, the second separates ions by their ion mobility and the final wave transfers ions to the time of flight (TOF) mass analyzer. Further fragmentation by collision induced dissociation (CID) can be performed before or after ion mobility separation.

2.3.5 GSNOR WT Native MS

Purified recombinant GSNOR was dethawed and storage buffer was buffer exchanged with 200 mM ammonium acetate, using a 15 mL compacity Amicon centrifugal filter tube. Protein was injected into the Synapt G1 mass spectrometer at a rate of 6 μL/min and data was recorded in positive ion mode at a range of 500-8000 *m/z*. Other system settings are overviewed in **Table 2.3.5**. The electrospray voltage settings are consistent for all MS data sets.

Table 2.3.5: Native GSNOR Synapt G1 Operating Settings.

Electrospray Ion Source Voltage Settings

Capillary Voltage	3.00 kV
Sampling Cone	50 V
Extraction Cone	2.0 V

Operating Pressures (Torr)

Trap	1.06×10^{-2}
IMS Cell	5.22×10^{-4}
TOF	7.63×10^{-7}
Backing Pressure	2.22

2.3.6 GSNOR WT Peptide Fragmentation

MS^1 fragmentation of native GSNOR WT is done using pepsin agarose beads placed in a fabricated poly(methyl methacrylate) (PMMA) chip that allows for low-pressure proteolysis with on-chip ESI. Fabricated as previously described by Wilson and colleagues.[94] The PMMA chip is shown in **Figure 2.3.6a (i)** while the assembled microfluidics apparatus is shown in **Figure 2.3.6a (ii)**; this set up includes the blue-coloured pepsin agarose beads, the entrance connector carrying native protein, ready for proteolysis, and an exit channel, towards ionization by electrospray and analysis by the Synapt G1 MS. The stock aliquots of pepsin agarose beads used are maintained by the Wilson Lab.

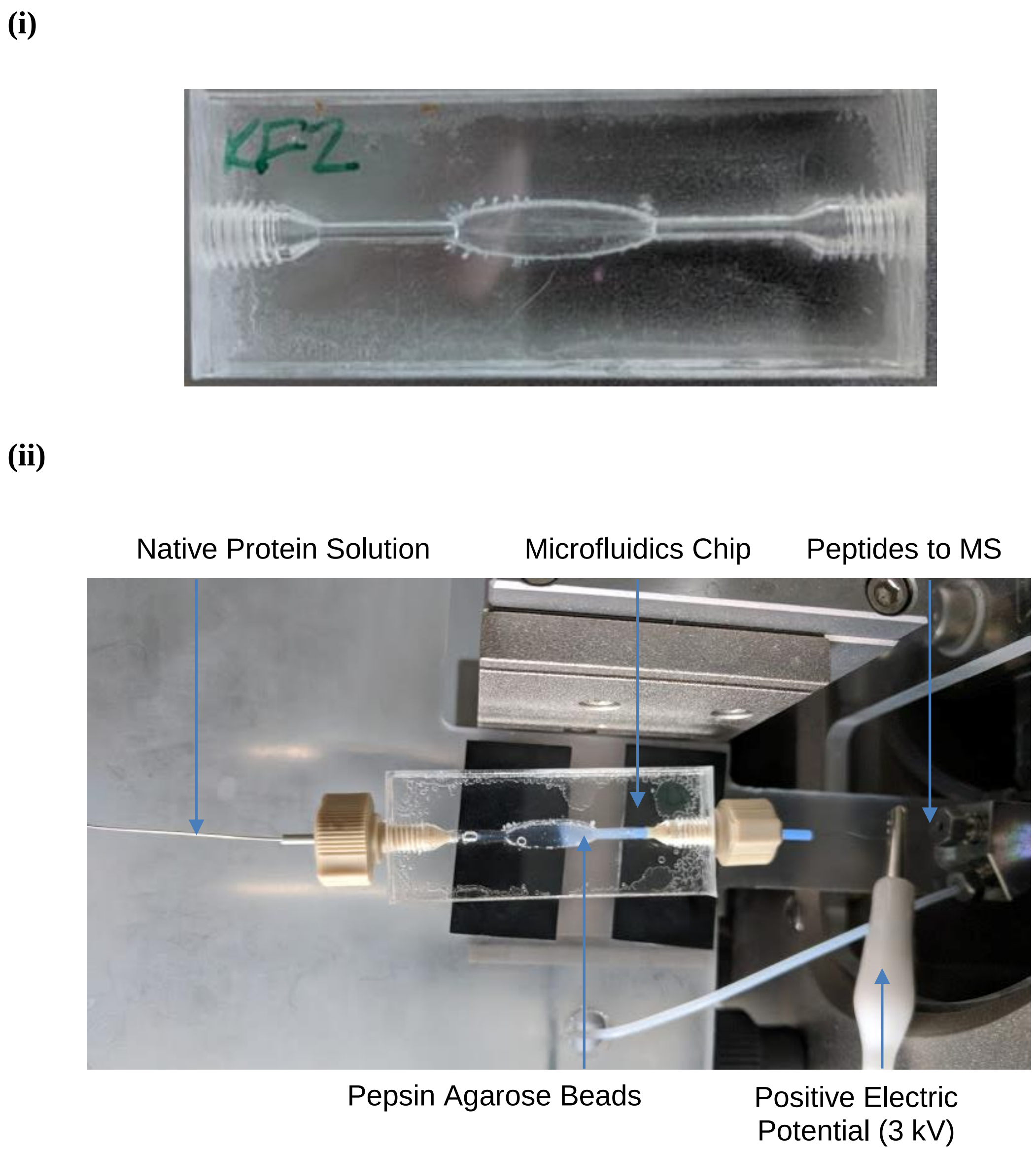

Figure 2.3.6a: PMMA chip for protein proteolysis.

(i) PMMA chip, with entrance channel and an exit channel, connected by the proteolysis reaction chamber.

(ii) Native protein solution is pumped into the PMMA microfluidics chip containing pepsin agarose beads for low-pressure proteolysis. The peptides then exit the pepsin resin for ESI to enter the Synapt G1 spectrometer.

2.3.7 GSNOR WT MS-MS for Peptide Identification

Tandem mass spectrometry (MS-MS, or MS^2) is utilized for characterization of the peptides fragmented from the pepsin column. By acquiring data in MS-TOF mode, a precursor ion can be chosen to undergo further fragmentation by CID. The collision energy applied was customized for each precursor ion to obtain an ideal fragmentation pattern. The fingerprint spectra were collected within a mass range of 100-2000 *m/z*.

A theoretical pepsin digest was performed using FindPept tool on the ExPASy Proteomics server (Swiss Institute of Bioinformatics, Basel). Search parameters were set to pepsin (porcine A) at $pH > 2$ with a mass tolerance of ± 0.5 Da. The possible identities of the parent ion were chosen from the resulting list. Each possible parent ion was theoretically fragmented by the spectra viewing software mMass and compared with the fingerprint. The parameters used included searching for the loss of $-H_2O$ and $-NH_3$, as well as identifying y, a, b, int-a, and int-b fragment ions.

2.3.8 GSNOR WT HDX-MS

Hydrogen deuterium exchange (HDX) MS was made possible by outfitting the Synapt G1 with the custom TRESI apparatus as described by Wilson *et al*.[91] The reagents utilized include 5% (v/v) acetic acid, GSNOR in 200 mM ammonium acetate, and deuterium oxide (D_2O) (99.9% purity of LC-MS grade, Sigma-Aldrich). These reagents are pumped through polyamide-coated glass capillary with an outer diameter (o.d.) of 109.2 μm using Harvard Apparatus Pump 11 Elite infusion syringe pumps (Holliston, MA). Protein and D_2O were pumped at a rate of 2 μL/min with 0.5 mL syringes (Hamilton 700

Series Gastight Syringe) while acid was pumped at a rate of 16 µL/min with a 5 mL or 2.5 mL syringe (Hamilton 1000 Series Gastight Syringe).

The TRESI microfluidics apparatus describes where the mixing of protein and D_2O takes place. The 109.2 µm o.d. glass capillary containing protein is encased in a metal capillary with an inner diameter (i.d.) of 132.6 µm. A 2 mm notch was made and the end of the glass capillary was sealed, this allowed for efficient kinetic mixing before the exchange reaction was quenched by the acid and sent to the PMMA chip containing the pepsin agarose beads for MS^1 fragmentation. The creation of the notch and the melting the end of the glass capillary was done fresh for each experiment using a *Versa*Laser™ as described.[91] Measuring different time points of D_2O incorporation is done by measuring the distance allowed from the end of the 'plug' (**Figure 2.3.8a (i)**) to the end of the outer capillary. The schematic of this device and its physical manifestation is shown in **Figure 2.3.8a**.

The HDX-MS experiments conducted for this report utilized 5 mm and 10 mm reaction spaces, which corresponds to 2.07 seconds (~2 secs) and 3.93 seconds (~4 secs), respectively. Data was collected in IMS mode in the 400-1500 *m/z* range. The operational settings and average operational pressures for these experiments are summarized in **Table 2.3.8**. The experimental deuterium uptake of each peptide obtained was calculated using a custom-built software program (DJW, unpublished results).

Each set of data was collected on the same day, including three 5 min spectra acquisitions of: protein GSNOR without deuterium exchange, two secs exchange, and four secs exchange. Followed by three 5 min spectra acquisitions of: protein GSNOR + 20x excess of GSNO without deuterium exchange, two secs exchange, and four secs exchange. Concentrations of GSNOR and GSNO were calculated by Bradford assay and UV-Vis, respectively, to confirm a 20x stoichiometric addition of GSNO. Integrity of the notch was confirmed to be maintained at the end of the experiment.

(i)

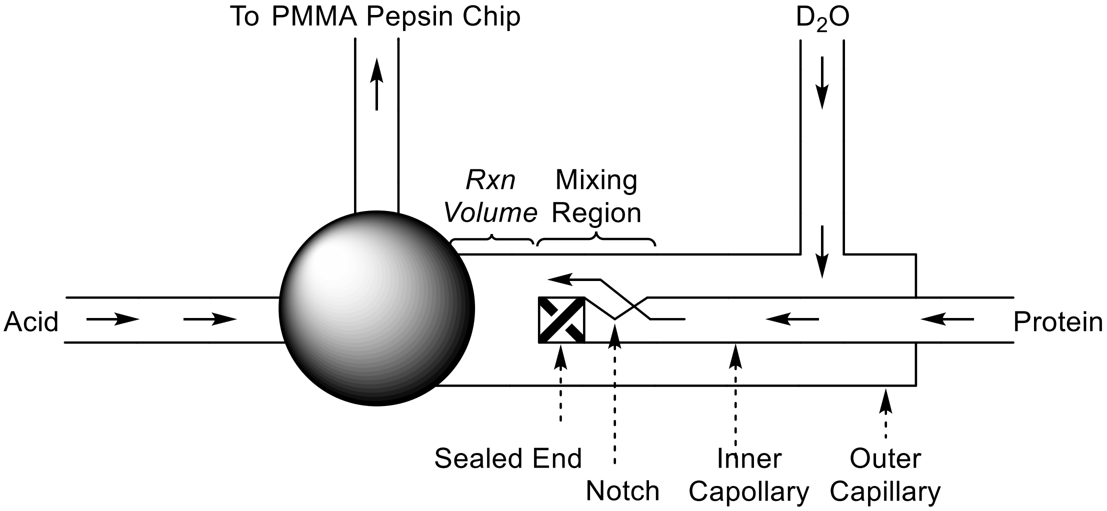

(ii)

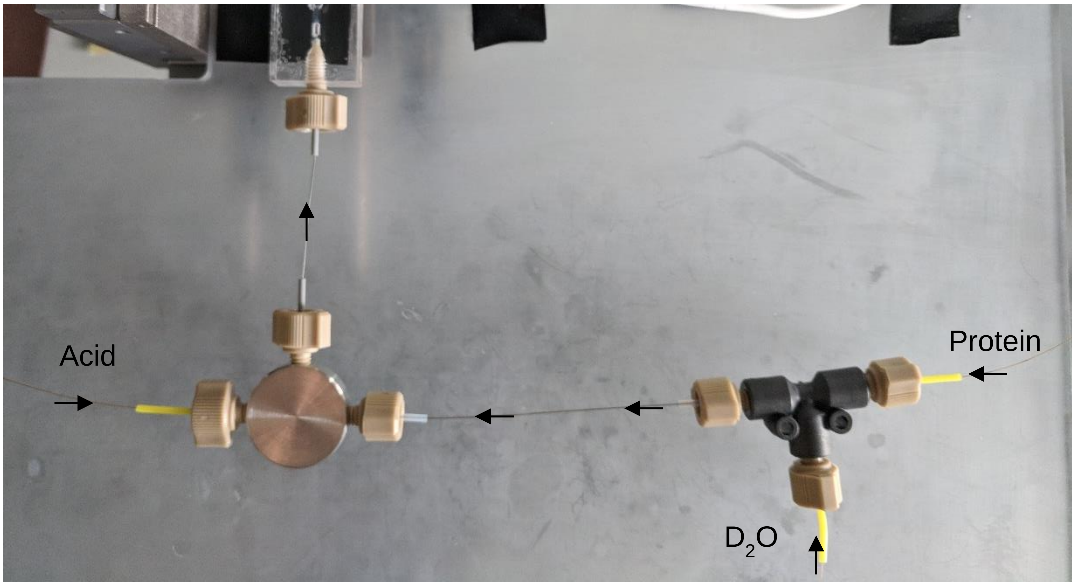

Figure 2.3.8a: TRESI microfluidics set up for HDX-MS.

(i) Schematic for D_2O and protein mixing, followed by acid quenching and fragmentation by pepsin. Protein solution exits the notch and immediately mixes with D_2O, the space from the end of the glass inner capillary to the end of the metal outer capillary corresponds to the exchange reaction time.

(ii) Complete set up of the TRESI device connected to the PMMA chip.

Table 2.3.8: HDX-MS GSNOR Synapt G1 Operating Settings.

Electrospray Ion Source Voltage Settings	
Capillary Voltage	3.00 kV
Sampling Cone	50 V
Extraction Cone	1.5 V
Operating Pressures (Torr)	
Trap	$2.19 \pm 0.15 \times 10^{-2}$
IMS Cell	$5.66 \pm 0.37 \times 10^{-1}$
TOF	$7.99 \pm 0.22 \times 10^{-7}$
Backing Pressure	2.17 ± 0.05

2.4 Results

Sigmoidal deviations resulting in positive cooperativity were identified with GSNOR kinetics. To further investigate the allosteric effect, molecular docking (MD) simulations were performed to look for a possible allosteric binding site for substrate GSNO. Electrospray mass spectrometry (ESI-MS) was also utilized it identify protein-ligand interactions. The MS experiments performed here include: native MS for dimer identification, MS-MS for peptide identification, and hydrogen–deuterium exchange experiments (HDX-MS) for the investigation of direct ligand interactions.

2.4.1 GSNOR WT Kinetics

Steady state kinetic assays of recombinant wild type GSNOR were performed in triplicate, with one set of representative data being displayed throughout this section. Upon assessment of the kinetic parameters of GSNOR, the apparent K_M, or $K_{0.5}$, was 16.7 ± 0.53 μM towards GSNO with a k_{cat} of 120000 ± 40000 s^{-1}. The catalytic efficiency, calculated as $k_{cat}/K_{0.5}$, was found to be 12000 ± 2000 s^{-1} M^{-1}. These values, as well as the Hill constant (n), are summarized in **Table 2.4.1.**

To determine possible allostery, the Hill coefficient was deduced to quantitatively determine the cooperativity of ligand binding. The kinetic data for reactions containing 0-70 μM GSNO were used to construct a Hill plot, as shown in **Figure 2.4.1a**. The resulting Hill constant observed was 1.49 ± 0.037.

With the Hill constant calculated, fit curves can be applied to the experimental data, as in **Figure 2.4.1b (i-ii)**. The featured data is shown with the classical Michaelis-Menten curve (*n* = 1) as well as the corresponding Hill plot (*n* = 1.54). **Figure 2.4.1b (ii)** offers a closer look at the lower concentrations.

Table 2.4.1: GSNOR WT Kinetic Parameters.

Kinetic Parameter	Value
$K_{0.5}$ (μM) (n=3)	16.7 ± 0.53
k_{cat} ($x10^5$ s^{-1}) (n=3)	1.2 ± 0.4
$k_{cat}/K_{0.5}$ ($x10^4$ s^{-1} M^{-1}) (n=3)	1.2 ± 0.2
n (n=3)	1.49 ± 0.037

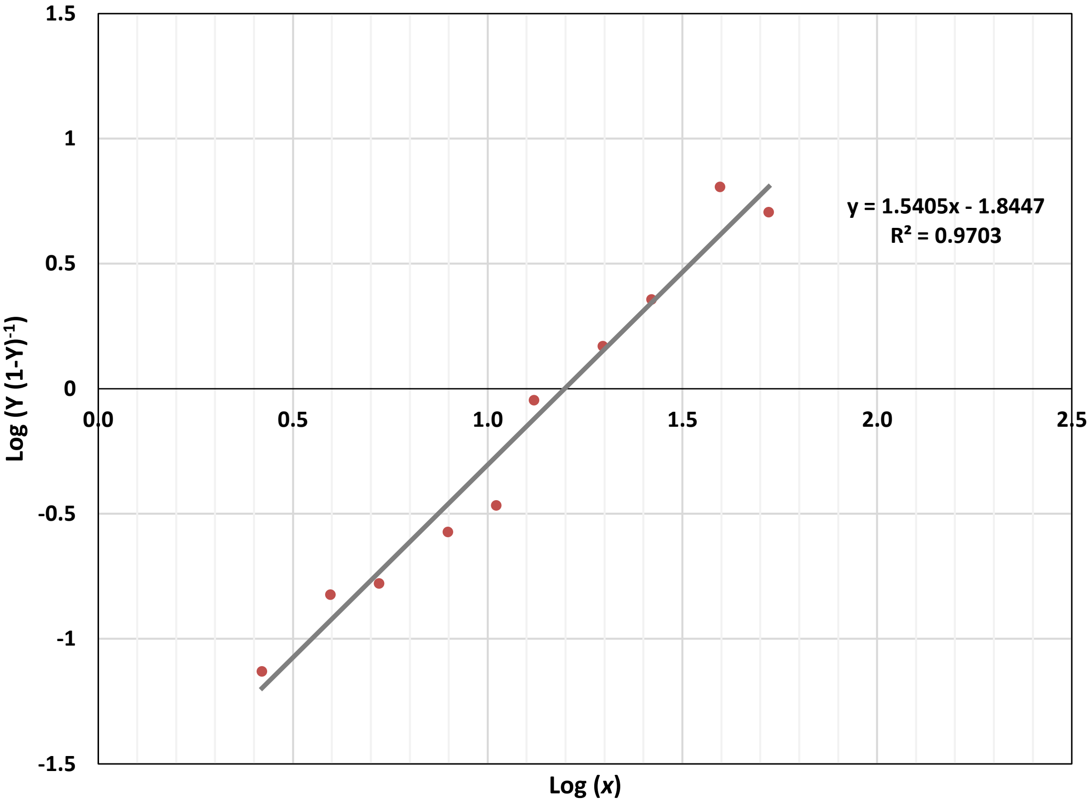

Figure 2.4.1a: Hill plot for the discovery of the Hill constant (*n*). Utilizing representative data of 0-60 μM GSNO, the Hill constant is determined by the slope of the line of best fit, $n = 1.54$.

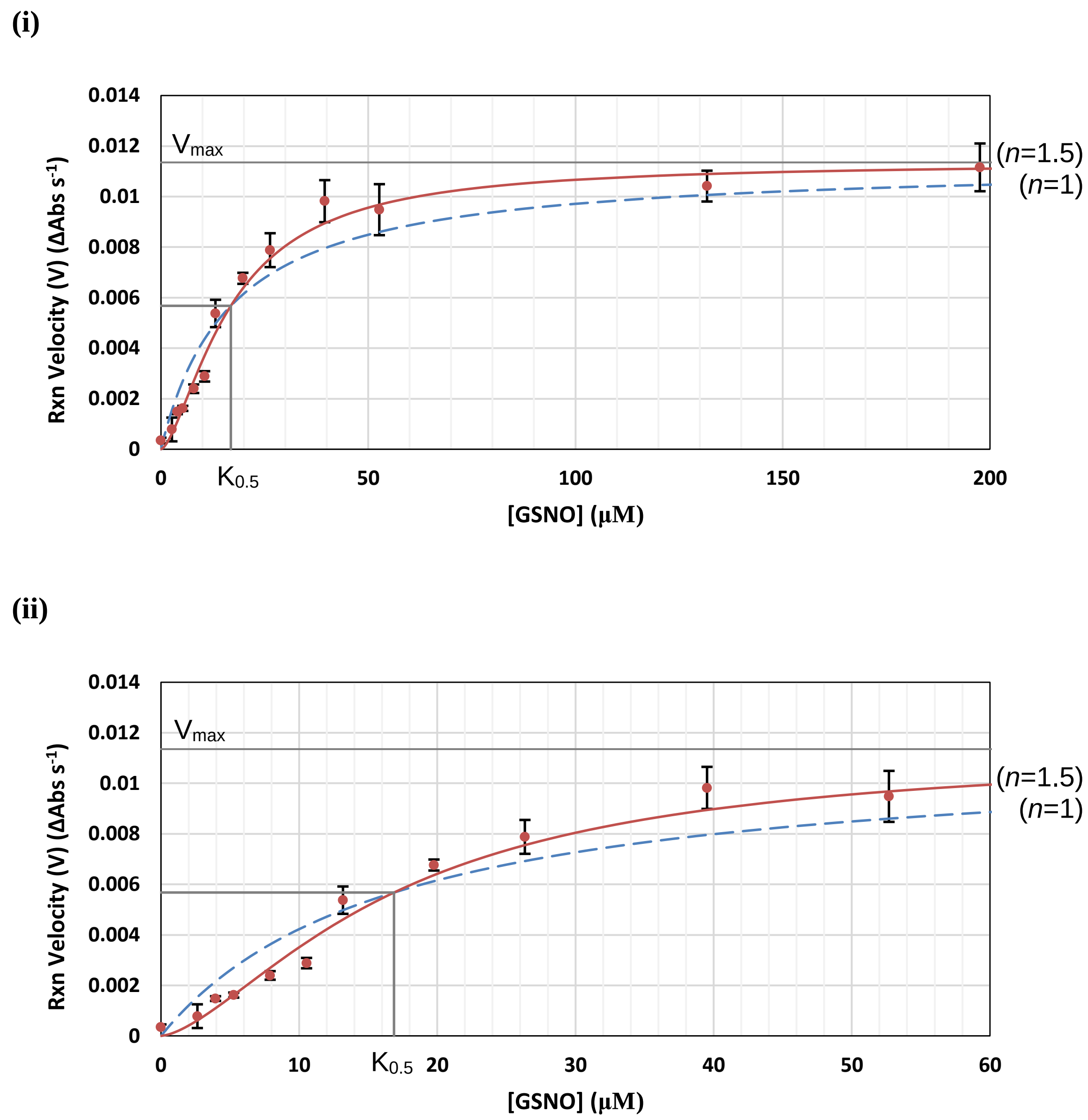

Figure 2.4.1b: Representative GSNOR WT kinetic data. Initial reaction rates measured by monitoring the decrease in absorbance at 340 nm. Each reaction contained 80 µM of NADH and was initiated by the addition of 2 µg of enzyme. Error bars represent standard deviation (n=3). Displayed is a Michaelis-Menten fit curve ($K_{0.5}$ = 16.8 µM, *n* = 1, blue dashed curve) contrasted with a Hill plot ($K_{0.5}$ = 16.8 µM, *n* = 1.54, solid red curve).

(i) Substrate range: 0-200 µM GSNO.

(ii) Substrate range: 0-60 µM GSNO.

2.4.2 Native GSNOR WT MS

Obtaining the mass spectra for the native protein GSNOR allows for calculation of the molecular weight. As well as viewing monomers, dimers, trimers, etc., if applicable. Performing this experiment proves that the dimer is involved in the HDX experiments, however not the protein solution is not purely dimerized.

The spectra obtained can be found in the **Appendix Figure B.1**, with peaks corresponding to monomeric GSNOR and dimerized GSNOR. The m/z values for these peaks is summarized in **Appendix Table B.1**. While the monomer peaks display as broad and unresolved, each subsequent dimer peak appears as three relatively distinct peaks (termed 1st, 2nd, and 3rd from low to high *m/z*). The molecular weight of these peaks were determined using ESIprot Online.[95] The results are displayed in **Table 2.4.2**. The three dimer peaks have an average first difference of 635 Da. Since GSNOR is known to carry NADH molecules throughout the purification process, this stepwise increase in mass could be explained by a dimer set with no NADH, a dimer with one monomer containing NADH, and a dimer with both monomers containing NADH. The molecular weight of NADH is 663 g/mol, which is within the combined errors of each calculated MW.

Table 2.4.2: Experimental MW of GSNOR, derived from native MS.

	Molecular Weight (Da)
Monomer	43384.06 ± 29.17
1st Dimer	86285.54 ± 54.54
2nd Dimer	86944.87 ± 47.89
3rd Dimer	87554.32 ± 29.43

2.4.3 GSNOR WT MS-MS Coverage Map

Obtaining identification of each peak in in MS fingerprint is necessary in order to produce a heat map of deuterium uptake. Thirty-two MS-MS spectra were obtained and successfully matched to peptide fragments of GNSOR. These peptides identified 188 unique amino acids which corresponds to about 50% sequence coverage. The list of these peptides and the corresponding sequence map is displayed in **Appendix B**. The sequence coverage can be extended by successfully matching other MS-MS spectra with the proper peptides. As well, incorporating chromatography in the MS process could theoretically help to increase the resolution of the peptides and aid in MS-MS data collection.

2.4.4 Previous Computational Studies

Previous molecular dynamics (MD) simulations were conducted in collaboration by Dr. B. Sun and Dr. B Mutus with Dr. James Gauld and his student S. Nikoo. These studies were performed in order to provide speculation into the possible allosteric binding site of GSNO.

A template crystal structure (PDB ID: 3QJ5) was used to perform the docking simulations using Molecular Operating Environment software (MOE, 2013.08; Chemical Computing Group Inc. Montréal, QC, Canada).[96] The results of the model implicated four amino acids in the binding of GSNO at a putative allosteric site. Asn185 and Gly321 appeared to interact with GSNO directly while Lys188 and Lys323 interacts indirectly, through a solvent network of hydrogen bonds. The study also provided docking score; these are used to predict binding affinity, with a low score indicating stability and favorable interactions. GSNO binding at the active site gave a score of -8.60 while the putative allosteric site has a score of -10.4.[96]

This punitive allosteric binding of GSNO and the implicated amino acid residues are displayed in **Figure 2.4.4a**.

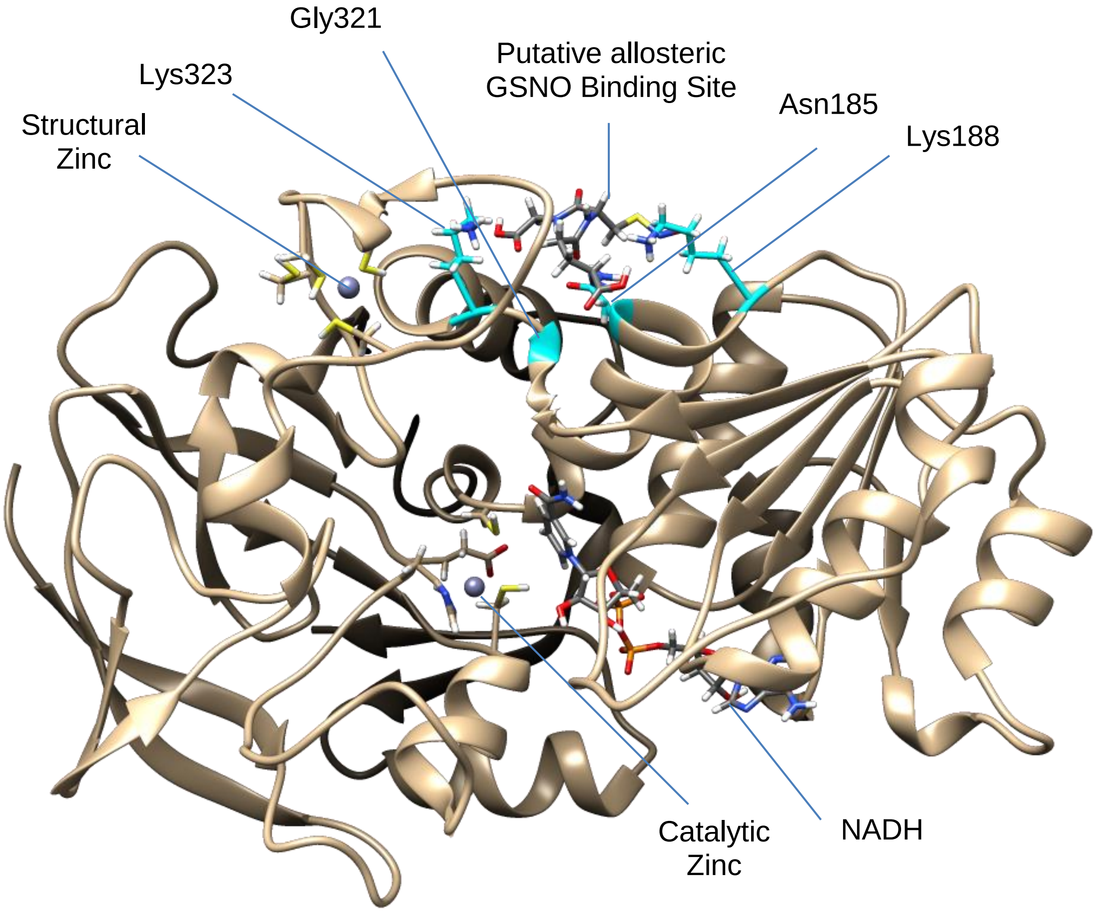

Figure 2.4.4a: Putative allosteric site near the structural zinc, as discovered by MD simulations. Asn185 and Gly321 are predicated to interact with GSNO directly while Lys188 and Lys323 interacts indirectly.

2.4.5 GSNOR WT HDX-MS

The custom TRESI device allowed for two static time points for the deuterium exchange reaction to occur; two seconds and four seconds were chosen.

Of the data obtained, six sets of data describing GSNOR peptides as they respond to deuterium incorporation were successfully analyzed. Sample spectra of this data can be seen in **Appendix D**, in **Figures D.1-3**. Baseline spectra displays peptides in a typical fashion of ESI peptides (**Figure D.1**); with the with the highest intensity peak being the first peak and subsequently decreasing in intensity. As deuterium is incorporated (**Figure D.2-3**), the peak distribution shifts with the addition of the heavier isotope. This shift is used to observe the overall amount of deuterium that is taken up by the peptide. The next layer of data incudes the incorporation of the substrate GSNO. Sample spectra of GSNOR + GNSO data can be seen in **Appendix D**, in **Figures D.4-6**. Two sets of GSNOR + GNSO HDX data were successfully analyzed.

Twenty times the concentration of GSNO was mixed in GSNOR, to ensure sufficient substrate was available to be observed interacting with the active site, as well as the putative allosteric site. While there are some subtle changes that can be viewed between the two spectrums', the most obvious is the appearance of a 613 m/z ($z = 1$) peak after the addition of GSNO. Based off literature MS studies of the GSNOR's kinetic processes, it is most likely that this peak corresponds to GSSG.[67] This is not unexpected, since the GSNO synthesized in-house was not completely pure, and degrades over time. This would lead to GSH being present in the sample used, and is also why the concentration if GSNO used is always confirmed with UV-Vis spectroscopy on the day of use. As well, it is not possible to purify GSNOR without residual NADH carried throughout the process. With the substrate and the cofactor present, some GSNO would be metabolized by the enzyme, leading to GSSG since GSH is present (**Figure 2.2.2a**). Excess GSNO and GSOOH (*if* any was produced) was not witnessed since both molecular weights are below 400 Da, and thus below the threshold of data acquired.

The results of these HDX-MS experiments are summarized in **Appendix D**. **Table D.1** offers a closer look at the peptide (I)PLYIPQCG(E) (residues 91-98). Here, the visible change that deuterium incorporation has on the peptide's peak distribution can be seen. Numeric summary of the two second exchange reaction time is displayed in **Table D.2** and the four second exchange reaction is in **Table D.3**. These tables provide the baseline deuterium uptake (%) for each peptide, which represents GSNOR data without GSNO. As well as the deuterium uptake (%) for each peptide with GSNO incorporated. The values of consequence, however, is the difference between these two values. Those values are what is superimposed on the crystal structures (**Figures 2.4.5 (a-b)**) to pictorially view the response to the presence of GSNO.

Four amino acid residues were implicated by computational means as being involved in the interaction of GSNO at a putative allosteric site; Asn185, Gly321, Lys188, and Lys323 (**Figure 2.4.4a**). While Asn185 is not represented by the identified peptide list, Lys188 and Lys323 are, as well as Gly321, which is represented twice. Under a two second exchange reaction, these residues all show a decrease in deuterium uptake (**Table 2.4.5**). This is displayed in **Figure 2.4.5a**, where the decrease in uptake is denoted with increasing shades of red. Areas with the largest decrease in uptake can be seen around this putative site, as well as in the active site pocket.

The results of the two second exchange reaction is at a contrast with the four second exchange. With double the time for allowed mixing, the majority of peptides displayed an increase in deuterium uptake. The notable exceptions are some peptides around the NADH binding region, as well the peripheral peptides in the same area. These peptides, located in the lower right quadrant of **Figure 2.4.5 (a-b)** show remarkedly similar uptake patterns at both time points. This exception also includes Lys188, whose peptide displays an uptake difference that is more negative than compared to the two second exchange data (**Table 2.4.5**).

Table 2.4.5: Δ Deuterium uptake of the amino acid residues implicated in allosteric biding.

	2 sec Exchange Δ Deuterium Uptake (%)	4 sec Exchange Δ Deuterium Uptake (%)	Representing Peptide Sequence
Asn185	N/A	N/A	N/A
Gly321	-0.9	+0.1	(W)/KGTAFG<u>G</u>WKS(V)
	-1.4	+0.5	(F)/G<u>G</u>WKSVESVPK(L)
Lys188	-0.4	-0.6	(T)A<u>K</u>LEPGSVC(A)
Lys323	-1.4	+0.5	(F)/GGWKSVESVP<u>K</u>(L)

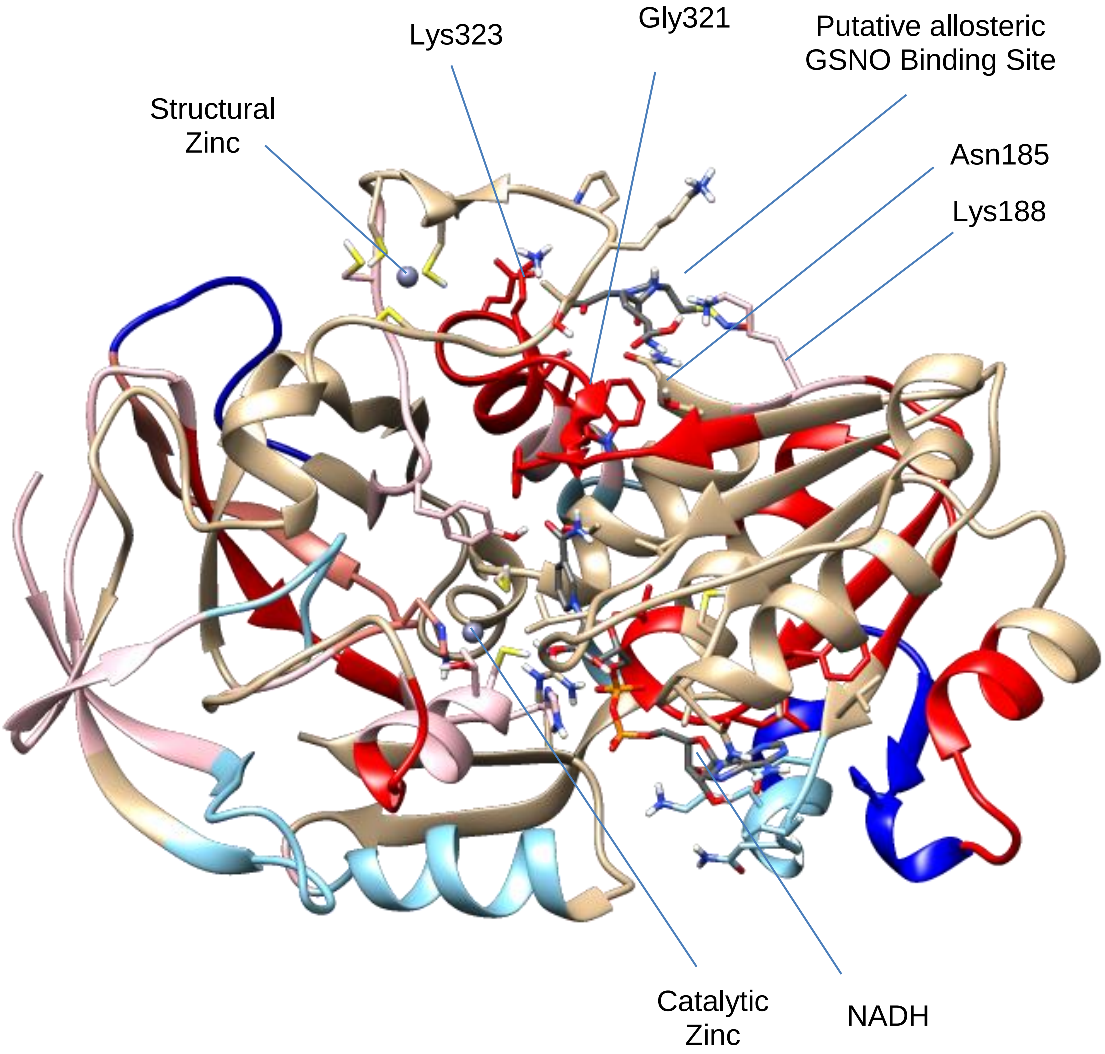

Δ Deuterium Uptake (%)					
Red	Salmon	Pink		Sky Blue	Blue
-1.8	-0.7	-0.4	0	0.6	3.4

Figure 2.4.5a: HDX-MS heat map after two seconds of deuterium exchange. Red conveys a decrease in deuterium incorporation after in inclusion of GSNO, Blue conveys an increase. The putative allosteric binding site with GSNO is shown, along with labels of the implicated resides involved in allosteric binding.

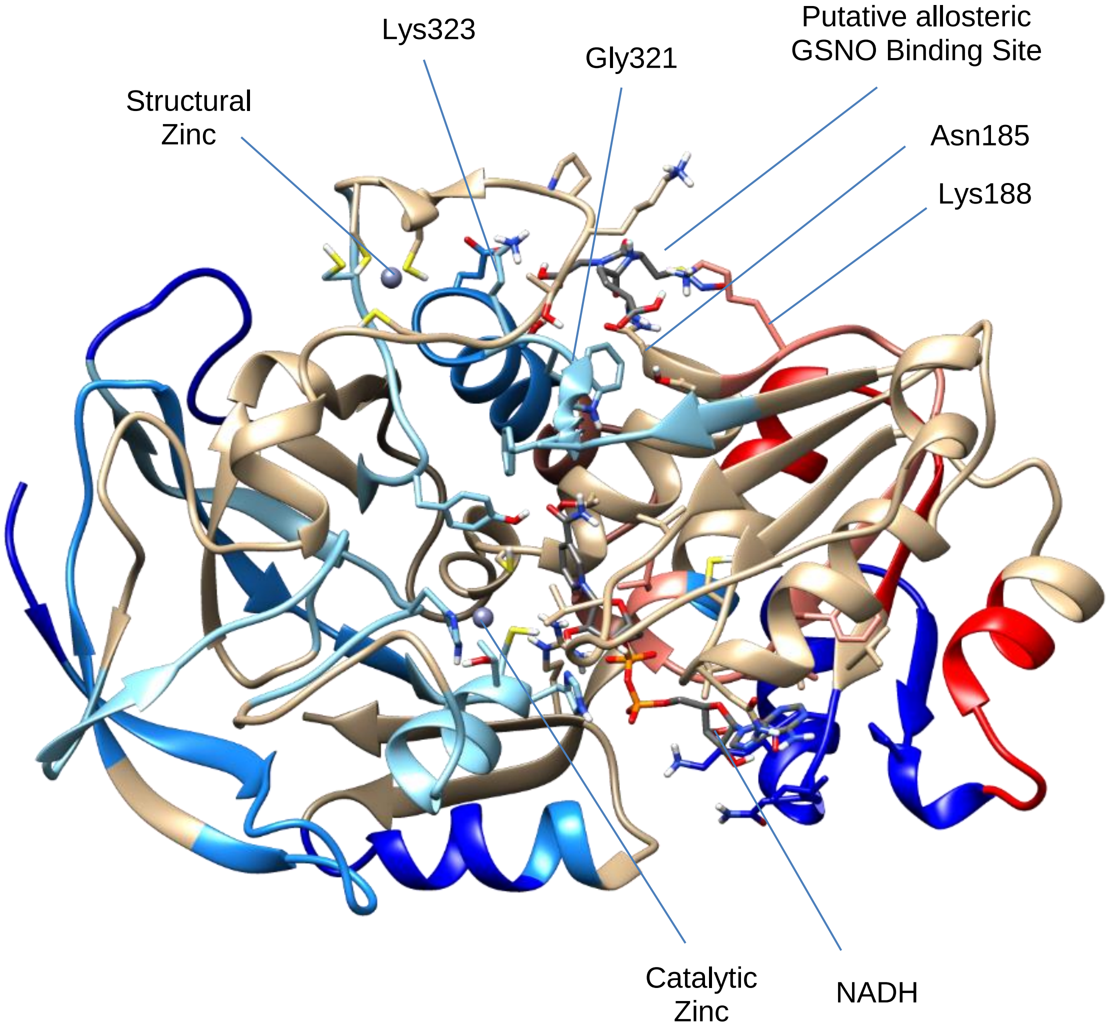

Δ Deuterium Uptake (%)					
Red	Salmon		Sky Blue	Dodger Blue	Blue
-5.2	-0.8	0	0.7	1.4	5.1

Figure 2.4.5b: HDX-MS heat map after four seconds of deuterium exchange. Red conveys a decrease in deuterium incorporation after in inclusion of GSNO, Blue conveys an increase. The putative allosteric binding site with GSNO is shown, along with labels of the implicated resides involved in allosteric binding.

2.5 Discussion

In addition to the preliminary computational studies, the enzyme kinetics of GSNOR, and HDX-MS studies at two reaction time points have been analyzed in the effort of supporting the hypothesis of the existence of an allosteric site.

2.5.1 GSNOR Kinetics

The steady state kinetic assays performed provide a convincing basis for the hypothesis of allosteric binding. With a Hill number (*n*) of 1.49 ± 0.037, there is indication of some form of cooperative binding being observed. In addition to this, the Hill Plot curve has a far superior fit in comparison to the basic Michaelis-Menten curve (**Figure 2.4.1b**); while utilizing the same values for V_{max} and $K_{0.5}/K_M$, which were experimentally derived. The Hill Plot can account for the slower rates when approaching $K_{0.5}$ while also observing the faster ascent to V_{max} that positive allosteric binding makes possible.

2.5.2 GSNOR HDX-MS: Two Second Exchange

Of the residues implicated in allosteric binding, Gly321, Lys188, and Lys323 have representing peptides identified by MS-MS. As can be seen in **Figure 2.4.5a**, these residues, and other peptides surrounding the computational placement of GSNO exhibit a decrease in deuterium uptake. Gly321, which is represented twice, displays a decrease of 0.9% and 1.4%, while Lys188 shows on a peptide that decreased of 0.4% and Lys323 decreased of 1.4%.

A decrease in deuterium uptake in peptides leading to the active site pocket, peptides involved in binding NADH, and of those binding to the catalytic zinc, was also observed. This included the amino acid residues Cys45 (-0.4%, TAVCHTDAYTLSGAD), His67 (-0.3%, ILGHEGAGIVESVGEG; -0.7%, GHEGAGIVESVGEGVT), and Glu68 (-0.3%, ILGHEGAGIVESVGEG; -0.7%, GHEGAGIVESVGEGVT), of which are involved in the binding of the catalytic zinc. Observing this decrease in solvent exposure around the active site is not unexpected or unwelcome; the fact that GSNO causes a change here adds another layer of legitimacy to the observations at the putative site. Further speculation on the HDX-MS structure patters can be found in **Section 2.5.3**.

The conformation of the structure used to display this data was obtained as a computationally minimized structure, followed by an induced fit at the active site.[96] The consequence of this is that the static image shows the monomer as slightly puckered, in comparison to the dimerized crystal structure (PDB ID: 3QJ5). Since Lys188 is the residue that displayed a decrease in solvent exposure at both time points, the distance between the α-carbon of Lys188 and the structural zinc since was chosen to display the differences in confirmation after binding of GSNO. The physical location of the other amino acid residues implicated in binding are located between Lys188 and the structural zinc. In the computationally untouched dimerized crystal structure, the distances displayed are 24.4 Å and 23.2 Å. The monomeric structures of the MD simulations have a shorter distance of 22.0 Å. Computationally minimized structures of the enzyme with GSNO in the allosteric site and active site, as well as just at the active site, while being bound as a dimer would be of interest; the further explore the structural effects of the allosteric site. **Figure 2.5.3a (iii-iv)** depict these distances.

Table 2.5.2: Distance between Lys188 and the structural zinc. These distances were determined using UCSF Chimera software.

Structure:	Distance between Lys188 and structural zinc (Å):
Dimerized crystal structure	24.409, 23.150
Minimized monomer	22.014

2.5.3 GSNOR HDX-MS: Four Second Exchange

With double the reaction time, the data obtained from the four second reactions move to more extreme changes in the uptake levels. While the two second reactions gave peptide changes in the -1.8% to +3.4% range, the four second reactions were found to be between -5.2% to +5.1% deuterium uptake change. As well, the majority of the peptides presented an increase in uptake levels, with only five peptides in the negative range. To counter this, there are also larger standard deviations in the values obtained for each peptide; the most extreme peptides on either side both have errors around 4%, easily the highest of all the data presented. This is not to negate the obvious trend observed, since there is clearly an increase in deuterium uptake across the span of peptides. With a longer time for the exchange reaction to occur, more time is present for the D_2O to displace the ligand-containing solvent surrounding the enzyme. The consequence of this larger time is that any observations of ligand interactions is essentially exchanged away. All that can be said for the amino acid Gly321 and Lys323 is that they do not exceed +0.5% change in deuterium uptake, while Lys188 exhibits -0.6% uptake.

The GSNOR dimer arranges itself with a central axis of β-pleated sheets. The regions that continue to display a decrease in deuterium uptake (with similar patterns to the two sec exchange data) are placed at each end of this ‘column’ of β-sheets. In the dimerized image shown in **Figure 2.5.3a (i-ii)**. One explanation for retention of negative uptake is that this section of the protein is less flexible, with more hydrogen bonding, and less likely to be affected by the increase in reaction time. It is entirely possible that this is the real putative site for GSNO docking, however, it is unlikely that GSNO would display a stronger interaction here over the active site.

The dimerized image in **Figure 2.5.3a (iii)** offers another perspective of the allosteric region; the dimers has been rotated 180^o on a horizontal axis, offering a ‘back-side’ view in comparison to the **Figure 2.5.3a (i-ii)** orientation. Although the GSNO is not shown, the binding regions of the allosteric site are shown by blue ovals. The blue dashed line connects Lys188 to the structural zinc.

(i)

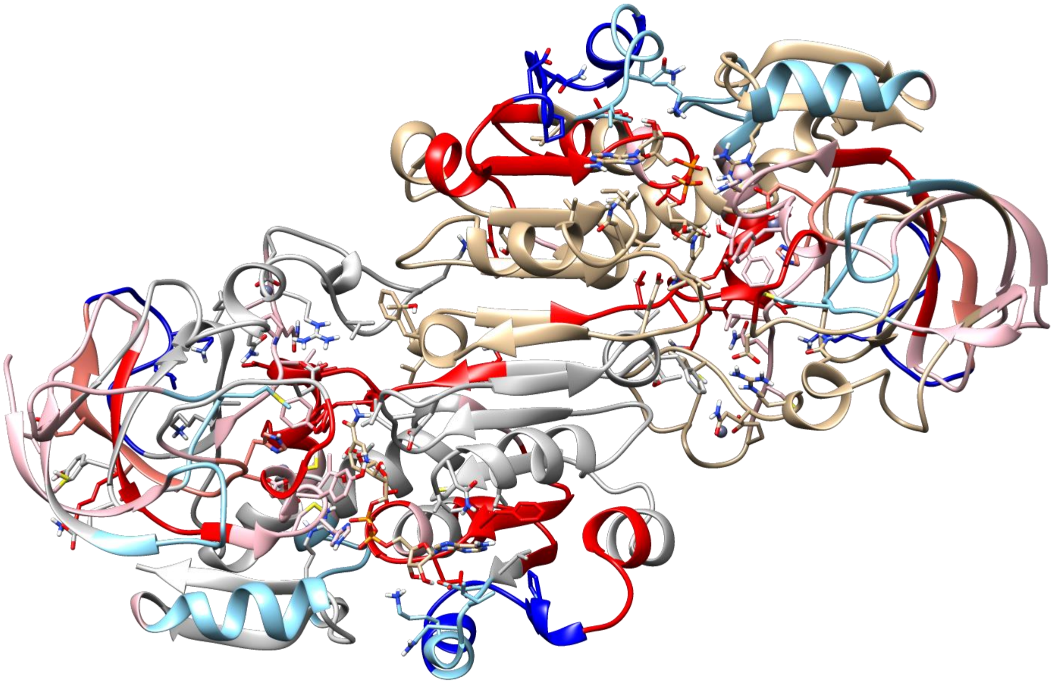

(ii)

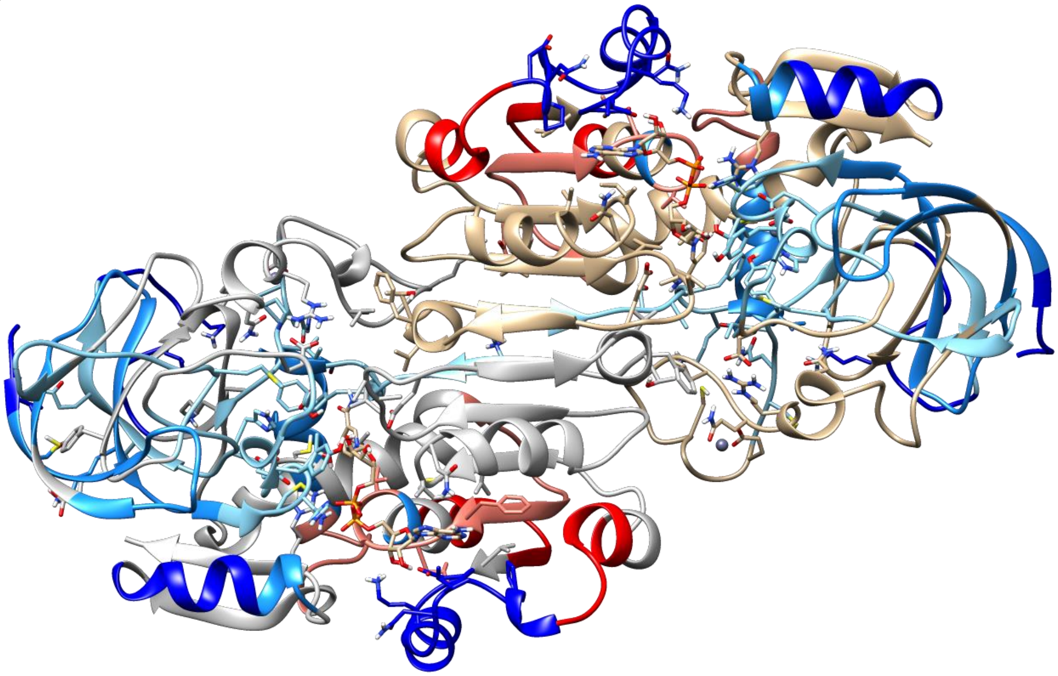

Figure 2.5.3a (i-ii): HDX-MS heat maps with dimerized GSNOR.

(i) GSNOR two second reaction data on dimerized structure.

(ii) GSNOR four second reaction data on dimerized structure.

(iii)

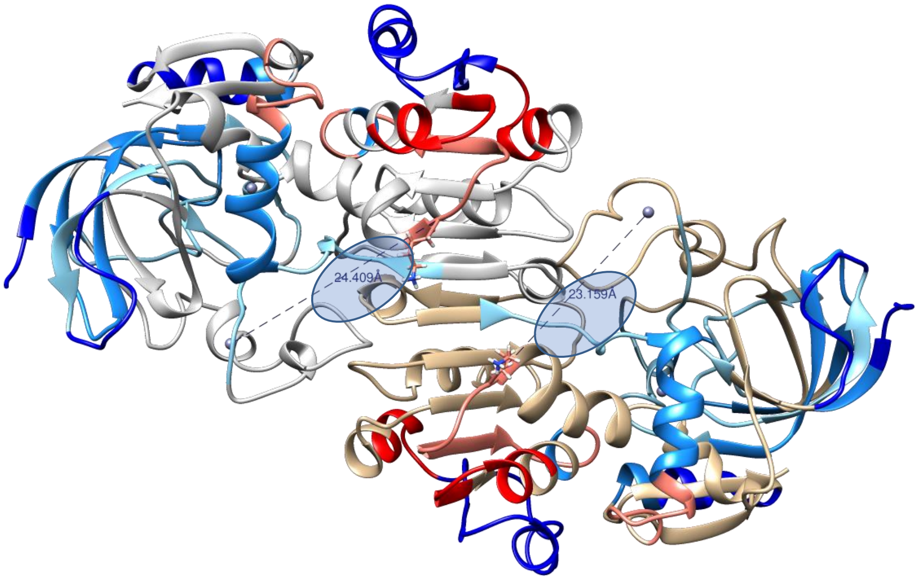

(iv)

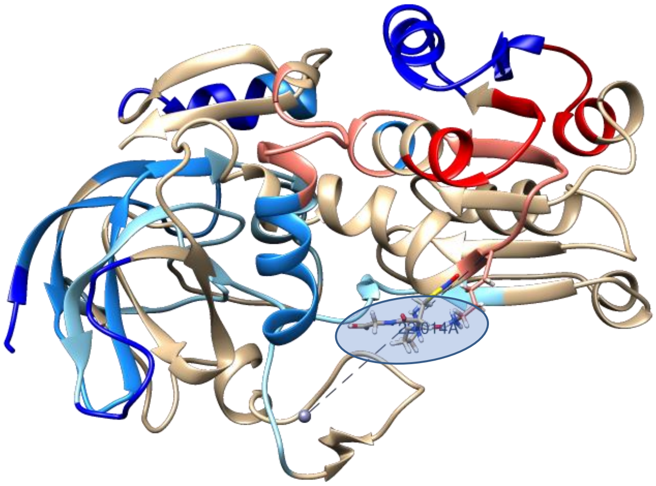

Figure 2.5.3a (iii-iv): HDX-MS heat maps with dimerized GSNOR.

(iii) 'Back-side' view of four second reaction data; 180º horizontal rotation of (ii). Blue circles demonstrate location of allosteric GSNO binding. Blue dashed lines denote the distance between the α-carbon of Lys188 and the structural zinc. The distances are 24.4 Å for the left sided monomer and 23.2 Å for the right.

(iv) Similar orientation of (iii), of the four second reaction data. GSNO is shown; blue dashed lines denote the distance between the α-carbon of Lys188 and the structural zinc, 22.0 Å.

2.6 Conclusion

This chapter supports the existence of a possible allosteric site on the enzyme S-nitrosoglutathione reductase (GSNOR). Experimental kinetic data provided a sigmoidal curve with a Hill coefficient (*n*) of 1.49 ± 0.037. This being greater than 1 suggests that the substrate S-nitrosoglutathione (GSNO) is binding in a cooperative manner. Molecular docking simulation on monomeric GSNOR presented a GSNOR binding site, located near the structural zinc. The amino acid residues Gly321, Lys323, Asn185, and Lys188 were implicated in the binding of GSNO at this site; peptides containing Gly321, Lys323, and Lys188 were successfully characterized by MS-MS. TRESI-HDX-MS studies were utilized to investigate this site further. Two and four second hydrogen to deuterium exchange reaction time points were observed. Under a two second HDX, the residues Gly321, Lys323, and Lys188 displayed a decrease of 1.4%, 1.4%, and 0.4%, respectively, after the addition of GSNO to the enzyme solution. This corresponds to a decrease in solvent exposure on the enzyme and supports the computational docking studies. Decreases were also observed around the active site, and NADH binding region. Under a four second HDX, the vast majority of peptides displayed an overall increase in deuterium uptake, in solvent exposure. This includes active site peptides and eludes to four seconds being too long to observe the interactions of GSNOR and GSNO.

2.7 Future Directions

To further investigate the validity of the putative allosteric site, site directed mutagenesis on Lys323 and Lys188 is in progress. By mutating both Lys323 and Lys188 to alanine, the loss of allosteric effects is hypothesized to be lost in the kinetic data. Other work includes successfully obtaining a third set of HDX-MS data of GNSOR + GSNO. As is, four sets of data were collected, with two sets being discarded due to discrepancies within the HDX GSNOR + GNSO spectra. One set was discarded due to notch failure of the TRESI device and thus improper mixing, leading to a dramatically reduced deuterium uptake observed. The second set of data discarded resulted in similar patterns, with very little deuterium uptake after the addition of GSNO despite the experimental conditions; the reasons for this has yet to be deduced. A third set is needed to have a complete triplicate data set.

BIBLIOGRAPHY

1. Wang, R., Two's company, three's a crowd: can H2S be the third endogenous gaseous transmitter? *FASEB Journal* **2002,** *16* (13), 1792-1798.

2. Mustafa, A. K.; Gadalla, M. M.; Snyder, S. H., Signaling by Gasotransmitters. *Sci. Signal.* **2009,** *2* (68).

3. Tinajero-Trejo, M.; Jesse, H. E.; Poole, R. K., Gasotransmitters, poisons, and antimicrobials: it's a gas, gas, gas! *F1000Prime Reports* **2013,** *5* (28).

4. Cooper, C. E.; Brown, G. C., The inhibition of mitochondrial cytochrome oxidase by the gases carbon monoxide, nitric oxide, hydrogen cyanide and hydrogen sulfide: chemical mechanism and physiological significance. *J Bioenerg Biomembr* **2008,** *40* (5), 533-539.

5. Ignarro, L. J.; Byrns, R. E.; Burga, G. M.; Wood, K. S., Endothelium-Derived Relaxing Factor From Pulmonary Artery and Vein Possesses Pharmacologic and Chemical Properties Identical to Those of Nitric Oxide Radical. *Circulation Research* **1987,** *61* (6), 866-879.

6. Ignarro, L. J.; Burga, G. M.; Wood, K. S.; Byrns, R. E.; Chaudhuri, G., Endothelium-derived relaxing factor produced and released from artery and vein is nitric oxide. *Proc Natl Acad Sci U S A* **1987,** *84* (24), 9265-9269.

7. Jeandroz, S.; Wipf, D.; Stuehr, D. J.; Lamattina, L.; Melkonian, M.; Tian, Z.; Zhu, Y.; Carpenter, E. J.; Ka-Shu Wong, G.; Wendehenne, D., Occurrence, structure, and evolution of nitric oxide synthase–like proteins in the plant kingdom. *Sci. Signal.* **2016,** *9* (17).

8. Treuer, A. V.; Gonzalex, D. R., Nitric oxide synthases, S-nitrosylation and cardiovascular health: From molecular mechanisms to therapeutic opportunities (Review). *Molecular Medicine Reports* **2014,** *11*, 1555-1565.

9. Rassaf, T.; Ferdinandy, P.; Schulz, R., Nitrite in organ protection. *British Journal of Pharmacology* **2013,** *171*, 1-11.

10. Willmota, M. R.; Batha, P. M. W., The potential of nitric oxide therapeutics in stroke. *Expert Opin Investig Drugs* **2003,** *12* (3), 455-470.

11. Misko, T. P.; Schilling, R. J.; Salvemini, D.; Moore, W. M.; Currie, M. G., A Fluorometric Assay for the Measurement of Nitrite in Biological Samples. *Analytical Biochemistry* **1993,** *214* (1), 11-16.

12. Garthwaite, J.; Charles, S. L.; Chess-Williams, R., Endothelium-derived relaxing factor release on activation of NMDA receptors suggests role as intercellular messenger in the brain. *Nature* **1988,** *336* (6197), 385-388.

13. Garthwaite, J.; Boulton, C. L., Nitric Oxide Signaling in the Central Nervous System. *Annu. Rev. Physiol.* **1995,** *57*, 683-706.

14. Witte, M. B.; Barbul, A., Role of nitric oxide in wound repair. *Am J Surg* **2002,** *183* (4), 406-412.

15. Kolios, G.; Valatas, V.; Ward, S. G., Nitric oxide in inflammatory bowel disease: a universal messenger in an unsolved puzzle. *Immunology* **2004,** *113* (4), 427-437.

16. Martinez, L. R.; Han, G.; Chacko, M.; Mihu, M. R.; Jacobson, M.; Gialanella, P.; Friedman, A. J.; Nosanchuk, J. D.; Friedman, J. M., Antimicrobial and Healing Efficacy of Sustained Release Nitric Oxide Nanoparticles Against Staphylococcus Aureus Skin Infection. *J Investig Dermatol* **2009,** *129* (10), 2463-2469.

17. Luo, J.; Chen, A. F., Nitric oxide: a newly discovered function on wound healing. *Acta Pharmacologica Sinica* **2005,** *26* (3), 259-264.

18. Ziche, M.; Morbidelli, L., Nitric oxide and angiogenesis. *J Neurooncol* **2000,** *50* (1-2), 139-148.

19. Schäffer, M. R.; Tantry, U.; Gross, S. S.; Wasserkrug, H. L.; Barbul, A., Nitric Oxide Regulates Wound Healing. *Journal of Surgical Research* **1996,** *63*, 237-240.

20. Heuer, K.; Hoffmanns, M. A.; Demir, E.; Baldus, S.; Volkmar, C. M.; Röhle, M.; Fuchs, P. C.; Awakowicz, P.; Suschek, C. V.; Opländer, C., The topical use of non-thermal dielectric barrier discharge (DBD): Nitric oxide related effects on human skin. *Nitric Oxide* **2015,** *44*, 52-60.

21. Rundhaug, J. E., Matrix metalloproteinases and angiogenesis. *J Cell Mol Med* **2005,** *9* (2), 267-285.

22. Ridnour, L. A.; Windhausen, A. N.; Isenberg, J. S.; Yeung, N.; Thomas, D. D.; Vitek, M. P.; Roberts, D. D.; Wink, D. A., Nitric oxide regulates matrix metalloproteinase-9 activity by guanylyl-cyclase-dependent and -independent pathways. *PNAS* **2007,** *104* (43), 16898-16903.

23. Lee, C. Z.; Xue, Z.; Hao, Q.; Yang, G.-Y.; Young, W. L., Nitric Oxide in Vascular Endothelial Growth Factor-Induced Focal Angiogenesis and Matrix Metalloproteinase-9 Activity in the Mouse Brain. *Stroke* **2009,** *40*, 2879-2881.

24. Lacey, J. E.; Grabowski, P. S.; Skerry, T. M., Nitric oxide activates matrix metalloproteinases indirectly in human articular chondrocytes. *Int J Exp Pathol* **2000,** *81* (1), A17.

25. Williams, S. B.; Cusco, J. A.; Roddy, M.-A.; Johnstone, M. T.; Creager, M. A., Impaired nitric oxide-mediated vasodilation in patients with non-insulin-dependent diabetes mellitus. *Clinical Study* **1996,** *27* (3), 567-574.

26. Lin, K. Y.; Ito, A.; Asagami, T.; Tsao, P. S.; Adimoolam, S.; Kimoto, M.; Tsuji, H.; Reaven, G. M.; Cooke, J. P., Impaired Nitric Oxide Synthase Pathway in Diabetes Mellitus. *Circulation* **2002,** *106*, 987-992.

27. Foster, M. W.; McMahon, T. J.; Stamler, J. S., S-nitrosylation in health and disease. *Trends in Molecular Medicine* **2003,** *9* (4), 391-404.

28. Bhatraju, P.; Crawford, J.; Hall, M.; Lang, J. D. J., Inhaled Nitric Oxide: Current Clinical Concepts. *Nitric Oxide* **2015,** *50*, 114-128.

29. Frost, M. C.; Reynolds, M. M.; Meyerhoff, M. E., Polymers incorporating nitric oxide releasing/generating substances for improved biocompatibility of blood-contacting medical devices. *Biomaterials* **2005,** *26*, 1685-1693.

30. Elnaggar, M. A.; Seo, S. H.; Gobaa, S.; Lim, K. S.; Bae, I.-H.; Jeong, M. H.; Han, D. K.; Joung, Y. K., Nitric Oxide Releasing Coronary Stent: A New Approach Using Layer-by-Layer Coating and Liposomal Encapsulation. *Small* **2016,** *12* (43), 6012-6023.

31. Wonoputri, V.; Gunawan, C.; Liu, S.; Barraud, N.; Yee, L. H.; Lim, M.; Amal, R., Copper Complex in Poly(vinyl chloride) as a Nitric Oxide-Generating Catalyst for the Control of Nitrifying Bacterial Biofilms. *ACS Appl Mater Inter* **2015,** *7* (40), 22148–22156.

32. Islam, M.; Masum, S.; Rahman, M.; Molla, A. I.; Shaikh, A. A., Preparation of Chitosan from Shrimp Shell and Investigation of Its Properties. *International Journal of Basic and Applied Sciences* **2011,** *11* (1), 77-80.

33. Dutta, P. K.; Dutta, J.; Tripathi, V. S., Chitin and chitosan: Chemistry , properties and applications. *J Sci Ind Res* **2004,** *63*, 20-31.

34. Kim, J.-Y.; Jun, J.-H.; Kim, S.-J.; Hwang, K.-M.; Choi, S. R.; Han, S. D.; Son, M.-W.; Park, E.-S., Wound healing efficacy of a chitosan-based film-forming gel containing tyrothricin in various rat wound models. *Arch. Pharm. Res.* **2015,** *38*, 229-238.

35. Archanaa, D.; Singha, B. K.; Duttab, J.; Duttaa, P. K., Chitosan-PVP-nano silver oxide wound dressing: In vitro and in vivo evaluation. *International Journal of Biological Macromolecules* **2015,** *73*, 49-57.

36. Sivashankari, P. R.; Prabaharan, M., Prospects of chitosan-based scaffolds for growth factor release in tissue engineering. *International Journal of Biological Macromolecules* **2016,** *93B*, 1382-1389.

37. Fontana, K.; Mutus, B., Nitric Oxide-Donating Devices for Topical Applications. In *Nitric Oxide Donors: Novel Biomedical Applications and Perspectives*, Seabra, A., Ed. Elsevier Science: 2017; pp 55-74.

38. Guchhait, S. K.; Chandgude, A. L.; Priyadarshani, G., CuSO4–Glucose for in Situ Generation of Controlled Cu(I)–Cu(II) Bicatalysts: Multicomponent Reaction of Heterocyclic Azine and Aldehyde with Alkyne, and Cycloisomerization toward Synthesis of N-Fused Imidazoles. *J Org Chem* **2012,** *77* (9), 4438-4444.

39. Singh, S. V.; Saxena, C.; Singh, M. P., Mechanism of Copper (11) Oxidation of Reducing Sugars. I. Kinetics and Mechanism of Oxidation of D-Xylose, L-Arabinose, D-Ghcose, D-Fructose, D-Mannose, D-Galactose, L-Sorbose, Lactose, Maltose, Cellobiose, and Melibiose by Copper(11) in Alkaline Medium. *J Am Chem Soc* **1970,** *92* (3), 537-541.

40. Sugaya, S.; Yamada, M.; Hori, A.; Seki, M., Microfluidic production of single micrometer-sized hydrogel beads utilizing droplet dissolution in a polar solvent. *Biomicrofluidics* **2013,** *7*.

41. Piknova, B.; Schechter, A. N., Measurement of Nitrite in Blood Samples Using the Ferricyanide-Based Hemoglobin Oxidation Assay. *Methods Mol Biol* **2011,** *704*, 39-56.

42. Faccenda, A.; Wang, J.; Mutus, B., Polydimethylsiloxane Permeability-Based Method for the Continuous and Specific Detection of Hydrogen Sulfide. *Anal Chem* **2012,** *84* (12), 5243-5249.

43. Toth, M.; Sohail, A.; Fridman, R., Assessment of gelatinases (MMP-2 and MMP-9) by gelatin zymography. *Methods Mol Biol* **2012,** *878*, 121-135.

44. abcam Gelatin zymography protocol http://www.abcam.com/protocols/gelatin-zymography-protocol (accessed March).

45. Sarma, M.; Mondal, B., Nitric Oxide Reduction of Copper(II) Complexes: Spectroscopic Evidence of Copper(II) Nitrosyl Intermediate. *Inorg Chem* **2011,** *50* (8), 3206-3212.

46. Frost, W. H. M. C., Direct measurement of actual levels of nitric oxide (NO) in cell culture conditions using soluble NO donors. *Redox Biol* **2016,** *9*, 1-14.

47. Zaragoza, C.; Balbín, M.; López-Otín, C.; Lamas, S., Nitric oxide regulates matrix metalloprotease-13 expression and activity in endothelium. *Kidney Int* **2002,** *61* (3), 804-808.

48. Sasaki, K.; Hattori, T.; Fujisawa, T.; Takahashi, K.; Inoue, H.; Takigawa, M., Nitric Oxide Mediates Interleukin-1-Induced Gene Expression of Matrix Metalloproteinases and Basic Fibroblast Growth Factor in Cultured Rabbit Articular Chondrocytes. *J Biochem* **1998,** *123* (3), 431-439.

49. McCarthy, S. M.; Bove, P. F.; Matthews, D. E.; Akaike, T.; Vliet, A. v. d., Nitric Oxide Regulation of MMP-9 Activation and Its Relationship to Modifications of the Cysteine Switch. *Biochemistry* **2008,** *47* (21), 5832-5840.

50. Hirai, Y.; Migita, K.; Hondaa, S.; Ueki, Y.; Yamasaki, S.; Urayama, S.; Kamachi, M.; Kawakami, A.; Ida, H.; Kita, M.; Fukuda, T.; Shibatomi, K.; Kawabe, Y.; Aoyagi, T.; Eguchi, K., Effects of nitric oxide on matrix metalloproteinase-2 production by rheumatoid synovial cells. *Life Sci* **2001,** *68* (8), 913-920.

51. Jurasz, P.; Sawicki, G.; Duszyk, M.; Sawicka, J.; Miranda, C.; Mayers, I.; Radomsk, M. W., Matrix metalloproteinase 2 in tumor cell-induced platelet aggregation: regulation by nitric oxide. *Cancer Res* **2001,** *61* (1), 376-382.

52. Pustovrh, C.; Jawerbaum, A.; Sinner, D.; Pesaresi, M.; Baier, M.; Micone, P.; Gimeno, M.; Gonzalez, E. T., Membrane-type matrix metalloproteinase-9 activity in placental tissue from patients with pre-existing and gestational diabetes mellitus. *Reprod Fertil Dev* **2000,** *12* (5-6), 269-275.

53. Bove, P. F.; Wesley, U. V.; Greul, A.-K.; Hristova, M.; Dostmann, W. R.; Vliet, A. v. d., Nitric oxide promotes airway epithelial wound repair through enhanced activation of MMP-9. *Am J Respir Cell Mol Biol* **2007,** *36* (2), 138-146.

54. Smith, M., Genetics of human alcohol and aldehyde dehydrogenases. *Adv Hum Genet* **1986,** *15*, 249-290.

55. Jensen, D. E.; Belka, G. K.; Bois, G. C. D., S-Nitrosoglutathione is a substrate for rat alcohol dehydrogenase class III isoenzyme. *Biochem J* **1998,** *331*, 659-668.

56. Hedberg, J. J.; Hoog, J.-O.; Nilsson, J. A.; Xi, Z.; Elfwing, Å.; Grafstro, R. C., Expression of alcohol dehydrogenase 3 in tissue and cultured cells from human oral mucosa. *Am J Pathol* **2000,** *157* (5), 1745-1755.

57. Hopkinson, R. J.; Barlow, P. S.; Schofield, C. J.; Claridge, T. D. W., Studies on the reaction of glutathione and formaldehyde using NMR. *Org Biomol Chem* **2010,** *8* (24), 4915-4920.

58. Barnett, S. D.; Buxton, I. L. O., The Role of S-nitrosoglutathione Reductase (GSNOR) in Human Disease and Therapy. *Crit Rev Biochem Mol Biol* **2017,** *52* (3), 340-354.

59. Foglio, M. H.; Duester, G., Characterization of the functional gene encoding mouse class I11 alcohol dehydrogenase (glutathione-dependent formaldehyde dehydrogenase) and an unexpressed processed pseudogene with an intact open reading frame *Eur J Biochem* **1996,** *237* (2), 496-504.

60. Leterrier, M.; Chaki, M.; Airaki, M.; Valderrama, R.; Palma, J. M.; Barroso, J. B.; Corpas, F. J., Function of S-nitrosoglutathione reductase (GSNOR) in plant development and under biotic/abiotic stress. *Pant Signal Behav* **2011,** *6* (6), 789-793.

61. Fagerberg, L.; Hallstro, B. M.; Oksvold, P.; Kampf, C.; Djureinovic, D.; Odeberg, J.; Habuka, M.; Tahmasebpoor, S.; Danielsson, A.; Edlund, K.; Asplund, A.; Sjostedt, E.; Lundberg, E.; Szigyarto, C. A.-K.; Skogs, M.; Takanen, J. O.; Berling, H.; Tegel, H.; Mulder, J.; Nilsson, P.; Schwenk, J. M.; Lindskog, C.; Danielsson, F.; Mardinoglu, A.; Sivertsson, Å.; Feilitzen, K. v.; Forsberg, M.; Zwahlen, M.; Olsson, I.; Navani, S.; Huss, M.; Nielsen, J.; Ponten, F.; Uhlen, M., Analysis of the Human Tissue-specific Expression by Genome-wide Integration of Transcriptomics and Antibody-based Proteomics. *Molecular & Cellular Proteomics* **2014,** *13* (2), 397-406.

62. Fernández, M. R.; Biosca, J. A.; Parés, X., S-nitrosoglutathione reductase activity of human and yeast glutathione-dependent formaldehyde dehydrogenase and its nuclear and cytoplasmic localisation. *Cell Mol Life Sci* **2003,** *60* (5), 1013-1018.

63. Sanghani, P. C.; Davis, W. I.; Zhai, L.; Robinson, H., Structure-Function Relationships in Human Glutathione-Dependent Formaldehyde Dehydrogenase. Role of Glu-67 and Arg-368 in the Catalytic Mechanism. *Biochemistry* **2006,** *45*, 4819-4830.

64. Kubienová, L.; Kopecný, D.; Tylichová, M.; Briozzo, P.; Skopalová, J.; Sebela, M.; Navrátil, M.; Tâche, R.; Luhová, L.; Barroso, J. B.; Petrivalský, M., Structural and functional characterization of a plant S-nitrosoglutathione reductase from Solanum lycopersicum. *Biochimie* **2013,** *95* (4), 889-902.

65. Guerra, D.; Ballard, K.; Truebridge, I.; Vierling, E., S-nitrosation of conserved cysteines modulates activity and stability of S-nitrosoglutathione reductase (GSNOR). *Biochemistry* **2016,** *55* (17), 2452-2464.

66. Bühler, R.; Hempel, J.; Kaiser, R.; Wartburg, J.-P. v.; Vallee, B. L.; Jörnvall, H., Human alcohol dehydrogenase: structural differences between the beta and gamma subunits suggest parallel duplications in isoenzyme evolution and predominant expression of separate gene descendants in livers of different mammals. *Proc Natl Acad Sci U S A* **1984,** *81* (20), 6320-6324.

67. Hedberg, J. J.; Griffiths, W. J.; Nilsson, S. J. F.; Höög, J.-O., Reduction of S-nitrosoglutathione by human alcohol dehydrogenase 3 is an irreversible reaction as analysed by electrospray mass spectrometry. *Eur J Biochem* **2003,** *270* (6), 1249-2156.

68. Lamattina, L.; García-Mata, C., *Gasotransmitters in Plants: The Rise of a New Paradigm in Cell Signaling*. Springer International Publishing: 2016.

69. Foster, M. W.; Hess, D. T.; Stamler, J. S., Protein S-nitrosylation in health and disease: a current perspective. *Trends Mol Med* **2009,** *15* (9), 391-404.

70. Sanghani, P. C.; Davis, W. I.; Fears, S. L.; Green, S.-L.; Zhai, L.; Tang, Y.; Martin, E.; Bryan, N. S.; Sanghani, S. P., Kinetic and Cellular Characterization of Novel Inhibitors of S-nitrosoglutathione reductase. *J Biol Chem* **2009,** *284* (36), 24354-24362.

71. Staaba, C. A.; Hellgrena, M.; Grafströmb, R. C.; Höög, J.-O., Medium-chain fatty acids and glutathione derivatives as inhibitors of S-nitrosoglutathione reduction mediated by alcohol dehydrogenase 3. *Chem Biol Interact* **2009,** *180* (1), 113-118.

72. Bobadilla, J. L.; Macek, M. J.; Fine, J. P.; Farrell, P. M., Cystic fibrosis: A worldwide analysis of CFTR mutations—correlation with incidence data and application to screening. *Hum Mutat* **2002,** *19* (6), 575-606.

73. Donaldson, S. H.; Solomon, G. M.; Zeitlin, P. L.; Flume, P. A.; Casey, A.; McCoy, K.; Zemanick, E. T.; Mandagere, A.; Troha, J. M.; Shoemaker, S. A.; Chmiel, J. F.; Taylor-Cousar, J. L., Pharmacokinetics and safety of cavosonstat (N91115) in healthy and cystic fibrosis adults homozygous for F 508 DEL - CFTR. *J Cyst Fibros* **2017,** *16* (3), 371-379.

74. Green, L. S.; Chun, L. E.; Patton, A. K.; Sun, X.; Rosenthal, G. J.; Richards, J. P., Mechanism of Inhibition for N6022, a First-in-Class Drug Targeting S-Nitrosoglutathione Reductase. *Biochemistry* **2012,** *51*, 2157-2168.

75. Chen, Q.; Sievers, R. E.; Varga, M.; Kharait, S.; Haddad, D. J.; Patton, A. K.; Mutka, C. S. D. S. C.; Blonder, J. P.; Dubé, G. P.; Rosenthal, G. J.; Springer, M. L., Pharmacological inhibition of S-nitrosoglutathione reductase improves endothelial vasodilatory function in rats in vivo. *J Appl Physiol (1985)* **2013,** *114* (6), 752-760.

76. Kovacs, I.; Holzmeister, C.; Wirtz, M.; Geerlof, A.; Fröhlich, T.; Römling, G.; Kuruthukulangarakoola, G. T.; Linster, E.; Hell, R.; Arnold, G. J.; Durner, J.; Lindermayr, C., ROS-Mediated Inhibition of S-nitrosoglutathione Reductase Contributes to the Activation of Anti-oxidative Mechanisms. *Front Plant Sci* **2016,** *7*.

77. Voet, D.; Voet, J. G.; Pratt, C. W., Enzyme Kinetics, Inhibition, and Control. In *Fundamentals of Biochemistry: Life at the Molecular Level 4th Edition*, John Wiley & Sons, Inc.: pp 366-395.

78. Bhagavan, N. V.; Ha, C.-E., Enzymes and Enzyme Regulation. In *Essentials of Medical Biochemistry 2nd Edition*, Academic Press: 2015; pp 47-58.

79. Domon, B.; Aebersold, R., Mass Spectrometry and Protein Analysis. *Science* **2006,** *312* (5771), 212-217.

80. Dole, M.; Mack, L. L.; Hines, R. L.; Mobley, R. C.; Ferguson, L. D.; Alice, M. B., Molecular Beams of Macroions. *J Chem Phys* **1968,** *49* (2), 2240-2249.

81. Whitehouse, C. M.; Dreyer, R. N.; Yamashita, M.; Fenn, J. B., Electrospray interface for liquid chromatographs and mass spectrometers. *Anal Chem* **1895,** *57* (3), 675-679.

82. Kebarle, P.; Verkerk, U. H., Electrospray: from ions in solution to ions in the gas phase, what we know now. *Mass Spectrom Rev* **2009,** *28* (6), 898-917.

83. Lento, C. Obtaining Structural Insights on Bacterial Protein Complexes Using Time-Resolved Hydrogen-Deuterium Exchange Mass Spectrometry. York University, 2015.

84. Bruins, A. P., Mechanistic aspects of electrospray ionization. *J of Chromatography A* **1998,** *794* (1-2), 345-357.

85. Ho, C. S.; Lam, C. W. K.; Chan, M. H. M.; Cheung, R. C. K.; Law, L. K.; Lit, L. C. W.; Ng, K. F.; Suen, M. W. M.; Tai, H. L., Electrospray Ionisation Mass Spectrometry: Principles and Clinical Applications. *Clin Biochem Rev* **2003,** *24* (1), 3-12.

86. Konermann, L.; Pan, J.; Liu, Y.-H., Hydrogen exchange mass spectrometry for studying protein structure and dynamics. *Chem Soc Rev* **2011,** *40* (3), 1224-1234.

87. Marciano, D. P.; Dharmarajan, V.; Griffin, P. R., HDX-MS guided drug discovery: small molecules and biopharmaceuticals. *Current Opinion in Structural Biology* **2014,** *28*, 105-111.

88. Beeston, H. S.; Ault, J. R.; Pringle, S. D.; Brown, J. M.; Ashcroft, A. E., Changes in protein structure monitored by use of gas-phase hydrogen/deuterium exchange. *Proteomics* **2015,** *15* (16), 2842-2850.

89. Gallagher, E. S.; Hudgens, J. W., Mapping Protein-Ligand Interactions with Proteolytic Fragmentation, Hydrogen/Deuterium Exchange-Mass Spectrometry. *Methods Enzymol* **2016,** *566*, 357-404.

90. Dempsey, C. E., Hydrogen exchange in peptides and proteins using NMR spectroscopy. *Prog Nucl Magn Reson Spectrosc* **2001,** *39* (2), 135-170.

91. Wilson, D. J.; Konermann, L., A Capillary Mixer with Adjustable Reaction Chamber Volume for Millisecond Time-Resolved Studies by Electrospray Mass Spectrometry. *Anal Chem* **2003,** *75*, 6408-6414.

92. Hart, T. W., Some observations concerning S-nitroso-and S-phenylsulfonylderivatives of L-cysteine and glutathione. *Tetrahedron Lett.* **1985,** *26*, 2013-2016.

93. Broniowska, K. A.; Diers, A. R.; Hogg, N., S-Nitrosoglutathione. *Biochim Biophys Acta* **2013,** *1830* (5), 3173-3181.

94. Liuni, P.; Rob, T.; Wilson, D. J., A microfluidic reactor for rapid, low-pressure proteolysis with on-chip electrospray ionization. *Rapid Commun Mass Spectrom* **2010,** *24*, 315-320.

95. Winkler, R., ESIprot: a universal tool for charge state determination and molecular weight calculation of proteins from electrospray ionization mass spectrometry data. *Rapid Commun Mass Spectrom* **2010,** *24* (3), 285-294.

96. Sun, B. Biochemical and Functional Studies of S-nitrosoglutathione Reductase and Neutral Sphingomyelinase II. University of Windsor, Electronic Theses and Dissertations, 2017.

APPENDIX

APPENDIX A – Recombinant GSNOR

Figure A.1: Recombinant wild type GSNOR protein sequence.

Figure A.2: Recombinant GSNOR Plasmid Map.

APPENDIX B – Mass Spectrometry: Native GSNOR

Figure B.1: Native GSNOR MS Spectra.

Table B1: Native GSNOR MS spectra peak m/z values and relative intensities.

APPENDIX C – Mass Spectrometry: MS-MS GSNOR

Figure C.1: GSNOR MS-MS Peptide Map.

Table C.1: Full peptide list resulting from MS-MS identification.

APPENDIX D – Mass Spectrometry: HDX-MS GSNOR

Figure D.1: GSNOR MS fingerprint, with pepsin fragmentation.

Figure D.2: GSNOR HDX-MS with two seconds reaction time.

Figure D.3: GSNOR HDX-MS with four seconds reaction time.

Figure D.4: GSNOR + 20x GSNO MS fingerprint, with pepsin fragmentation.

Figure D.5: GSNOR + 20x GSNO HDX-MS with two seconds reaction time.

Figure D.6: GSNOR + 20x GSNO HDX-MS with four seconds reaction time.

Table D.1: Representative peptide to visualize deuterium uptake.

Table D.2: Deuterium uptake results of two second reaction time.

Table D.3: Deuterium uptake results of four second reaction time.

APPENDIX A – Recombinant GSNOR

		1 10	20
MGSSHHHHHH	*SSGLVPRGSH*	MANEVIKCKA	AVAWEAGKPL
30	40	50	60
SIEEIEVAPP	KAHEVRIKIIA	TAVCHTDAY	TLSGADPEGC
70	80	90	100
FPVILGHEGA	GIVESVGEGV	TKLKAGDTVI	PLYIPQCGEC
110	120	130	140
KFCLNPKTNL	CQKIRVTQGK	GLMPDGTSRF	TCKGKTILHY
150	160	170	180
MGTSTFSEYT	VVADISVAKI	DPLAPLDKVC	LLGCGISTGY
190	200	210	220
GAAVNTAKLE	PGSVCAVFGL	GGVGLAVIMG	CKVAGASRII
230	240	250	260
GVDINKDKFA	RAKEFGATEC	INPQDFSKPI	QEVLIEMTDG
270	280	290	300
GVDYSFECIG	NVKVMRAALE	ACHKGWGVSV	VVGVAASGEE
310	320	330	340
IATRPFQLVT	GRTWKGTAFG	GWKSVESVPK	LVSEYMSKKI
250	360	370	374
KVDEFVTHNL	SFDEINKAFE	LMHSGKSIRT	VVKI
LEHHHHHH			

Figure A.1: Recombinant wild type GSNOR protein sequence. Amino acids are numbered from Met1 to Ile374, excluding the added histidine-tag (italicized).

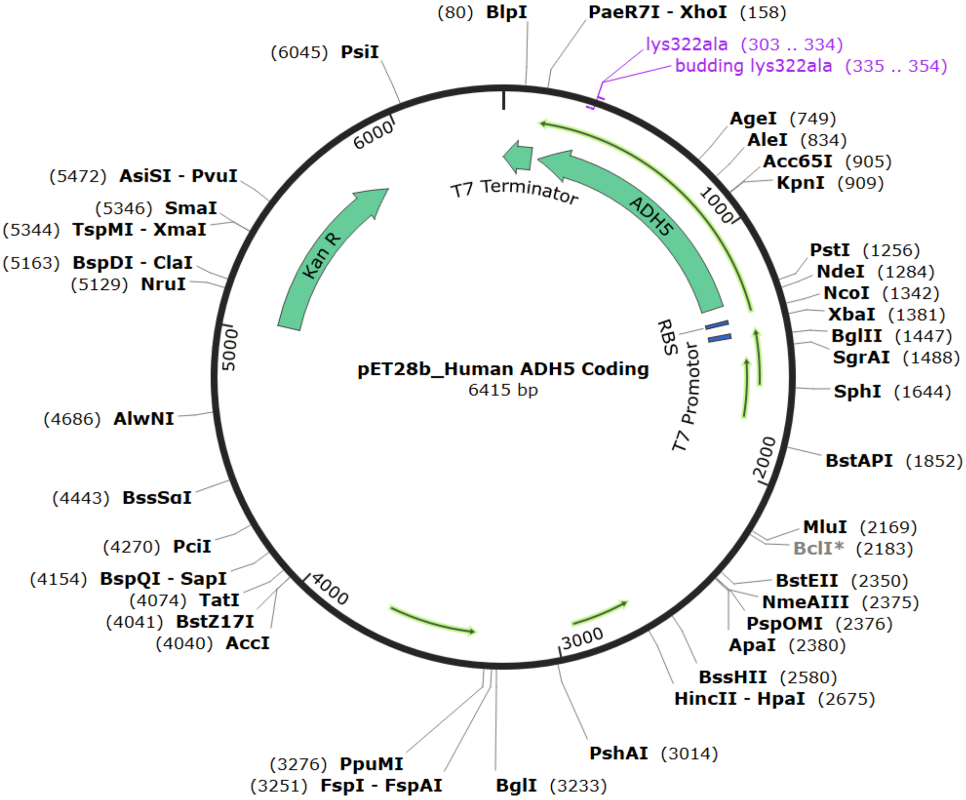

Figure A.2: Recombinant GSNOR Plasmid Map.

The following was designed and performed by Dr Bei Sun.[96]

Human ADH5 was purchased from Origene (SC119755) and sub-cloned into the bacterial expression vector pET28b using Cold Fusion Cloning Kit (MJS BioLynx Inc. SYMC010A1). The following primers for PCR were designed according to manufacturer's guidelines:

Forward 5' –GTGCCGCGCGGCAGCCATATGGCGAACGAGGTTATCAAG– 3'

Reverse 5' –GTGGTGGTGGTGGTGCTCGAGAATCTTTACAACAGTTCGAATG– 3'

Colonies were screened using diagnostic restriction enzyme digest and by partial sequencing (Robart's Research Institute, London Regional Genomics Center, London, Ontario, Canada). The final recombinant GSNOR contains a 6X-histidine tag at each terminus.

APPENDIX B – Mass Spectrometry: Native GSNOR

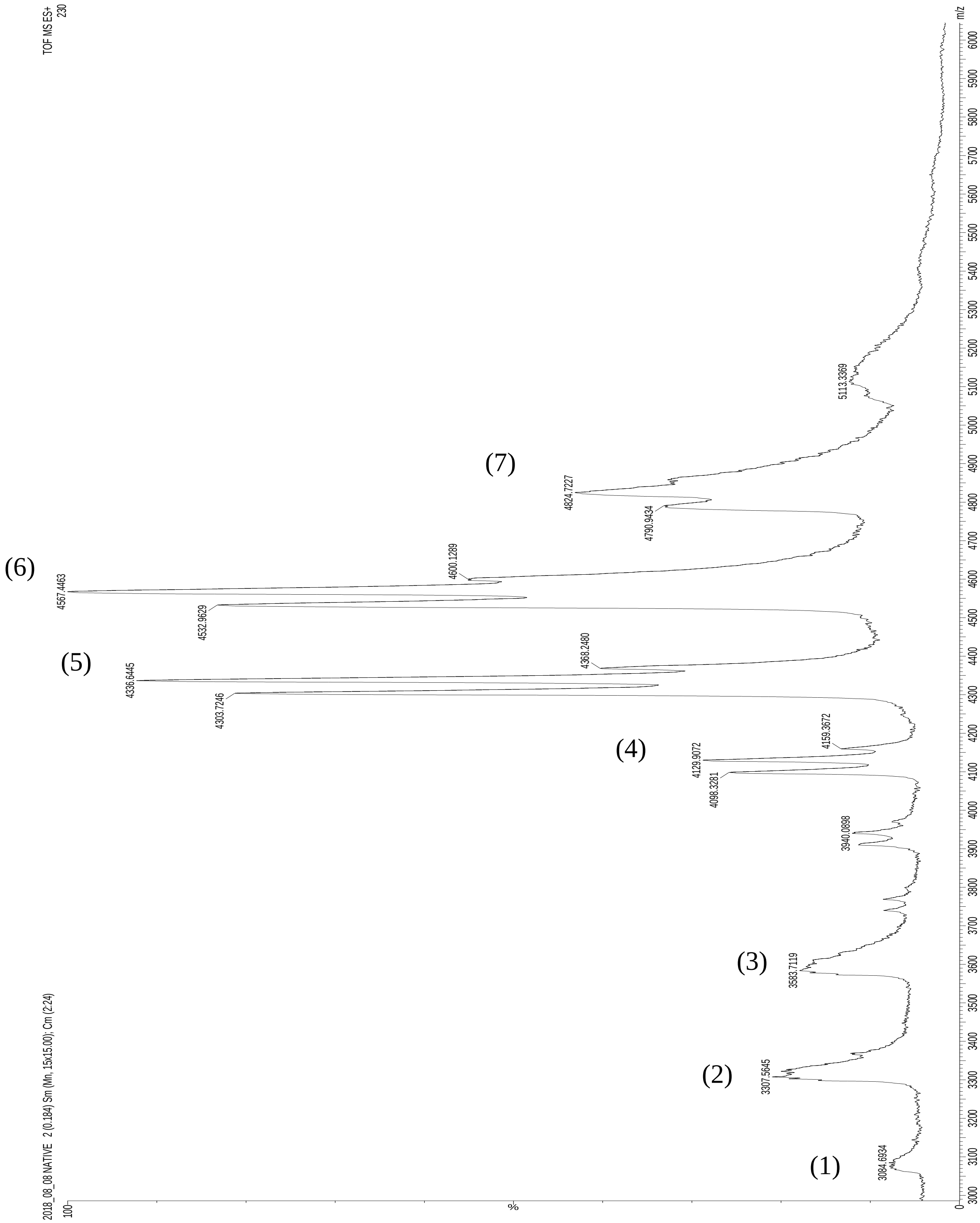

Figure B.1: Native GSNOR MS Spectra. Peaks shown in the 3000-6000 *m/z* window. Three broad monomer peaks followed by dimerized GSNOR.

Figure B.1 continued,

(1) – (3) Tertiary (3º) GSNOR, corresponding to monomer detection.

(4) – (7) Quaternary (4º) GSNOR, corresponding to dimerized GSNOR.

Table B1: Native GSNOR MS spectra peak m/z values and relative intensities. Figure labels as per Figure B.1.

Peak Label	***m/z***	**Relative Intensity**
(1)	3098.6168	3.94
(2)	3337.0012	18.17
(3)	3619.1516	12.55
(4)	4107.7135	8.53
	4139.0778	8.13
	4168.3220	0.81
(5)	4313.2573	53.51
	4346.3899	57.04
	4380.1287	19.53
(6)	4543.0849	81.58
	4579.0460	100.00
	4609.1482	51.71
(7)	4798.6105	45.83
	4833.7635	62.79
	4865.8180	47.55

APPENDIX C – Mass Spectrometry: MS-MS GSNOR

		1 10	20
MGSSHHHHHH	*SSGLVPRGSH*	MANEVIKCKA	AVAWEAGKPL
30	40	50	60
SIEEIEVAPP	KAHEVRIKIIA	TAVCHTDAY	TLSGADPEGC
70	80	90	100
FPVILGHEGA	GIVESVGEGV	TKLKAGDTVI	PLYIPQCGEC
110	120	130	140
KFCLNPKTNL	CQKIRVTQGK	GLMPDGTSRF	TCKGKTILHY
150	160	170	180
MGTSTFSEYT	VVADISVAKI	DPLAPLDKVC	LLGCGISTGY
190	200	210	220
GAAVNTAKLE	PGSVCAVFGL	GGVGLAVIMG	CKVAGASRII
230	240	250	260
GVDINKDKFA	RAKEFGATEC	INPQDFSKPI	QEVLIEMTDG
270	280	290	300
GVDYSFECIG	NVKVMRAALE	ACHKGWGVSV	VVGVAASGEE
310	320	330	340
IATRPFQLVT	GRTWKGTAFG	GWKSVESVPK	LVSEYMSKKI
250	360	370	374
KVDEFVTHNL	SFDEINKAFE	LMHSGKSIRT	VVKI
LEHHHHHH			

Figure C.1: GSNOR MS-MS Peptide Map. Highlighted amino acids are represented by identified peptides.

Table C.1: Full peptide list resulting from MS-MS identification. Theoretical amino acid number corresponds to labels beginning at Met1, whereas experimental amino acid numbers include the His tags of the recombinant protein. 292 total amino acids have been sequenced, however only 188 unique amino acids have coverage, resulting in a 52% sequence coverage of the 374 relevant residues. 48% coverage with His tags included.

m/z	Theoretical Amino Acid Number	Experimental Amino Acid Number	Amino Acid Sequence
813.3543	0-6	20-26	(S)HMANEVI(K)
690.0621	7-11	27-33	(I)KCKAAVA/(W)
621.4647	11-22	31-42	(A)/AVAWEAGKPLSI(E)
545.9043	25-43	45-54	(E)/IEVAPPKAHE/(V)
406.9651	35-41	55-61	(E)/VRIKIIA/(T)
457.5103	35-42	55-62	(E)/VRIKIIAT(A)
508.7969	42-56	62-76	(A)/TAVCHTDAYTLSGAD(P)
462.4796	52-56	72-76	(T)LSGAD(P)
762.2355	64-79	84-99	(V)ILGHEGAGIVESVGEG(V)
749.1952	66-81	86-101	(L)/GHEGAGIVESVGEGVT(K)
1260.826	75-87	95-107	(E)/SVGEGVTKLKAGD(T)
1017.545	78-87	98-107	(G)EGVTKLKAGD(T)
889.3751	91-98	111-118	(I)PLYIPQCG(E)
863.8682	131-138	151-158	(F)/TCKGKTIL/(H)
796.6921	139-145	159-165	(L)/HYMGTST(F)
903.3278	187-195	207-215	(T)AKLEPGSVC(A)
646.5185	190-203	210-223	(L)/EPGSVCAVFGLGGV(G)
1091.721	194-205	214-225	(S)VCAVFGLGGVGL/(A)
1074.582	210-220	230-240	(M)GCKVAGASRII(G)
537.7998	211-221	231-241	(G)CKVAGASRIIG(V)
950.457	223-230	243-250	(V)DINKDKFA/(R)
1053.654	228-236	248-256	(D)KFARAKEFG(A)
669.6493	231-242	251-262	(A)/RAKEFGATECIN(P)
726.2026	233-246	253-265	(A)/KEFGATECINPQD(F)
818.1564	239-245	259-265	(T)ECINPQD(F)
1061.054	246-254	266-274	(D)FSKPIQEVL/(I)
1038.94	315-324	335-344	(W)/KGTAFGGWKS(V)
1173.876	320-330	340-350	(F)/GGWKSVESVPK(L)
587.3912	324-334	344-354	(K)SVESVPKLVSE/(Y)
1241.154	334-343	354-363	(S)EYMSKKIKVD(E)
965.4494	353-360	373-380	(F)/DEINKAFE/(L)
1231.957	354-363	374-383	(D)EINKAFELMH(S)

APPENDIX D – Mass Spectrometry: HDX-MS GSNOR

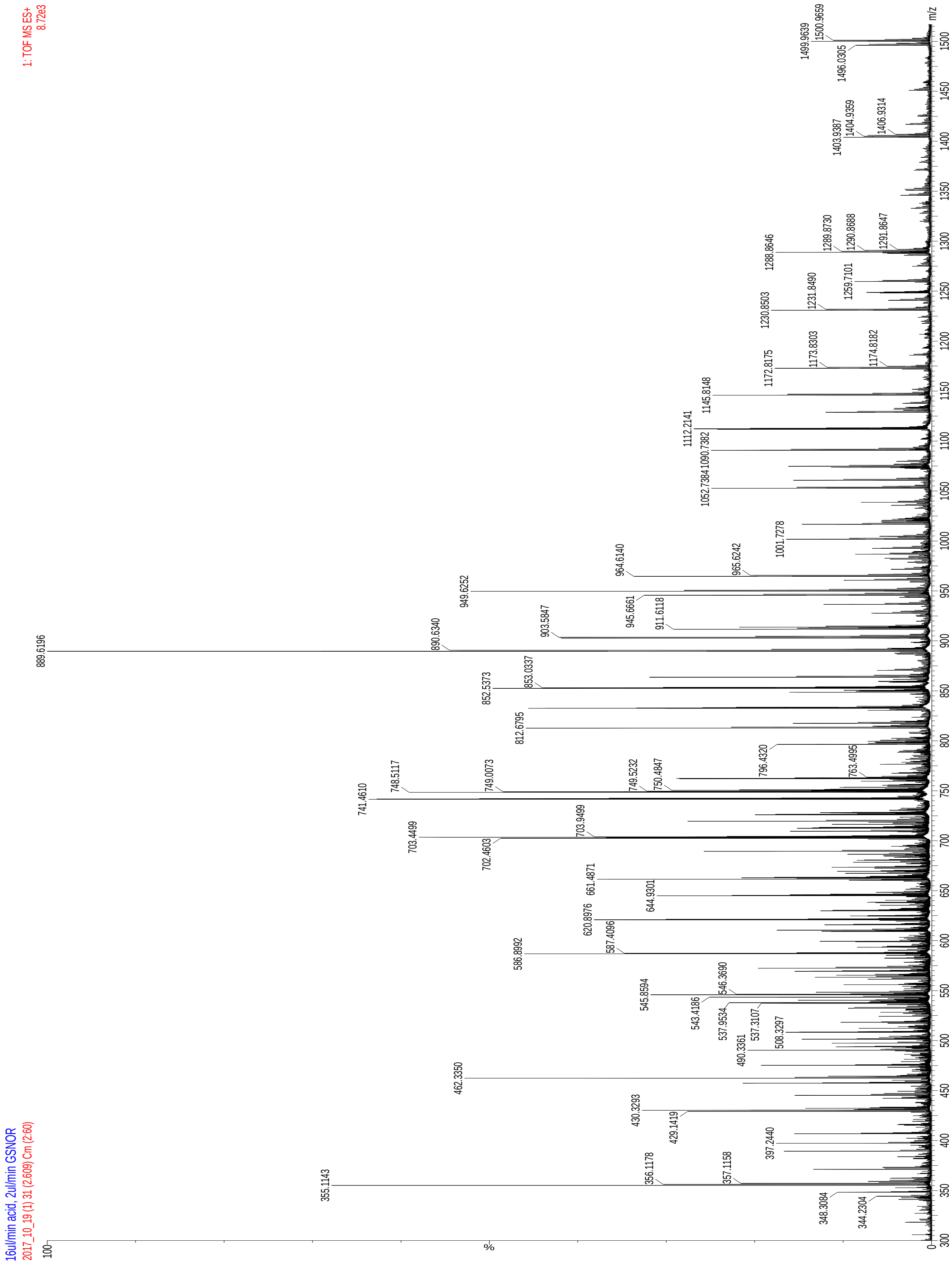

Figure D.1: GSNOR MS fingerprint, with pepsin fragmentation.

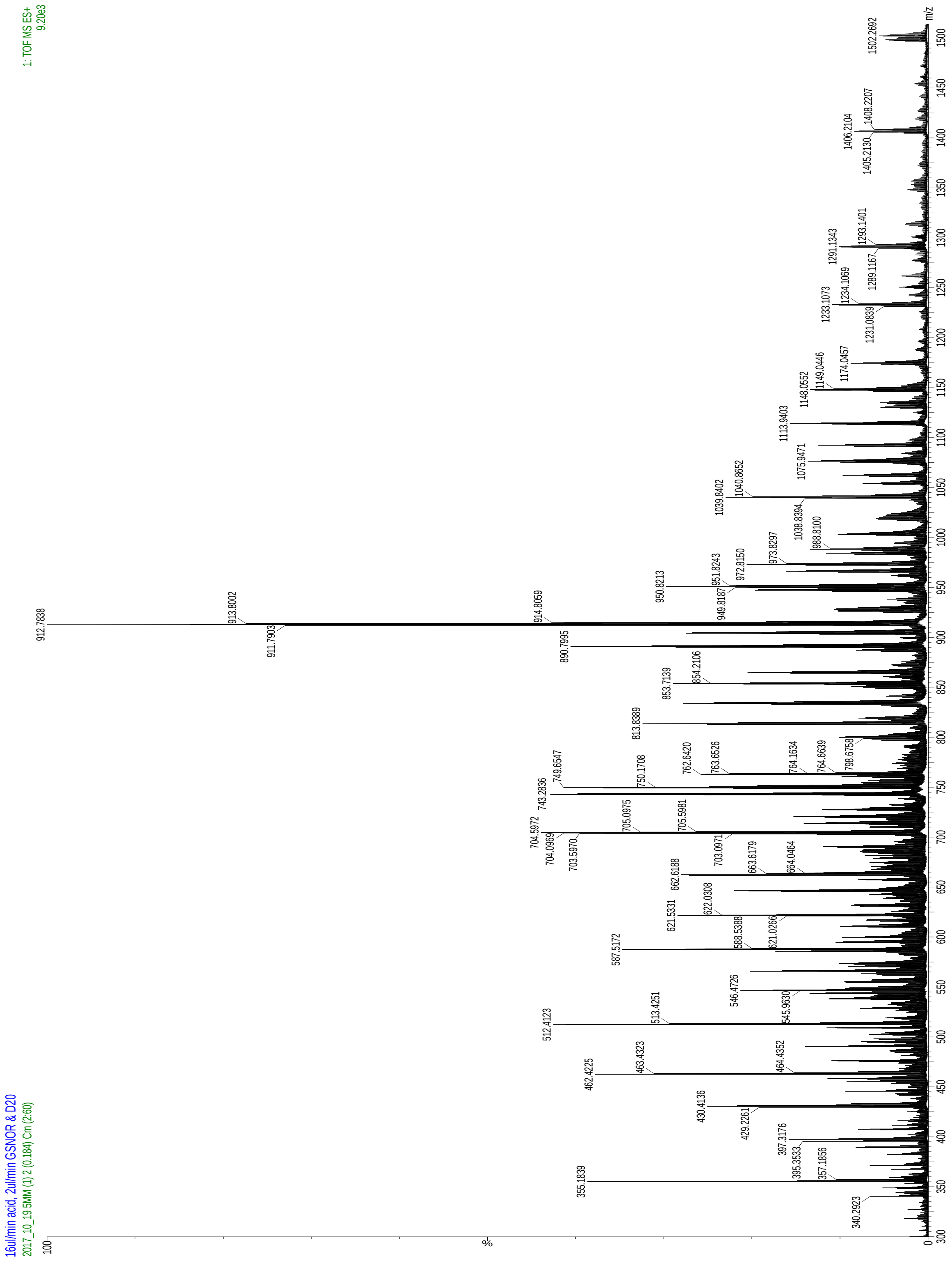

Figure D.2: GSNOR HDX-MS with two seconds reaction time.

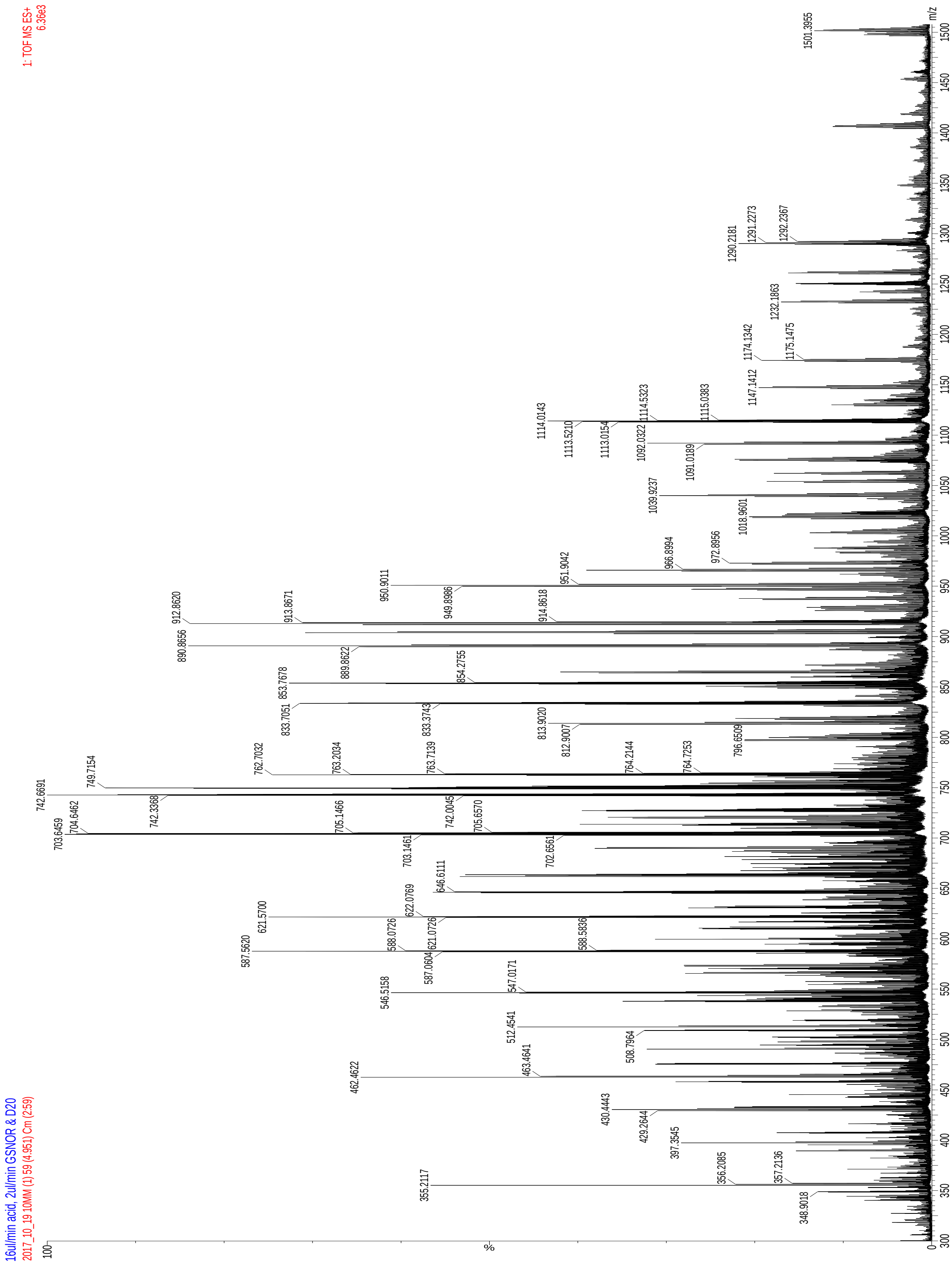

Figure D.3: GSNOR HDX-MS with four seconds reaction time.

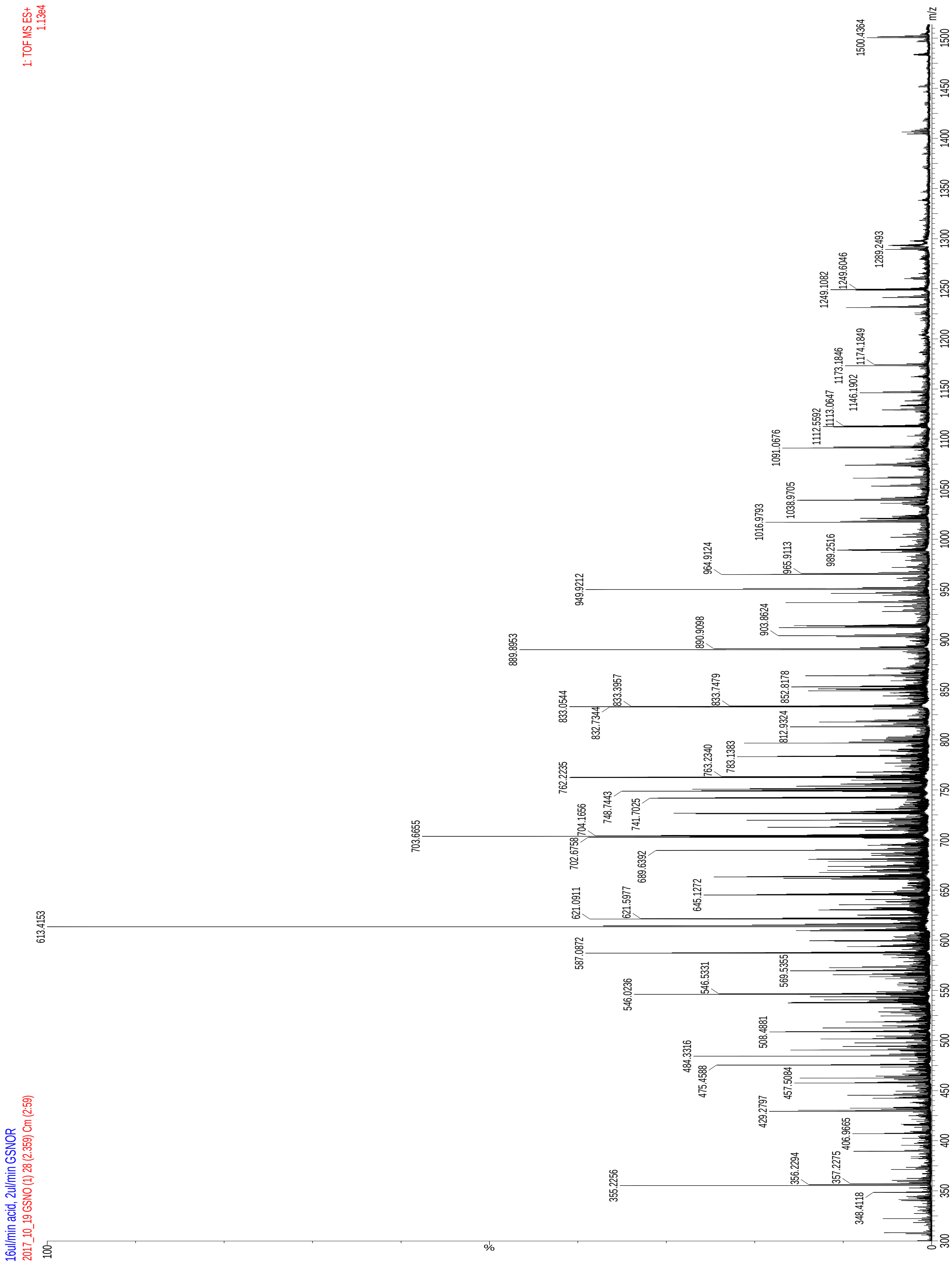

Figure D.4: GSNOR + 20x GSNO MS fingerprint, with pepsin fragmentation.

]

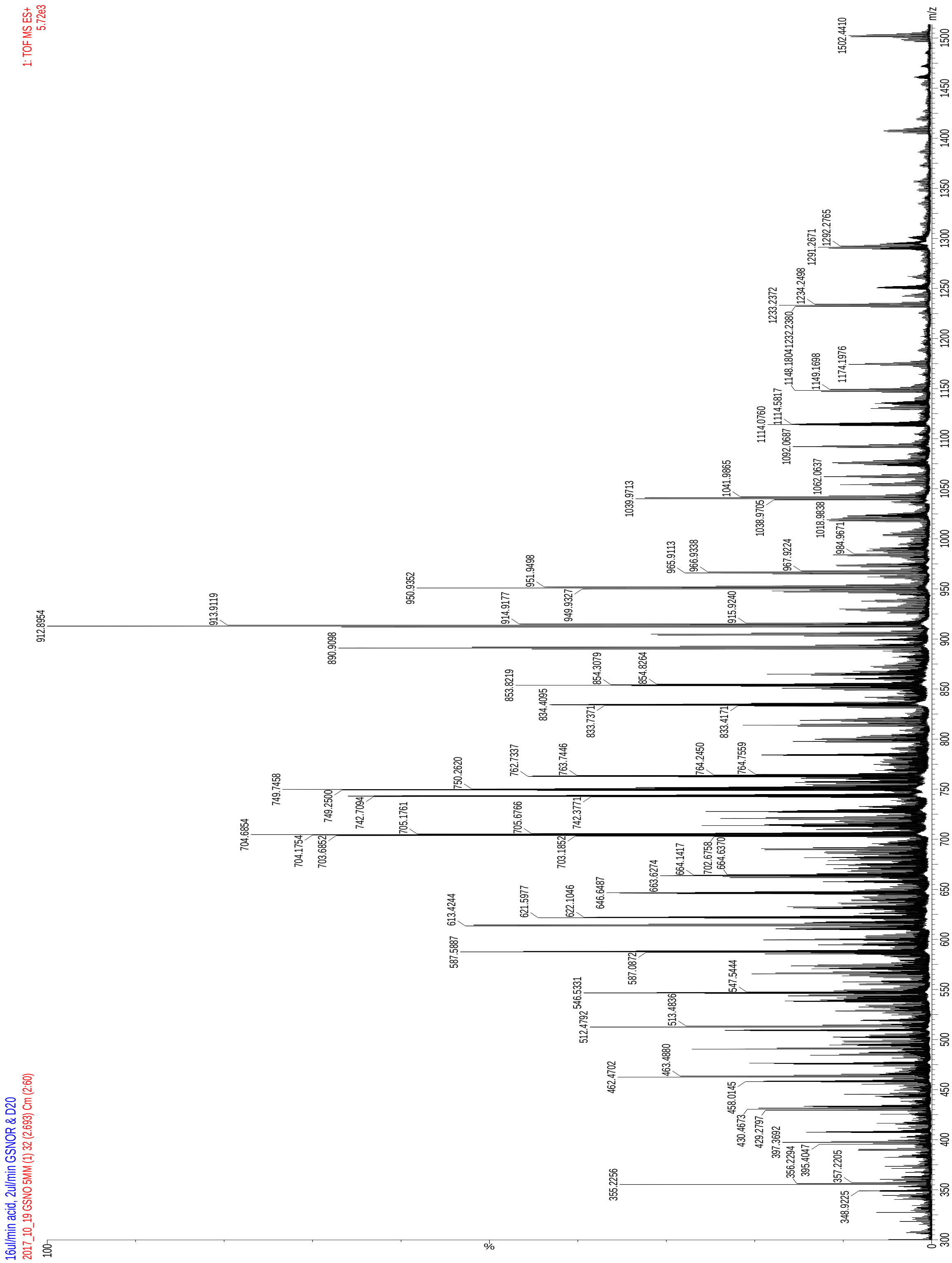

Figure D.5: GSNOR + 20x GSNO HDX-MS with two seconds reaction time.

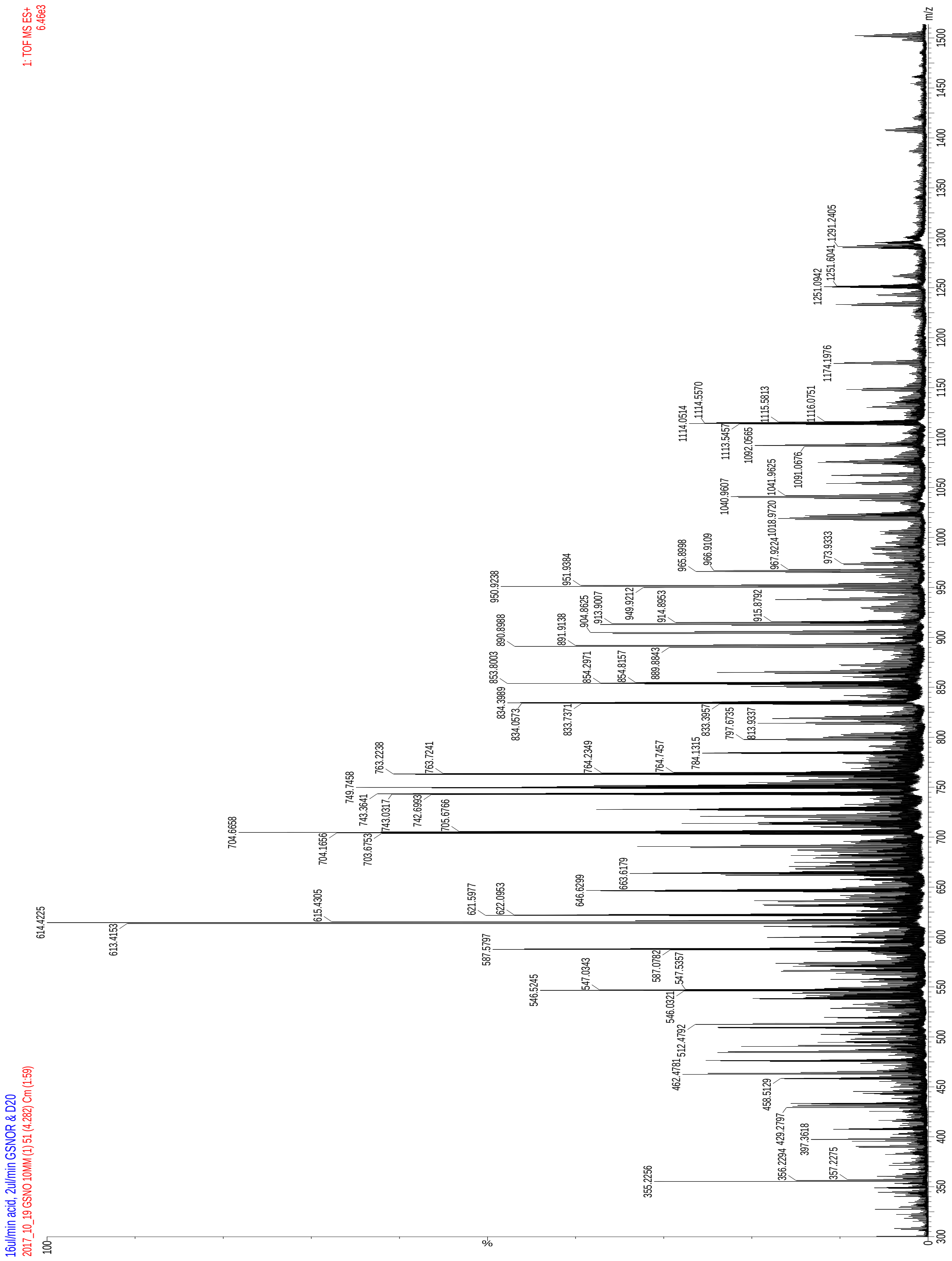

Figure D.6: GSNOR + 20x GSNO HDX-MS with four seconds reaction time.

Table D.1: Representative peptide to visualize deuterium uptake.

Peak information: 889.6 m/z, and the amino acid sequence is (I)PLYIPQCG(E) of residues 91-98. Deuterium uptake (D) and change of deuterium uptake (ΔD) is displayed.

GSNOR HDX-MS:		**GSNOR + GSNO HDX-MS:**	
No Deuterium Exchange	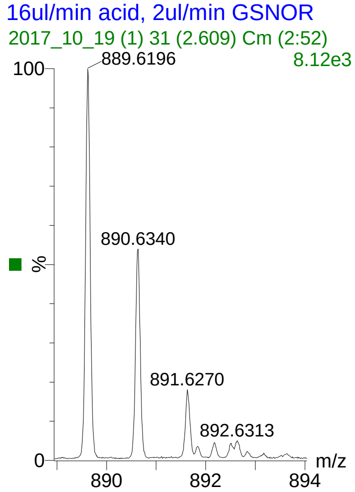	No Deuterium Exchange	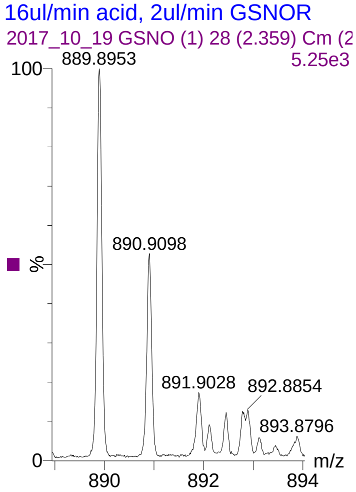
Two sec Exchange D: 24.4% ± 2.1	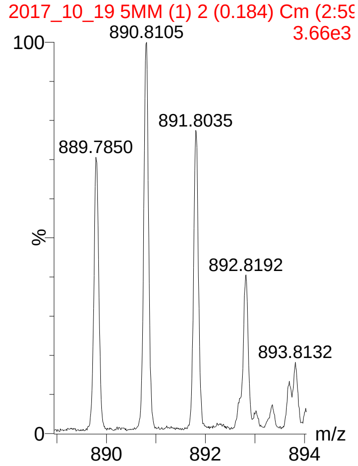	Two sec Exchange D: 24.0% ± 0.3 ΔD: -0.4%	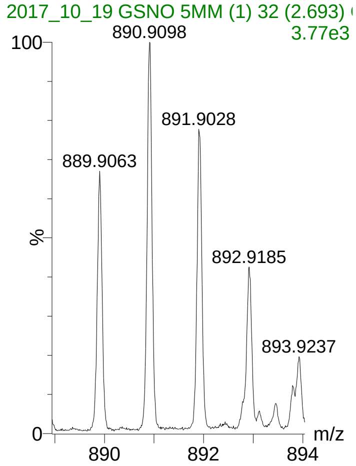
Four sec Exchange D: 27.1% ± 1.6	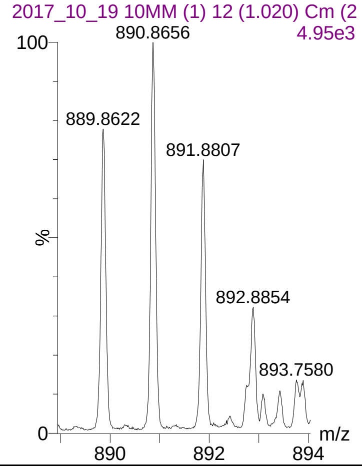	Four sec Exchange D: 27.5% ± 0.5 ΔD: +0.4%	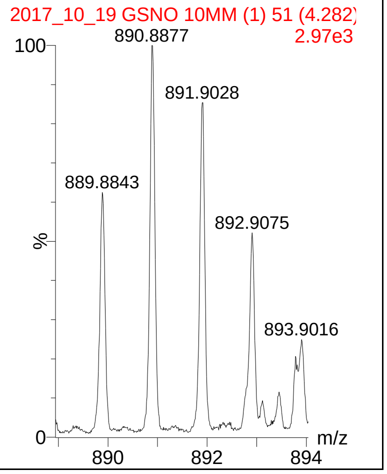

Table D.2: Deuterium uptake results of two second reaction time. With and without the addition of substrate GSNO. The difference in those values is shown as a heat map, Red = decrease in deuterium uptake, Blue = increase in uptake. The colour legend used for crystal structure representation images is shown below.

Red	Salmon	Pink		Sky Blue	Blue
-1.8	-0.7	-0.4	0	0.6	3.4

Baseline Deuterium Uptake (%) (n=6)	GSNO Deuterium Uptake (%) (n=2)	Δ Uptake (%) & Colour		Amino Acid Residue	Amino Acid Sequence
17.2 ± 1.4	17.0 ± 0.0	-0.2	Pink	0-6	(S)HMANEVI(K)
15.9 ± 2.7	15.8 ± 1.2	-0.1	Pink	7-11	(I)KCKAAVA/(W)
12.7 ± 1.1	12.8 ± 1.2	+0.2	Sky	11-22	(A)/AVAWEAGKPLSI(E)
17.0 ± 1.2	16.7 ± 0.7	-0.3	Pink	25-34	(E)/IEVAPPKAHE/(V)
21.3 ± 1.6	20.7 ± 0.0	-0.6	Salmon	35-41	(E)/VRIKIIA/(T)
21.6 ± 1.5	20.2 ± 0.5	-1.4	Red	35-42	(E)/VRIKIIAT(A)
11.9 ± 1.1	11.5 ± 0.5	-0.4	Pink	42-56	(A)/TAVCHTDAYTLSGAD(P)
20.3 ± 2.1	19.2 ± 0.5	-1.2	Red	52-56	(T)LSGAD(P)
9.5 ± 0.9	9.2 ± 0.2	-0.3	Pink	64-79	(V)ILGHEGAGIVESVGEG(V)
9.7 ± 0.7	9.0 ± 1.0	-0.7	Salmon	66-81	(L)/GHEGAGIVESVGEGVT(K)
18.4 ± 2.5	20.8 ± 1.2	+2.4	Blue	78-87	(G)EGVTKLKAGD(T)
24.4 ± 2.1	24.0 ± 0.3	-0.4	Pink	91-98	(I)PLYIPQCG(E)
15.7 ± 1.3	15.3 ± 0.0	-0.3	Pink	131-138	(F)/TCKGKTIL/(H)
16.8 ± 1.7	17.0 ± 0.0	+0.3	Sky	139-145	(L)/HYMGTST(F)
25.7 ± 2.8	25.3 ± 0.0	-0.4	Pink	187-195	(T)AKLEPGSVC(A)
19.3 ± 1.6	18.3 ± 1.0	-0.9	Red	190-203	(L)/EPGSVCAVFGLGGV(G)
9.3 ± 0.7	9.0 ± 1.3	-0.3	Pink	194-205	(S)VCAVFGLGGVGL/(A)
16.8 ± 2.5	15.0 ± 0.0	-1.8	Red	210-220	(M)GCKVAGASRII(G)
15.1 ± 1.2	15.3 ± 0.0	+0.2	Sky	223-230	(V)DINKDKFA/(R)
13.4 ± 1.4	12.7 ± 0.7	-0.7	Salmon	228-236	(D)KFARAKEFG(A)
13.8 ± 0.5	15.7 ± 0.0	+1.8	Blue	231-242	(A)/RAKEFGATECIN(P)
19.9 ± 2.3	23.3 ± 0.0	+3.4	Blue	233-245	(A)/KEFGATECINPQD(F)
29.5 ± 3.5	29.7 ± 0.0	+0.1	Sky	239-245	(T)ECINPQD(F)
17.1 ± 1.8	15.8 ± 1.2	-1.2	Red	246-254	(D)FSKPIQEVL/(I)
15.9 ± 2.5	15.0 ± 1.0	-0.9	Red	315-324	(W)/KGTAFGGWKS(V)
13.7 ± 1.3	12.3 ± 0.3	-1.4	Red	320-330	(F)/GGWKSVESVPK(L)
14.8 ± 1.3	14.3 ± 0.3	-0.4	Pink	324-334	(K)SVESVPKLVSE/(Y)
15.0 ± 1.1	15.3 ± 0.0	+0.3	Sky	334-343	(S)EYMSKKIKVD(E)
19.3 ± 1.3	19.0 ± 0.7	-0.3	Pink	353-360	(F)/DEINKAFE/(L)
17.6 ± 1.4	18.2 ± 0.2	+0.6	Sky	354-363	(D)EINKAFELMH(S)

Table D.3: Deuterium uptake results of four second reaction time. With and without the addition of substrate GSNO. The difference in those values is shown as a heat map, Red = decrease in deuterium uptake, Blue = increase in uptake. The colour legend used for crystal structure representation images is shown below.

Red	Salmon		Sky Blue	Dodger Blue	Blue
-5.2	-0.8	0	0.7	1.4	5.1

Baseline Deuterium Uptake (%) (n=6)	GSNO Deuterium Uptake (%) (n=2)	Δ Uptake (%) & Colour		Amino Acid Residue	Amino Acid Sequence
16.6 ± 1.8	18.7 ± 0.0	+2.1	Blue	0-6	(S)HMANEVI(K)
16.4 ± 3.1	17.7 ± 0.7	+1.3	Dodger	7-11	(I)KCKAAVA/(W)
12.3 ± 1.9	13.2 ± 0.2	+0.8	Dodger	11-22	(A)/AVAWEAGKPLSI(E)
16.5 ± 2.3	17.7 ± 0.0	+1.2	Dodger	25-34	(E)/IEVAPPKAHE/(V)
20.3 ± 3.1	21.7 ± 0.0	+1.4	Dodger	35-41	(E)/VRIKIIA/(T)
20.4 ± 2.4	21.2 ± 0.5	+0.8	Dodger	35-42	(E)/VRIKIIAT(A)
11.7 ± 2.0	12.2 ± 0.2	+0.5	Sky	42-56	(A)/TAVCHTDAYTLSGAD(P)
20.9 ± 2.5	21.5 ± 0.5	+0.6	Sky	52-56	(T)LSGAD(P)
9.3 ± 1.3	10.0 ± 0.0	+0.7	Sky	64-79	(V)ILGHEGAGIVESVGEG(V)
9.2 ± 1.4	9.5 ± 0.5	+0.3	Sky	66-81	(L)/GHEGAGIVESVGEGVT(K)
19.2 ± 3.7	23.5 ± 3.5	+4.3	Blue	78-87	(G)EGVTKLKAGD(T)
27.1 ± 1.6	27.5 ± 0.5	+0.4	Sky	91-98	(I)PLYIPQCG(E)
15.3 ± 2.3	16.0 ± 0.0	+0.7	Sky	131-138	(F)/TCKGKTIL/(H)
17.3 ± 2.7	17.7 ± 0.0	+0.3	Sky	139-145	(L)/HYMGTST(F)
24.9 ± 2.7	24.3 ± 0.0	-0.6	Salmon	187-195	(T)AKLEPGSVC(A)
19.3 ± 2.4	18.5 ± 1.8	-0.8	Salmon	190-203	(L)/EPGSVCAVFGLGGV(G)
8.8 ± 1.2	9.7 ± 0.7	+0.9	Dodger	194-205	(S)VCAVFGLGGVGL/(A)
17.7 ± 2.3	13.7 ± 0.0	-4.0	Red	210-220	(M)GCKVAGASRII(G)
14.3 ± 2.4	16.3 ± 0.3	+2.1	Blue	223-230	(V)DINKDKFA/(R)
13.1 ± 2.4	13.2 ± 0.2	+0.1	Sky	228-236	(D)KFARAKEFG(A)
11.0 ± 0.3	14.7 ± 0.0	+3.7	Blue	231-242	(A)/RAKEFGATECIN(P)
18.6 ± 4.0	23.7 ± 0.0	+5.1	Blue	233-245	(A)/KEFGATECINPQD(F)
30.1 ± 2.9	30.7 ± 0.0	+0.6	Sky	239-245	(T)ECINPQD(F)
17.4 ± 2.3	12.2 ± 3.8	-5.2	Red	246-254	(D)FSKPIQEVL/(I)
15.8 ± 3.6	15.8 ± 0.2	+0.1	Sky	315-324	(W)/KGTAFGGWKS(V)
13.0 ± 2.0	13.5 ± 0.2	+0.5	Sky	320-330	(F)/GGWKSVESVPK(L)
14.5 ± 1.6	15.3 ± 0.3	+0.8	Dodger	324-334	(K)SVESVPKLVSE/(Y)
15.7 ± 2.2	15.3 ± 0.0	-0.3	Salmon	334-343	(S)EYMSKKIKVD(E)
17.5 ± 2.8	19.7 ± 0.3	+2.2	Blue	353-360	(F)/DEINKAFE/(L)
17.2 ± 2.8	18.2 ± 0.5	+1.0	Dodger	354-363	(D)EINKAFELMH(S)

VITA AUCTORIS

NAME: Kathleen Fontana
PLACE OF BIRTH: Cambridge, ON

YEAR OF BIRTH: 1994

EDUCATION: St. Anne High School, Belle River, ON, 2012

University of Windsor, B.Sc., Windsor, ON, 2016

University of Windsor, M.Sc., Windsor, ON, 2018